*Correction*

The value of shear strain for the population of amphibole crystals is $\gamma = 0.75$. It is plotted incorrectly as 1.0 in figures 3.13 and 4.13b. This error is limited to these two figures. The correct value is used in all the calculations, captions and text, and conclusions are not affected. The corrected plots are below.

-Eric Beam 6/26/96

Figure 3.13

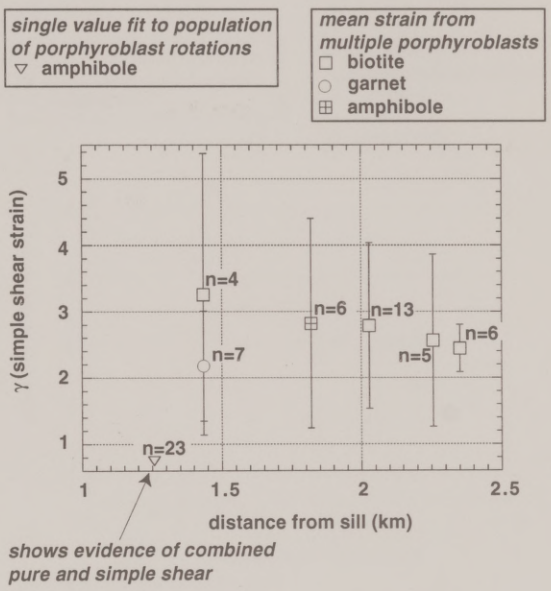


Figure 4.13b

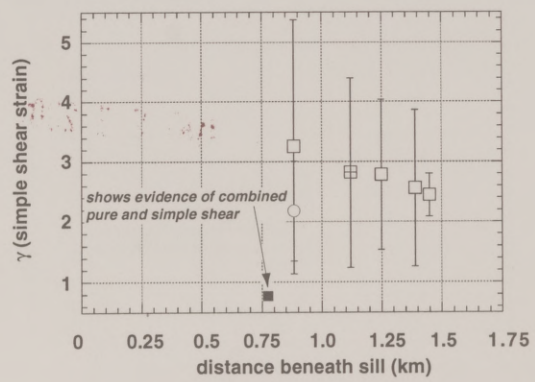

# Tectonothermal effects of mid- and upper-crustal magmatism

by

**Eric Christopher Beam, B.A., M.S.**

**Dissertation**

Presented to the Faculty of the Graduate School of

The University of Texas at Austin

in Partial Fulfillment

of the Requirements

for the Degree of

**Doctor of Philosophy**

**The University of Texas at Austin**

**August, 1996**

# Tectonothermal effects of mid- and upper-crustal magmatism

**Approved by**
**Dissertation Committee:**

[redacted]
Mark Cloos, Supervisor

[redacted]
William D. Carlson

[redacted]
Donald M. Fisher

[redacted]
Mark Helper

[redacted]
Lincoln S. Hollister

[redacted]
Sharon Mosher

## Acknowledgements

Thanks to everyone who helped, so many and in so many ways that it is difficult to list them. First, Mark Cloos made this possible, from start to finish. My other committee members also gave expert advice and encouragement along the way. Fieldwork in Alaska would have been difficult or impossible without the help of Ed and Howard Lightfoot, Dwight and Lauren Bradley, Leo Mark Anthony, Jerry O'Conner and everyone at Valdez Creek Mining Company. I would not have been able to begin the finite element aspect portion of this project without the help of Denise Apperson, Steve Cohen, and Clark Wilson. At Texas, I was lucky to share office space at one time or another with Barb Marin, Katherine Romanak, Becky Smyth, Roberto Gutierrez, Paul Warren, Amy Gray, Widodo Sudomo, and Sarah Penniston-Dorland. Amy and Sarah served as student editors, and were especially good friends during this difficult final year. Tim McMahon was a great help and a good teacher when I tried to understand the mysteries of igneous system evolution. John Kuehne provided constant technical advice and encouragement. And, of course, I owe the most to my family, especially my wife Mary. Financial support was provided by the University of Texas, the Geology Foundation, the Geological Society of America, Sigma Xi, and Freeport-McMoRan.

# Tectonothermal effects of mid- and upper-crustal magmatism

Publication No._____

Eric Christopher Beam, Ph.D.

The University of Texas at Austin, 1996

Supervisor: Mark Cloos

This study considers the effects of the addition of heat and fluids to the earth's middle and upper crust by magmatism, as well as methods by which these effects may be distinguished in rock fabrics.

A series of axisymmetric finite element transient heat conduction models were constructed to estimate crystallization rates, a proxy for fluid production. Crystallization rate varies from a high of ~80 $km^3$/ky to a low of ~10 $km^3$/ky. The shape of the crystallization rate histories is also highly variable, with thinner batholiths having high, sharp, early peaks. High fluid production rates will favor pooling of magmatic fluids in cupolas at the tops of stocks. In some cases this may trigger explosive eruptions, but in others could lead to economic mineralization.

A computer program was written to simulate the formation of inclusion trails in porphyroblasts growing in deforming rocks. This program models synkinematic porphyroblast growth as a series of steps of growth and rotation. Resultant inclusion trails are complex. This complexity is a result of the variable relative rates of rotation of the inclusion and the cleavage. In some cases foliations

are generated which could easily be interpreted as an included crenulation cleavage, other cases give an apparent sense of rotation opposite to the actual rotation.

Theory describing the rotation of rigid inclusions is applied to biotite, garnet, and amphibole porphyroblasts in order to evaluate the sense of shear, magnitude of strain, and strain path (pure vs. simple shear) in deformed metamorphosed rocks adjacent to a tonalite sill in the Maclaren Glacier Metamorphic Belt (MGMB), south-central Alaska. Mean shear strains determined from biotite populations in thin sections range from $\gamma = 2.4$ to 3.3.

Coupled temperature-displacement finite element models were constructed to simulate a cooling pluton in a zone of simple shear, using a realistic power law rheology. From these models it is clear that the thermal anomaly associated with a cooling pluton can concentrate deformation not just in the pluton, but into a laterally extensive zone running through the pluton. This may explain the deformation observed in the MGMB.

# Table of Contents

# List of Figures

# List of Tables

# Chapter 1: Crystallization and fluid production rates from conductive thermal modeling of granitic stock-batholith systems


## ABSTRACT

Quantitative understanding of the rates at which volatiles are released from magma in large chambers is needed to constrain models of the processes of explosive volcanism and the generation of orthomagmatic ore deposits. This study models the crystallization of magma in stock-batholith systems by performing axisymmetric finite element transient heat conduction analyses. Twenty geometries are considered, with batholith volumes from 500 to 2000 $km^3$, and stock volumes from 60 to 235 $km^3$. Thickness of the batholith is also varied from 1 to 4 km. All are intruded at an initial temperature of 1000°C into country rock with a 30°C/km geothermal gradient. The top of the batholith is at 10 km depth. The magma has a latent heat of 334 kJ/kg, released between 1000°C and 800°C. Material below the solidus (800°C) is considered to be 'solid', that above is 'liquid'. The changing volume of liquids and solids in the system is calculated, and the crystallization rate (dV/dt) and fluid production rate are derived.

Crystallization rate varies from a high of ~80 $km^3$/ky (1000 $km^3$, 1 km thick batholith) to a low of ~10 $km^3$/ky (2000 $km^3$, 4 km thick batholith). The variation in crystallization rate with time is also highly variable, with thinner batholiths having high, sharp, early peaks.

Assuming fluid production is dominated by crystallization, rather than depressurization during convective turnover, the fluid production history is

estimated. A pre-crystallization water content of 2 wt. % causes a range of fluid fluxes from a high of ~11 million kg/day to a low of ~140,000 kg/day. High fluid production rates will favor pooling of magmatic fluids in cupolas at the tops of stocks. In some cases this may trigger explosive eruptions, but if released in a controlled manner could lead to economic mineralization.

## INTRODUCTION

Fluid exsolution is an integral part of magmatism. By the time a silicic magma has completely crystallized, more than 5 wt. % fluids may be released, even after accounting for formation of hydrous minerals (Cline and Bodnar, 1991). Such magmatic fluids are rich in $H_2O$, but also contain $CO_2$ and minor $SO_2$ and HCl (Rubey, 1951, p. 1136; Le Cloarec et al., 1992, p. 21). This magmatic degassing has a profound influence on geologic processes, including, but not limited to explosive volcanism, fracturing, mineralization, contact metamorphism, and ductile deformation. Indeed, magmatic degassing may be responsible for the existence and current composition of the earth's atmosphere and hydrosphere (Rubey, 1951; Best, 1982, p. 588). It seems very likely that magmatic fluids are responsible for a variety of ore deposits (Hedenquist and Lowenstern, 1994). The relative rarity of mineralized intrusions, even in districts of overall similar geochemistry, indicates that some factor other than the amount of fluids released bears on the formation of ore deposits. Thus, the rate, timing, and spatial pattern of magmatic fluid release is of interest to geologists in a variety of fields. These variables are investigated in this paper through a series of forward models of conductive cooling.

A magma releases its volatiles when the saturation limit of the volatile species is reached. There are two end member paths along which a magma may evolve to reach the saturation limit: decompression without crystallization, and isobaric crystallization. These are sometimes called first and second boiling, but as

Shinohara and Kazahaya (1995) point out, the temporal relation between the two processes is not always clear, and the term boiling often refers to the behavior of the fluids after exsolution from the magma.

An example for water is illustrative. A silicic melt has a saturation limit for water which varies with pressure (Cline and Bodnar, 1991) as shown in Figure 1.1. If a melt starts at 1 kbar with 2 wt. % $H_2O$, it can reach saturation by a decompression, of about 700 bars. Although crystallization at constant pressure can concentrate water in the melt as anhydrous minerals form. The same starting melt could reach water saturation through crystallization of 51 % of its mass (Figure 1.1). While most magmas will undergo a history that is a complex combination of these two end members, only the crystallization path is considered here.

## TECHNIQUES

The exsolution considered here is driven by crystallization, which in turn is driven by cooling. Cooling of the magma is modeled to understand the consequent pattern of crystallization and the general temporal and spatial patterns of fluid release. The cooling of a pluton is a complex process that may involve conduction, convection of magma and/or of water in the country rock (Furlong et al., 1991). However, it is possible to justify some simplifying assumptions to understand the basic behavior of the system.

In the magmatic systems modeled in this study, heat transport can be considered to be predominantly by conduction. The bulk of the cooling takes place at depth >10 km, where confining pressure should generally reduce permeability

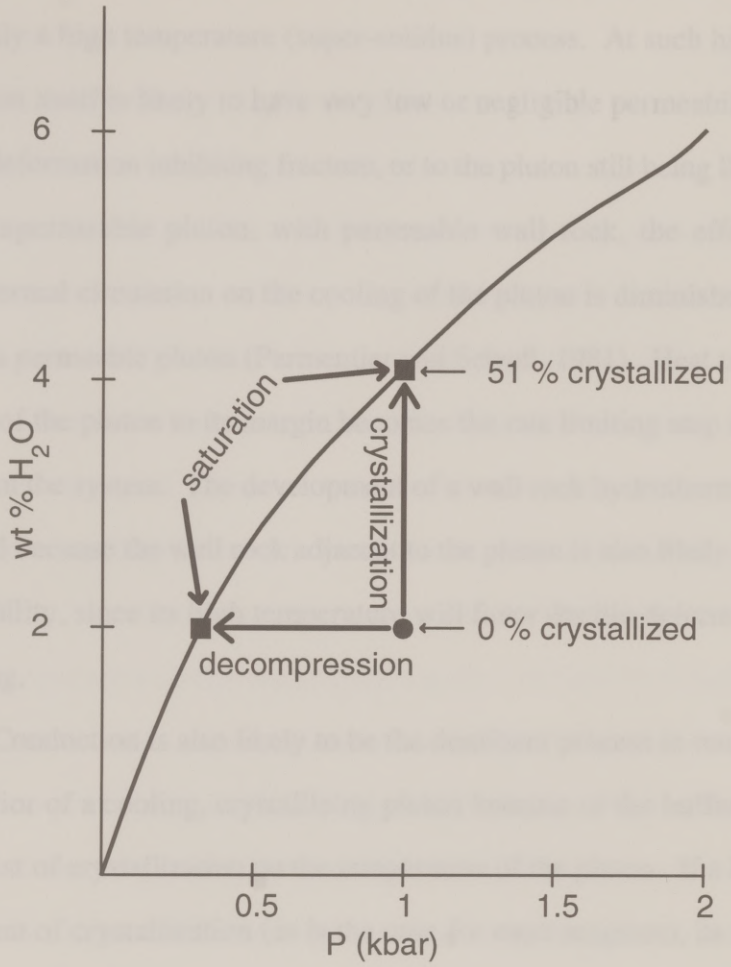


Figure 1.1: An example of two paths by which a magma may reach saturation for water. This study considers the crystallization path. Data from Cline and Bodnar (1991).

and inhibit hydrothermal circulation in the country rock. Thus, conduction will account for most of the heat transport in the wall rock. In addition, degassing is inherently a high temperature (super-solidus) process. At such high temperatures, the pluton itself is likely to have very low or negligible permeability, due either to plastic deformation inhibiting fracture, or to the pluton still being liquid. In the case of an impermeable pluton, with permeable wall rock, the effect of wall rock hydrothermal circulation on the cooling of the pluton is diminished, relative to the case of a permeable pluton (Parmentier and Schedl, 1981). Heat transport from the interior of the pluton to its margin becomes the rate limiting step in the removal of heat from the system. The development of a wall rock hydrothermal system is also inhibited because the wall rock adjacent to the pluton is also likely to have very low permeability, since its high temperature will favor ductile deformation rather than fracturing.

Conduction is also likely to be the dominant process in removing heat from the interior of a cooling, crystallizing pluton because of the buffering effect of the latent heat of crystallization on the temperature of the pluton. If a liquid has a large latent heat of crystallization (as is the case for most magmas), its temperature will be maintained at or near the solidus until the latent heat is released (Marsh, 1988; Stüwe, 1995), and there will be limited variation in the internal temperature. In the absence of large temperature gradients in the liquid, convective heat transfer will be minor or absent (Marsh, 1988; Brandeis and Marsh, 1989). If the temperature of the magma is higher than the liquidus, then vigorous convection of the magma is likely to occur. This convection will rapidly remove superheat (the excess temperature above the liquidus) from the magma chamber, and it is unlikely that an

ascending magma body would reach mid- to upper crustal depths with superheat. In any case, superheat-driven convection operates above the temperature interval in which degassing takes place.

In performing conductive thermal modeling, the dimensionality of the analysis is critical if quantitative timing and rates are of interest. One-dimensional models assume that heat flow is unidirectional (usually vertical within the earth) and that an intrusion is a half space or slab of infinite lateral extent. A one-dimensional model is often sufficient for determining temperature reached in country rock close to a laterally extensive intrusion (Furlong et al., 1991), but is not adequate for the goals of this study. Two-dimensional models are often sufficient for determining the pattern of metamorphic isograds (Bowers et al., 1990; Furlong et al., 1991), but still assume infinite extent of the intrusion in the third dimension. Thus, they are not suited to studies (such as this one) in which time and volumetric rate of crystallization are of critical interest. Three-dimensional studies have the potential to produce results that most closely approximate reality (Bowers et al., 1990). They have the drawback of being computationally intensive, and information about the three-dimensional shape of intrusions is often difficult to obtain.

The results presented here are from two-dimensional axisymmetric finite element heat conduction models. Axisymmetric models combine the realistic time scale of three-dimensional models with the computational efficiency of two-dimensional models. In this study they allow the determination of the changing volume of the magma chamber with time.

The equation describing two-dimensional transient heat conduction in Cartesian (x, y) coordinates, with constant thermal properties and no heat production is:

$$\frac{\partial T}{\partial t} = \left( \kappa \frac{\partial^2 T}{\partial x^2} + \kappa \frac{\partial^2 T}{\partial y^2} \right) \qquad (1.1)$$

(Carslaw and Jaeger, 1959, p. 9; Furlong et al., 1991, p. 439), where T is temperature, t is time, and $\kappa$ is thermal diffusivity. This can be transformed into cylindrical coordinates (r, $\theta$, z, where r is the radial distance from the cylinder axis, $\theta$ is the angle from a reference line, and z is height on the cylinder) using the relationships:

$$x = r \cos \theta$$

$$y = r \sin \theta$$

Substitution of these in (1) gives the equation for heat conduction in cylindrical coordinates:

$$\frac{\partial T}{\partial t} = \kappa \left( \frac{\partial^2 T}{\partial r^2} + \frac{1}{r} \frac{\partial T}{\partial r} + \frac{1}{r^2} \frac{\partial^2 T}{\partial \theta^2} + \frac{\partial^2 T}{\partial z^2} \right) \qquad (1.2)$$

(Carslaw and Jaeger, 1959, p. 17). If there is symmetry about the cylindrical axis (z), then there is no temperature variation along the $\theta$ coordinate, that is:

$$\frac{\partial T}{\partial \theta} = 0$$

and

$$\frac{\partial^2 T}{\partial \theta^2} = 0$$

This transforms (2) into the axisymmetric heat conduction equation:

$$\frac{\partial T}{\partial t} = \kappa\left(\frac{\partial^2 T}{\partial r^2} + \frac{1}{r}\frac{\partial T}{\partial r} + \frac{\partial^2 T}{\partial z^2}\right) \qquad (1.3)$$

This study uses the commercial finite element program ABAQUS to solve the axisymmetric heat conduction equation.

A latent heat of crystallization is approximated by modifying the heat capacity in the range of crystallization, as described by Furlong (1991, p. 462). The heat capacity is the rate of change of the internal energy of the system with change in temperature, that is:

$$C = \frac{\partial U}{\partial T}$$

The release of latent heat is considered to be an increase in the rate of energy release, that is an increase in dU/dT, or C (Figure 1.2). To include this effect in these models, the heat capacity in the range between the liquidus and solidus is increased by the amount of latent heat divided by the crystallization interval, that is:

$$C^* = C + \frac{L}{\left(T_l - T_s\right)} \qquad (1.4)$$

where C is the heat capacity of the rock outside of the crystallization interval, L is the amount of latent heat, $T_l$ is the liquidus temperature, $T_s$ the solidus temperature, and $C^*$ is modified heat capacity used in the solidification interval (see Figure 1.3a). This formula represents a linear release of latent heat between the liquidus and solidus temperatures. In practice it is necessary to apply a correction to smooth out the strong nonlinearities that the abrupt change in heat capacity introduces (Figure 1.3b). Thus, the release of latent heat in these models is 'almost' linear, being slightly less rapid near the liquidus and solidus.

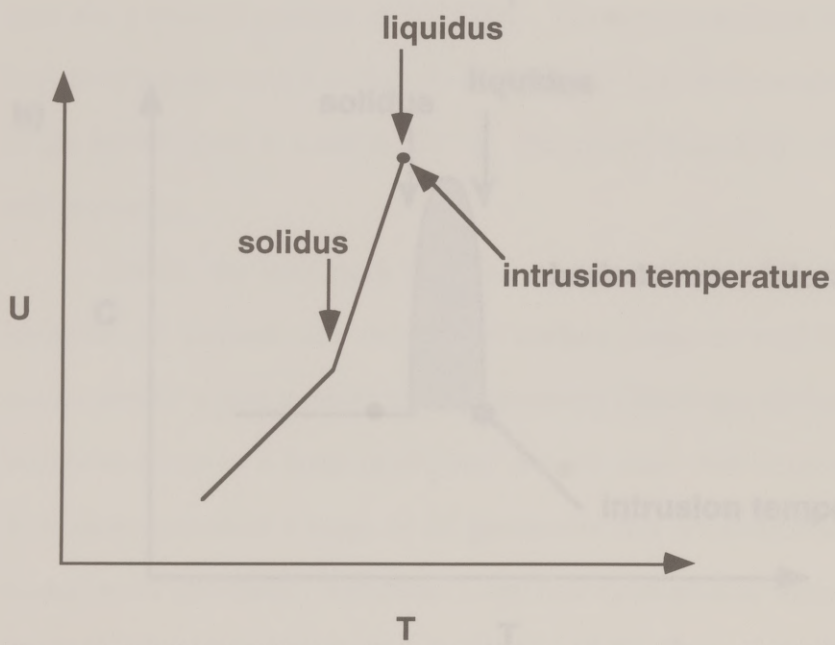


Figure 1.2: Graph of internal energy (U) vs. temperature (T). The release of latent heat is considered to be an increase in the rate of energy released with change in temperature, that is an increase in dU/dT, or C (heat capacity). This is reflected on this plot as a steeper slope during the crystallization interval.

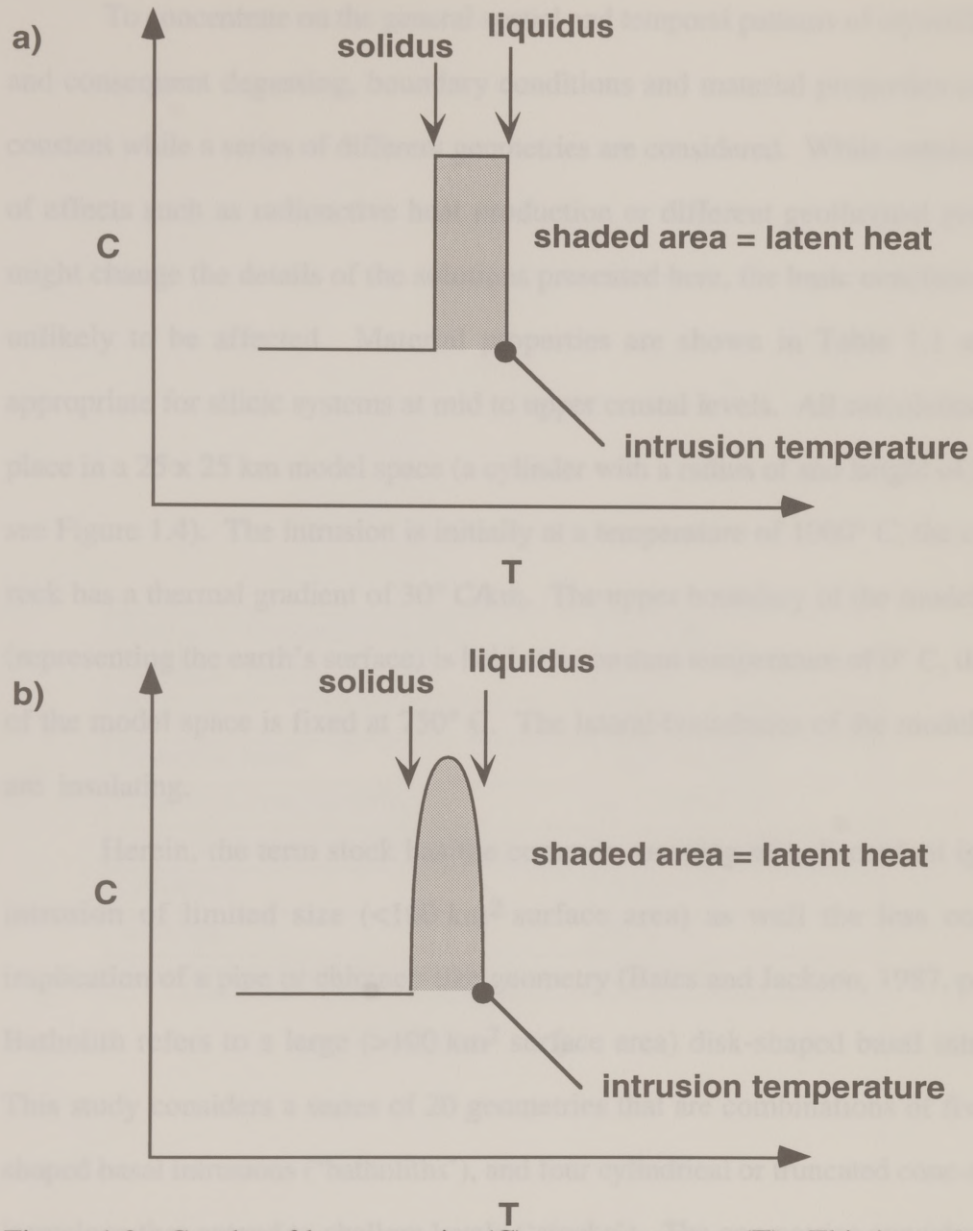


Figure 1.3: Graphs of heat capacity (C) vs. temperature (T). This is a schematic representation of the method used to account for latent heat in these models. (a) The heat capacity in the range between the liquidus and solidus is increased by the amount of latent heat divided by the crystallization interval. The shaded area represents the amount of heat released by crystallization. (b) In practice it is necessary to apply a correction to smooth out the strong nonlinearities which the abrupt change in heat capacity introduces.

To concentrate on the general spatial and temporal patterns of crystallization, and consequent degassing, boundary conditions and material properties are held constant while a series of different geometries are considered. While consideration of effects such as radioactive heat production or different geothermal gradients might change the details of the solutions presented here, the basic conclusions are unlikely to be affected. Material properties are shown in Table 1.1 and are appropriate for silicic systems at mid to upper crustal levels. All calculations take place in a 25 x 25 km model space (a cylinder with a radius of and height of 25 km, see Figure 1.4). The intrusion is initially at a temperature of 1000° C, the country rock has a thermal gradient of 30° C/km. The upper boundary of the model space (representing the earth's surface) is held at a constant temperature of 0° C, the base of the model space is fixed at 750° C. The lateral boundaries of the model space are insulating.

Herein, the term stock has the common meaning of a discordant igneous intrusion of limited size (<100 $km^2$ surface area) as well the less common implication of a pipe or chimney-like geometry (Bates and Jackson, 1987, p. 645). Batholith refers to a large (>100 $km^2$ surface area) disk-shaped basal intrusion. This study considers a series of 20 geometries that are combinations of five disk shaped basal intrusions ('batholiths'), and four cylindrical or truncated cone-shaped intrusions that extend to shallow levels ('stocks'). The geometries considered are illustrated in Figure 1.5.

The reason for inclusion of a stock in these models is that shallow processes involving magmatic fluids, such as mineralization and volcanism, are to a large degree controlled by crystallization processes in a parent batholith. There

| | |
|---|---|
| Ambient thermal gradient | 30 °C/km |
| Surface Temperature | 0 °C |
| Density | 2500 kg/m$^3$ |
| Specific heat | 920 J/kg/°C |
| Thermal conductivity | 2.5 W/m/°C |
| Latent heat of crystallization | 334,000 J/kg |
| Liquidus | 1000° C |
| Solidus | 800 °C |
| Temperature of intrusion | 1000 °C |

Table 1.1: Material properties used in this study, and appropriate for a range of magmatic systems at mid- to upper-crustal levels. Density and thermal conductivity are from Turcotte and Schubert (1982). Latent heat is from Pedersen and Ro (1992) for a melt generated by decompression of the mantle. Heat capacity is chosen to give a heat capacity per unit volume between 2-3 MJ/m$^3$°C, typical of mid- to upper-crustal rocks (Delaney, 1988). Resultant thermal diffusivity is 0.01 cm$^2$/s.

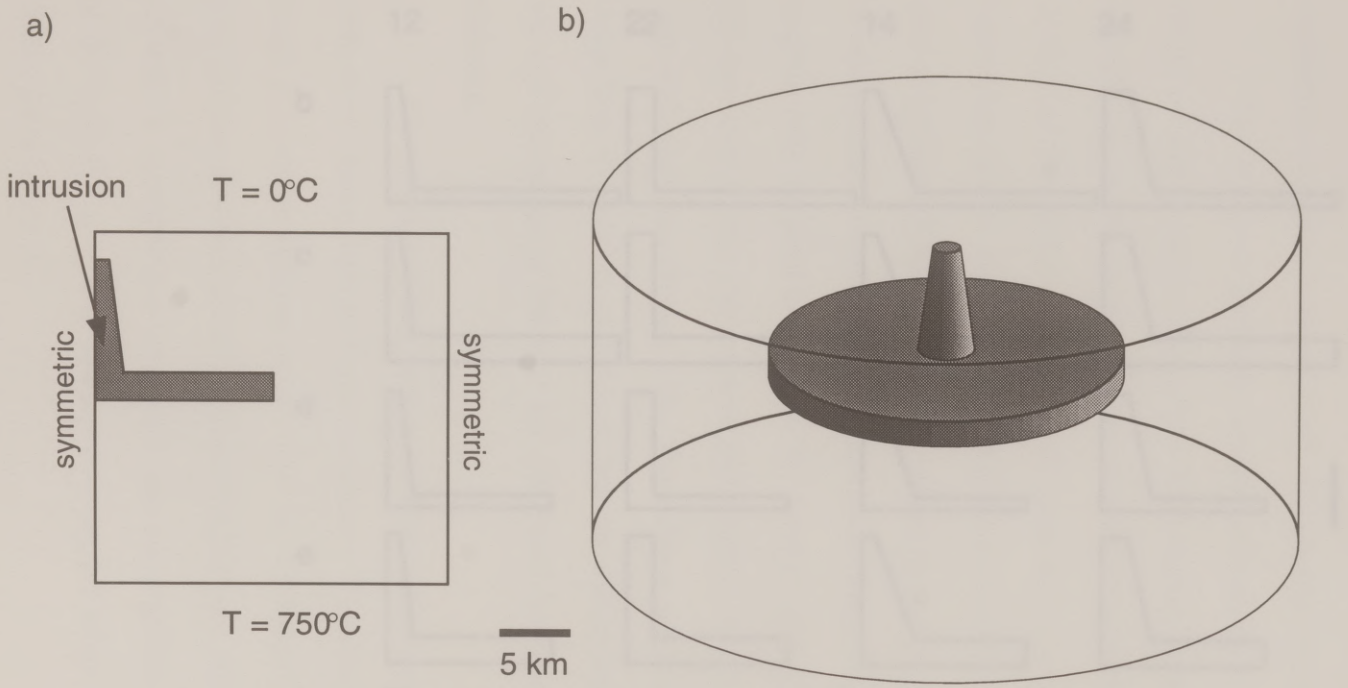


Figure 1.4: (a) Boundary conditions for model. The lateral boundaries are symmetric (insulating). The upper boundary is held at a constant temperature of 0° C, the base is fixed at 750° C. (b) Physical situation being modeled (model domain is a cylinder with a radius of and height of 25 km). The intrusion is shown in gray.

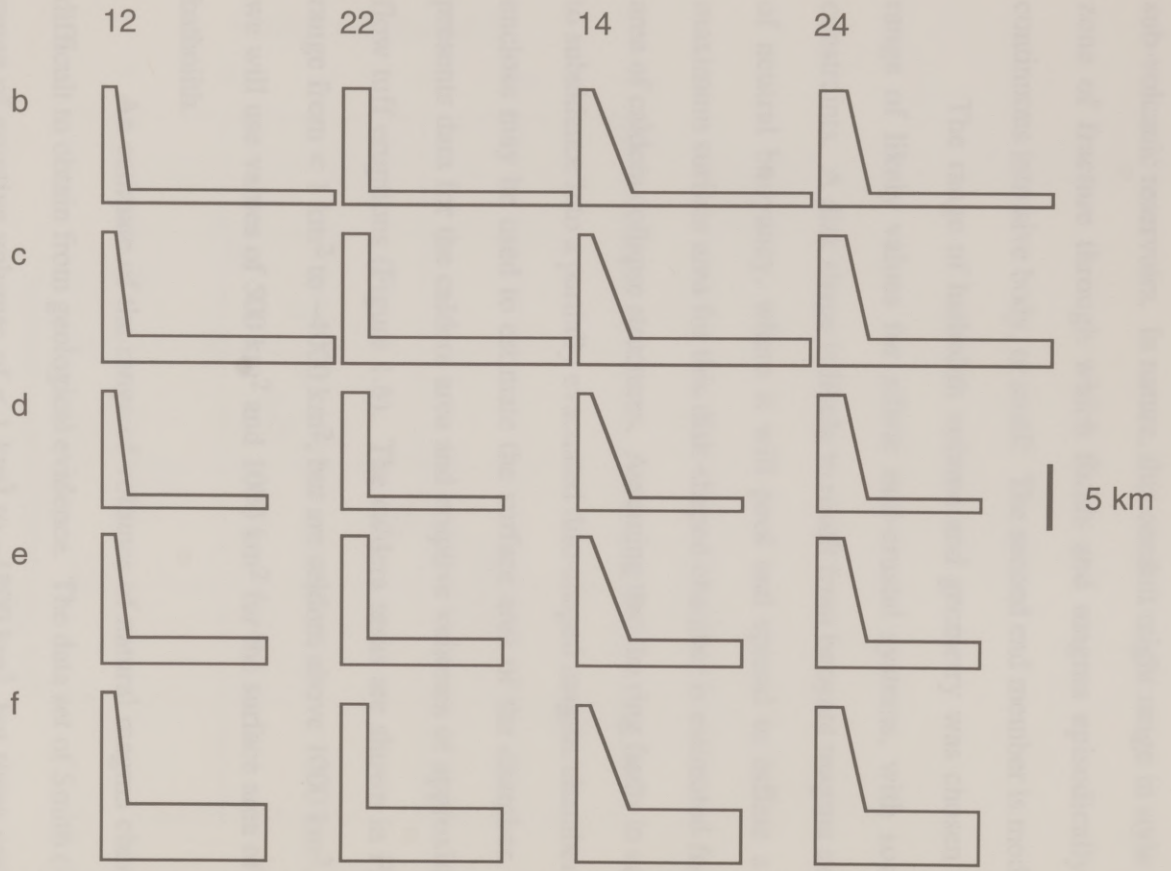


Figure 1.5: Batholith and stock geometries considered. This study considers a series of 20 geometries which are combinations of four stock and five batholith geometries.

must be some form of communication between a deep basal batholith and shallow sub-volcanic reservoirs. In nature, this conduit might range in style from a narrow zone of fracture through which fluids and magma episodically ascend, to a continuous intrusive body, or stock. The second end member is modeled here.

The range of batholith volume and geometry was chosen to represent a range of likely values for silicic mid-crustal systems, with some geological constraints. A disk shape is likely to result from buoyant magma ascent to a level of neutral buoyancy, where it will pool and spread to inflate a chamber. A maximum surface area for this disk-shaped chamber is estimated from the surface area of caldera collapse structures. Assuming that the ring faults in calderas are due to subsidence into a partially evacuated disc-shaped magma chamber, the area they enclose may be used to estimate the surface area of the chamber. Smith (1979) presents data for the caldera area and eruptive volumes of approximately 50 ash-flow tuff eruptions (Figure 1.6). The caldera areas are shown in Figure 1.7, and range from < 1 $km^2$ to ~4000 $km^2$, but are seldom above 1000 $km^2$. In this study we will use values of 500 $km^2$ and 1000 $km^2$ for the surface area of the top of the batholith.

An estimate of the range of volumes of natural magma chambers is more difficult to obtain from geological evidence. The data set of Smith (1979) shows a range of eruptive volumes of < 1 $km^3$ to ~1800 $km^3$, but these numbers provide only minimum estimates of magma chamber size, for it is unlikely that a magma chamber is completely evacuated in any one eruption. In this study, the thickness of the batholith is 1, 2 or 4 km, resulting in a range of volumes of 500, 1000 or 2000 $km^3$ (Table 1.2).

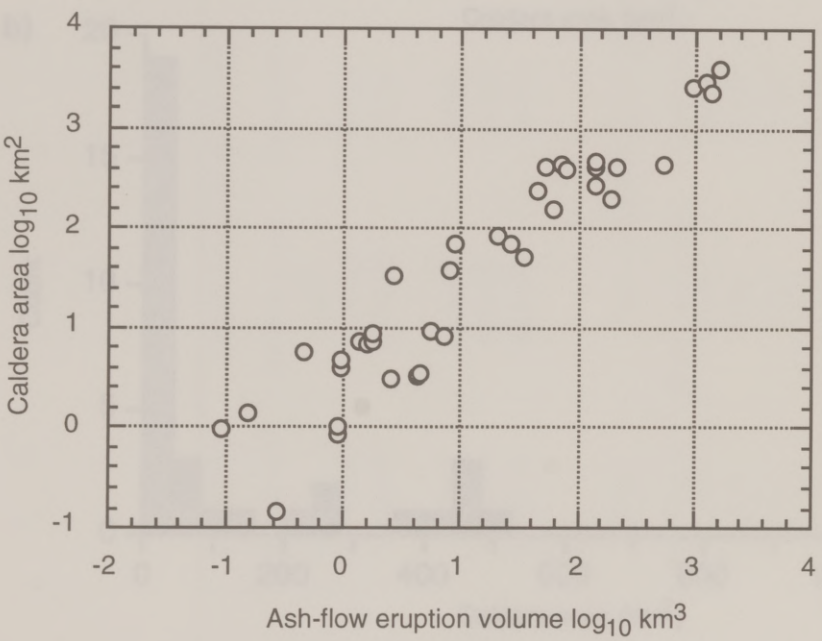


Figure 1.6: Relation between ash-flow eruption volume and associated caldera area. Data from Smith, (1979), San Juan Mountains data omitted.

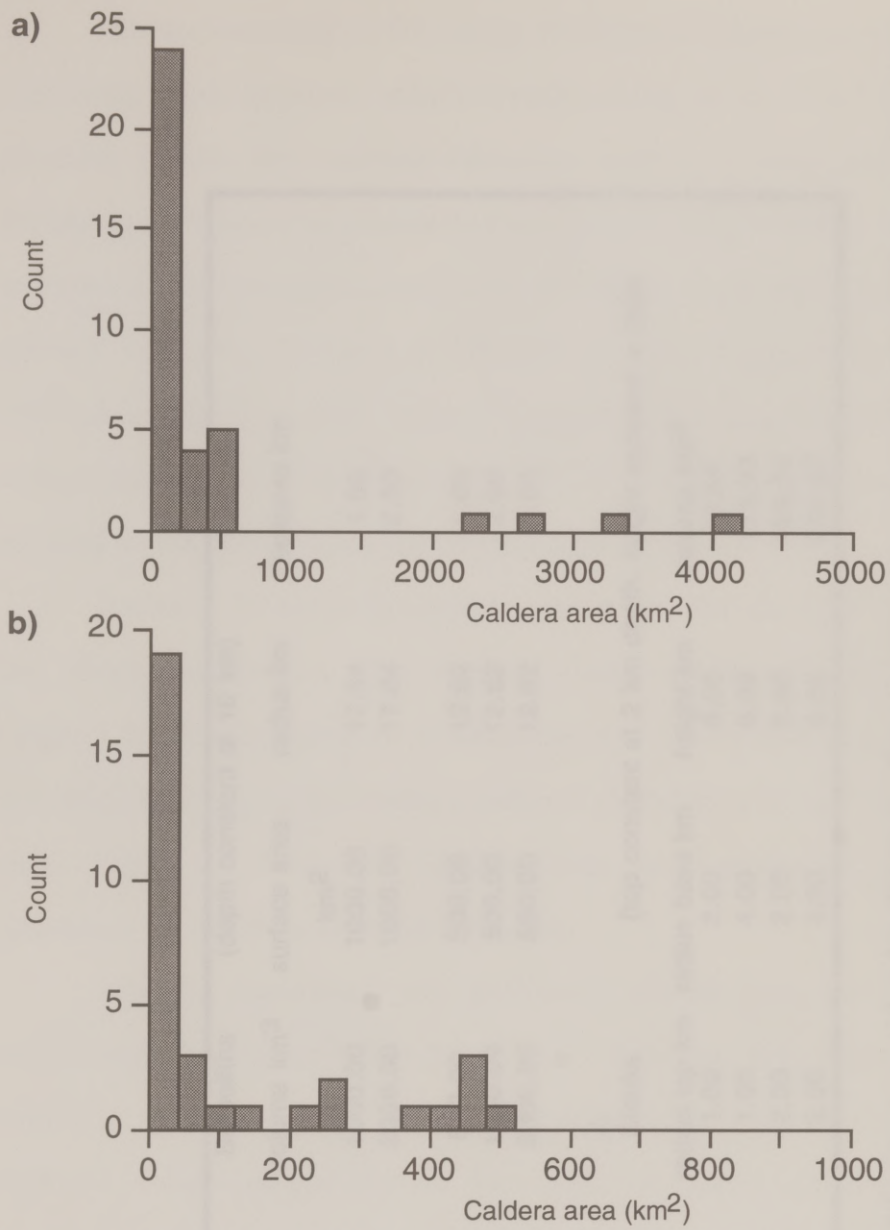


Figure 1.7: Caldera collapse structure area data used to choose model batholith size. Data from Smith, (1979), San Juan Mountains data omitted. The caldera areas are shown in figure (a), and range from < 1 $km^2$ to ~4000 $km^2$, but are seldom above 1000 $km^2$, as shown in (b), a detail of the same data set.

| Case | Batholiths | (depth constant at 10 km) | | |
|---|---|---|---|---|
| | Volume $km^3$ | surface area $km^2$ | radius km | thickness km |
| B | 1000.00 | 1000.00 | 17.84 | 1.00 |
| C | 2000.00 | 1000.00 | 17.84 | 2.00 |
| D | 500.00 | 500.00 | 12.62 | 1.00 |
| E | 1000.00 | 500.00 | 12.62 | 2.00 |
| F | 2000.00 | 500.00 | 12.62 | 4.00 |

| Sub-case | Stocks | (top constant at 2 km depth, height constant = 8km) | | |
|---|---|---|---|---|
| | radius top km | radius base km | height km | volume $km^3$ |
| 12 | 1.00 | 2.00 | 8.00 | 58.64 |
| 14 | 1.00 | 4.00 | 8.00 | 175.93 |
| 22 | 2.00 | 2.00 | 8.00 | 100.53 |
| 24 | 2.00 | 4.00 | 8.00 | 234.57 |

Table 1.2: Stock-batholith sytems considered in this study. Twenty geometries are considered, which are combinations of four stock and five batholith geometries. The thickness of the batholith is 1, 2 or 4 km, resulting in a range of volumes of 500, 1000 or 2000 $km^3$.

Another constraint on the volume of magma chambers may be obtained by calculating a mass balance of metals in a mineralized pluton. The Grasberg copper porphyry of Irian Jaya contains substantial reserves of both copper and gold. McMahon (1994) uses the amount of known metals in the intrusion, and a range of estimates of parental magma metal content to determine the necessary volume of a parental batholith. As much as 700 $km^3$ of parent magma may be required (McMahon, 1994, p. 937). Similar arguments for molybdenum porphyries indicate that a parental magma chamber of 10-150 times the volume of the stock is required for ore deposit formation (Shinohara et al., 1995).

Radius at the top of the stock is either 1 or 2 km, the base is either 2 or 4 km. Height is constant at 8 km, resultant volumes are 59, 101, 176 and 235 $km^3$ (Table 1.2). Model names are a combination of a letter denoting the batholith geometry, and two numbers corresponding to the radius at the top and base of the stock (Figure 1.5, Table 1.2). In all of these model geometries the confining pressure at the top of the batholith is ~2.5 kb. .

After the calculations were performed, contour plots were made of the temperature distribution within the pluton at each time step (Figure 1.8). The isotherms corresponding to the crystallization front (800°C, in this case) were digitized, and divided into sections. Each section is either a right circular cone, or the frustum of a right circular cone. The volume of revolution and the surface area can then be calculated analytically, and summed for the entire chamber (Figure 1.9). In this way the volume of remaining magma was determined at a series of time steps (Figure 1.10). The rate of crystallization can then be determined from the change in volume between steps.

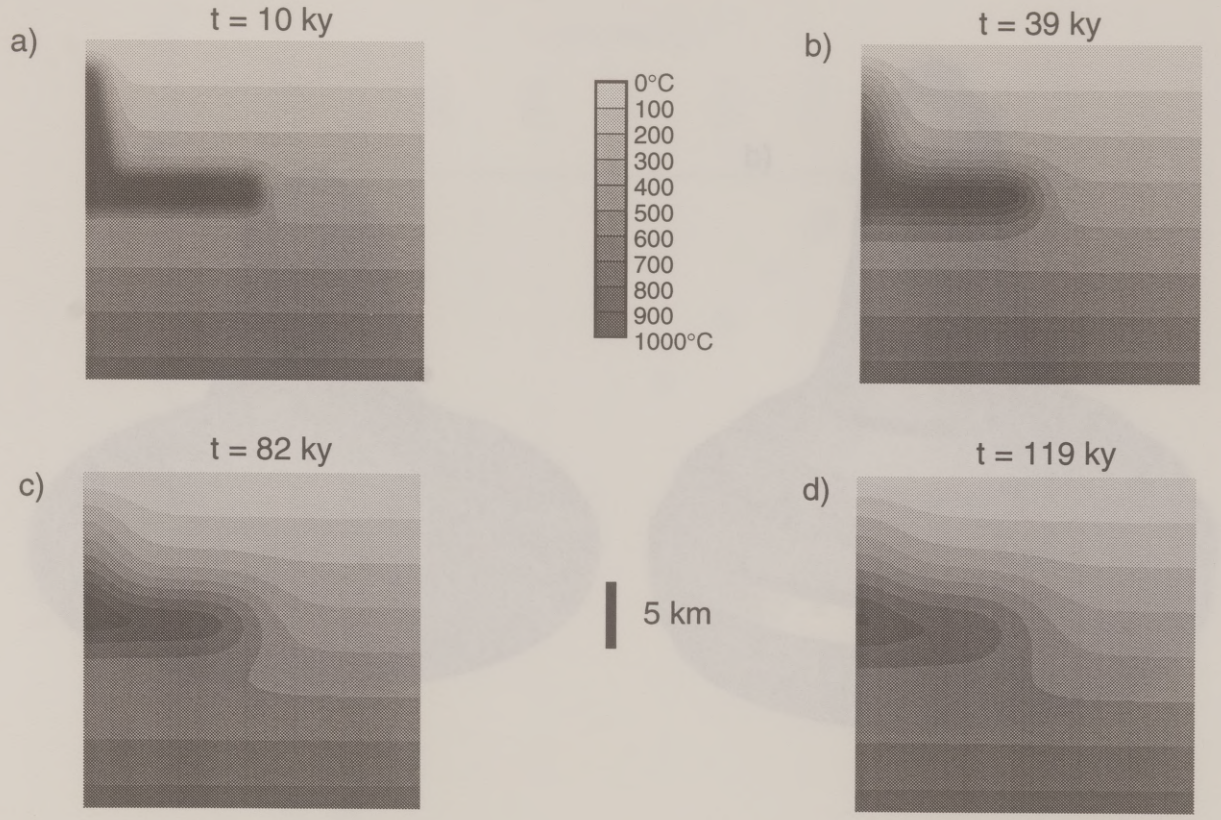


Figure 1.8: Contour of temperature for four calculation steps in model e12.

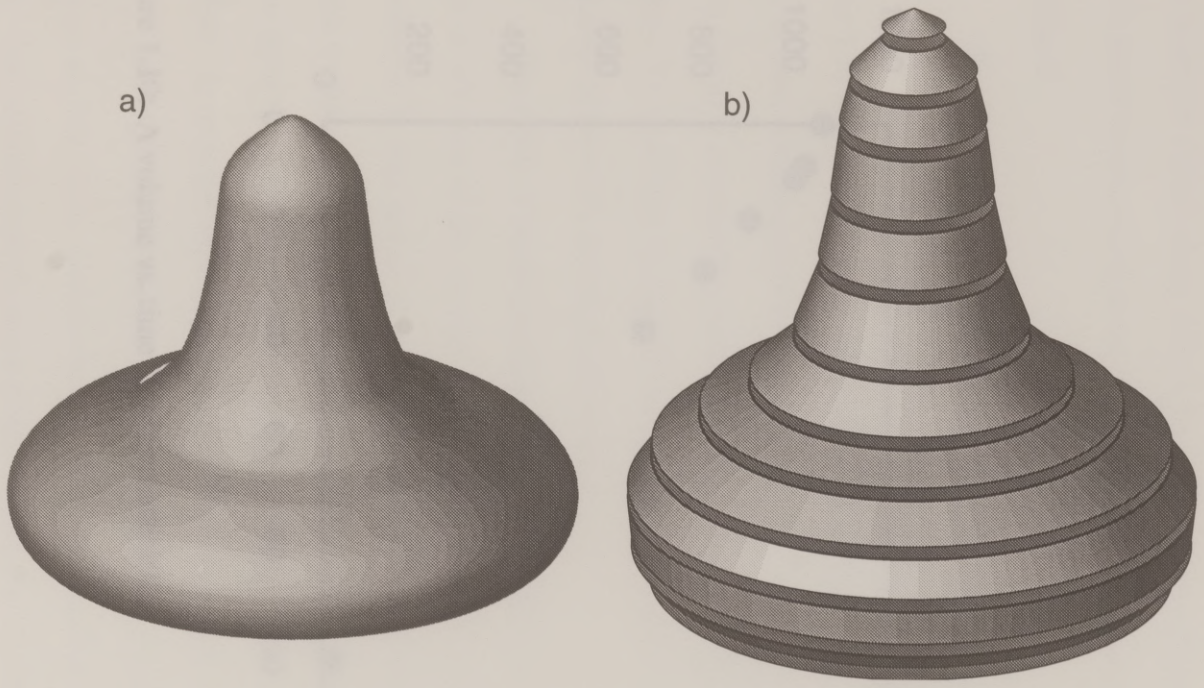


Figure 1.9: Method of volume calculation. The isotherm corresponding to the solidus is digitized, and revolved to form a solid (a). This is sliced up into discrete segments whose volume can be determined analytically (b).

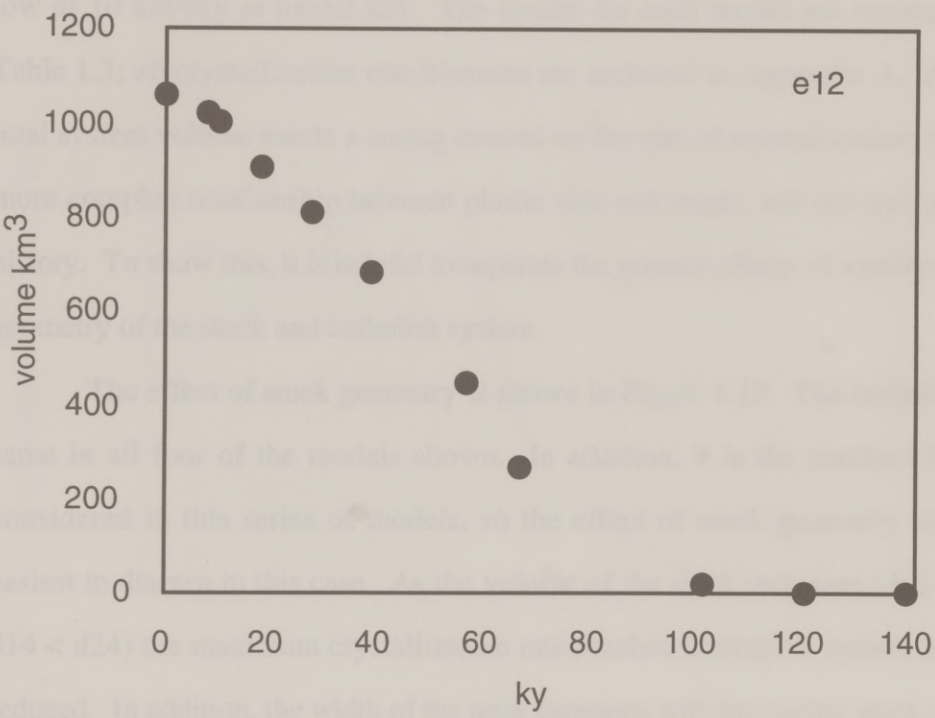


Figure 1.10: A volume vs. time plot for model e12.

Because this is a discrete approximation of a continuous process, the rate histories are sometimes difficult to compare directly. To facilitate comparison, a moving average (with a range of ±10% of the total data range) of the crystallization rate history is plotted along with the calculated rates (Figure 1.11). This makes the trends easier to see, while preserving the original calculations.

## RESULTS

Peak crystallization rates range from a high of 80 $km^3$/ky in model b14 to a low of 10 $km^3$/ky in model f24. The results for each model are summarized in Table 1.3; all crystallization rate histories are included in Appendix A. Although total system volume exerts a strong control on the rate of crystallization, there is a more complex relationship between pluton size and shape, and the crystallization history. To show this, it is helpful to separate the general effects of variations in the geometry of the stock and batholith system.

The effect of stock geometry is shown in Figure 1.12. The batholith is the same in all four of the models shown. In addition, it is the smallest batholith considered in this series of models, so the effect of stock geometry should be easiest to discern in this case. As the volume of the stock increases (d12 < d22 < d14 < d24) the maximum crystallization rate reached during the system history is reduced. In addition, the width of the peak increases with increasing stock volume.

The influence of the batholith is illustrated in Figure 1.13. The stock is the same in all five of the models shown, and is the smallest of the stocks considered here. The relation here is more complex than for the stocks in Figure 1.12. In comparing models b12 and c12 it is apparent that the effect of doubling the

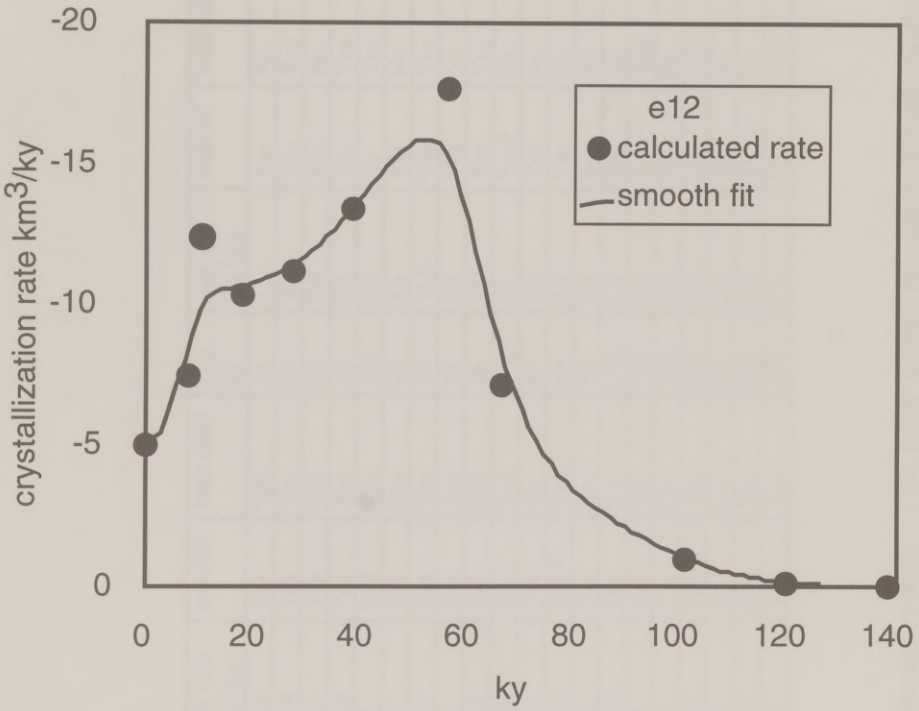


Figure 1.11: Rates calculated from data for model e12. Line is weighted average of points shown.

| model | volume of system $km^3$ | $t_{1/4}$ ky | rate $t_{1/4}$ $km^3$/ky | cupola? | batholith? | $t_{1/4}$ ky | rate $t_{1/2}$ $km^3$/ky | cupola? | batholith? | $t_{3/4}$ ky | rate $t_{3/4}$ $km^3$/ky | cupola? | batholith? |
|---|---|---|---|---|---|---|---|---|---|---|---|---|---|
| b12 | 1059 | 22 | 15.4 | Yes | Yes | 31 | 1.1 | Yes | No | 66 | 0.2 | No | No |
| c12 | 2059 | 27 | 20.0 | Yes | Yes | 56 | 43.3 | Yes | Yes | 104 | 0.7 | No | No |
| d12 | 559 | 22 | 12.1 | Yes | Yes | 46 | 0.8 | Yes | No | 66 | 0.2 | No | No |
| e12 | 1059 | 39 | 13.4 | Yes | Yes | 66 | 7.2 | Yes | Yes | 101 | 1.0 | No | No |
| f12 | 2059 | 122 | 7.4 | No? | Yes | 161 | 6.2 | No | Yes | 273 | 3.3 | No | Yes |
| b22 | 1101 | 23 | 8.6 | Yes | Yes | 46 | 1.4 | Yes | No | 83 | 0.1 | No | No |
| c22 | 2101 | 46 | 29.3 | Yes | Yes | 70 | 31.6 | Yes | Yes | 119 | 0.4 | No | No |
| d22 | 601 | 25 | 3.1 | Yes | Yes | 52 | 1.2 | Yes | No | 65 | 0.8 | Yes | No |
| e22 | 1101 | 34 | 13.8 | Yes | Yes | 66 | 17.0 | Yes | Yes | 104 | 1.3 | Yes | No? |
| f22 | 2101 | 82 | 6.4 | Yes | Yes | 172 | 6.1 | Yes? | No | 273 | 3.7 | No | No |
| b14 | 1176 | 37 | 2.0 | Yes | No | 83 | 1.2 | Yes | No | 124 | 0.5 | No | No |
| c14 | 2176 | 69 | 31.2 | Yes | Yes | 83 | 2.3 | Yes | No | 155 | 1.2 | No | No |
| d14 | 676 | 55 | 1.8 | Yes | Yes | 83 | 1.2 | Yes | No | 124 | 0.3 | No | No |
| e14 | 1176 | 46 | 14.6 | Yes | No | 103 | 1.8 | Yes | No | 155 | 1.2 | Yes? | No |
| f14 | 2176 | 88 | 6.5 | Yes | Yes | 163 | 6.6 | Yes | Yes | 317 | 2.5 | No? | Yes? |
| b24 | 1235 | 43 | 2.5 | Yes | No | 113 | 1.0 | Yes | No | 165 | 0.1 | No | No |
| c24 | 2235 | 72 | 16.1 | Yes | Yes | 134 | 1.8 | Yes | No | 197 | 0.8 | No | No |
| d24 | 735 | 38 | 2.2 | Yes | No | 81 | 1.6 | Yes | No | 164 | 0.2 | No | No |
| e24 | 1235 | 42 | 12.2 | Yes | Yes | 108 | 1.7 | Yes | No | 190 | 1.0 | No? | No |
| f24 | 2235 | 102 | 6.0 | Yes | Yes | 186 | 7.4 | Yes | Yes | 331 | 2.3 | No? | Yes? |

Table 1.3: Summary of model results. This table shows the state of each model at 1/4, 1/2, and 3/4 of the total time required for crystallization. At each of these time the crystallization rate is shown, the presence or absence of a cupola is noted, and the existence of a partially molten zone extending out into the batholith is noted.

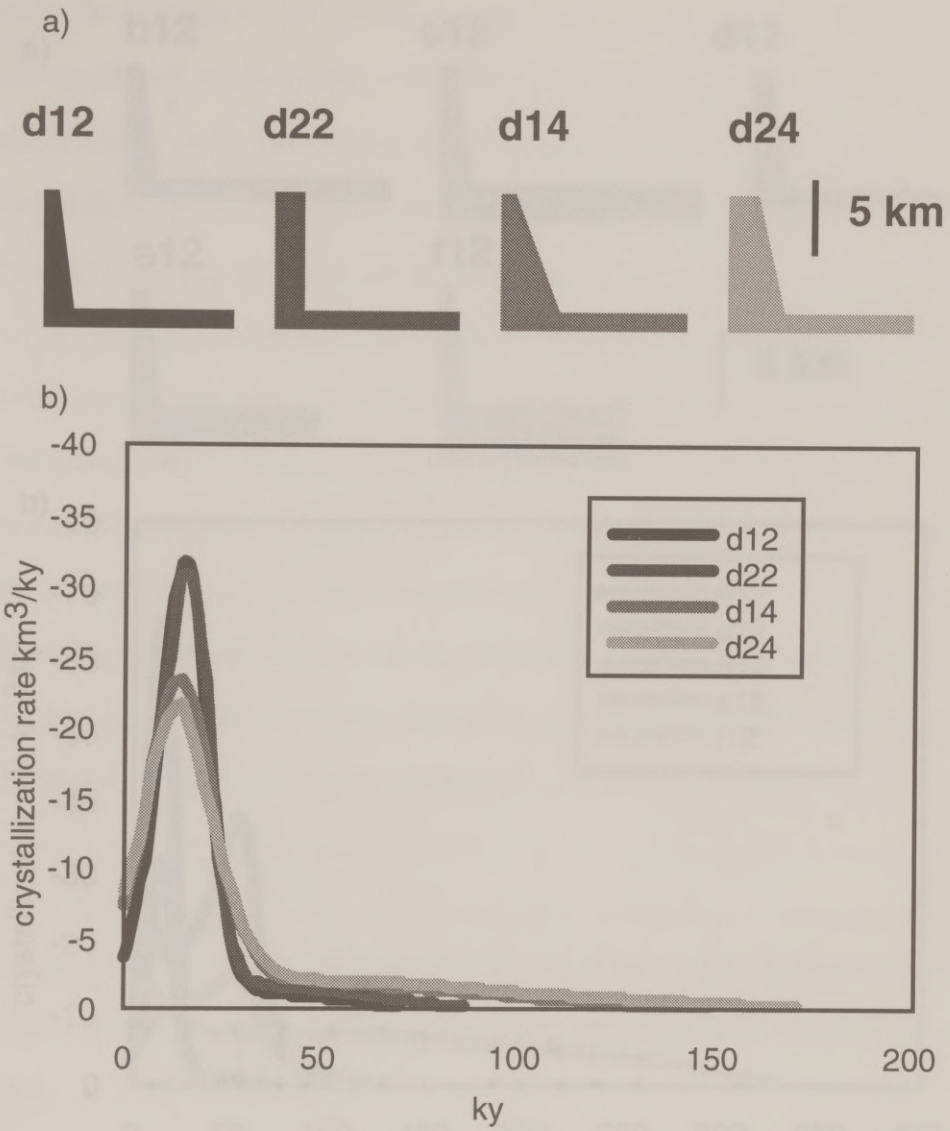


Figure 1.12: Effect of stock geometry on crystallization rates. The batholith is the same in all four of the models considered, and the geometries of the systems are shown in (a). The smoothed crytallization rate histories are shown in (b). As the volume of the stock increases (d12 < d22 < d14 < d24) the maximum crystallization rate reached during the system history is reduced.

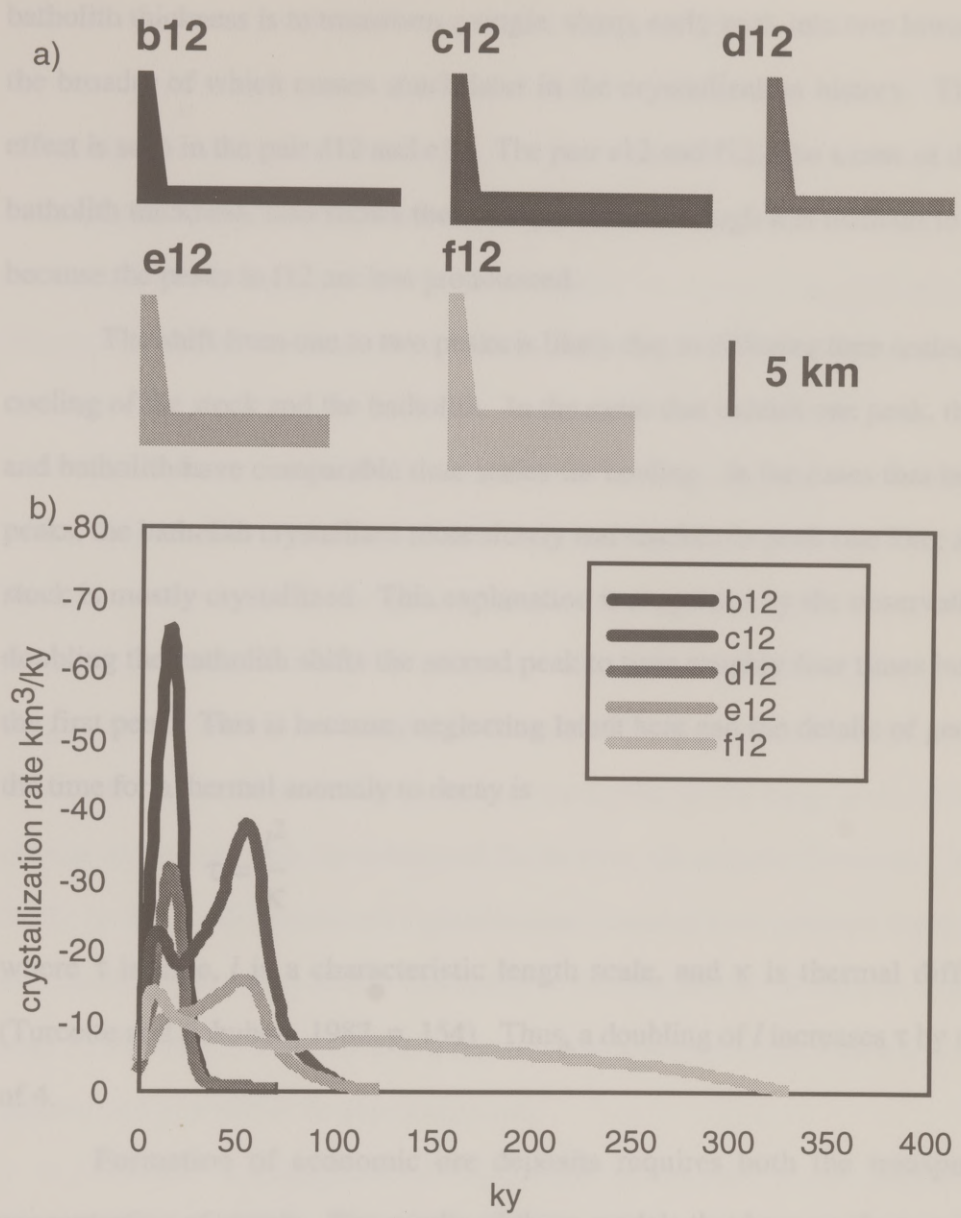


Figure 1.13: Effect of batholith geometry. The stock is the same in all five of the models shown, and the geometries of the systems are shown in (a). The smoothed crytallization rate histories are shown in (b). In general, the effect of doubling the batholith thickness is to transform a single, sharp, early peak into two lower peaks, the broader of which comes much later in the crystallization history.

batholith thickness is to transform a single, sharp, early peak into two lower peaks, the broader of which comes much later in the crystallization history. The same effect is seen in the pair d12 and e12. The pair e12 and f12, also a case of doubling batholith thickness, also shows the same patterns, although it is difficult to discern because the peaks in f12 are less pronounced.

The shift from one to two peaks is likely due to differing time scales for the cooling of the stock and the batholith. In the cases that exhibit one peak, the stock and batholith have comparable time scales for cooling. In the cases that have two peaks, the batholith crystallizes more slowly and reaches its peak rate long after the stock is mostly crystallized. This explanation is supported by the observation that doubling the batholith shifts the second peak to time roughly four times later than the first peak. This is because, neglecting latent heat and the details of geometry, the time for a thermal anomaly to decay is

$$\tau = \frac{l^2}{\kappa}$$

where $\tau$ is time, $l$ is a characteristic length scale, and $\kappa$ is thermal diffusivity (Turcotte and Schubert, 1982, p. 154) Thus, a doubling of $l$ increases $\tau$ by a factor of 4.

Formation of economic ore deposits requires both the transport and concentration of metals. The results of these models that bear on these processes are the rate of fluid production and the degree to which the shape of the crystallizing chamber provides a means of focusing the produced fluids.

The rate of crystallization (and consequent fluid production) is important because it determines the mechanism by which produced fluids will be transported.

If fluids are produced slowly, they are likely to leave the chamber by diffuse flow into the surrounding country rock. More rapid fluid production is likely to cause an accumulation of fluid in pockets, if there is a physical means of transport and a magma chamber geometry which favors concentration. Once this accumulation occurs hydraulic fractures may form. Because transport through fractures is an inherently concentrated from of fluid flow, this may favor the development of ore deposits.

Most workers believe that magmatic fluid driven hydraulic fracturing is the critical process in formation of ore deposits. Burnham (1979) postulated the formation of a shallow, water saturated, stock which is sealed from wall rock interaction by a ductile shell, or 'carapace'. Within the carapace, cooling continues, driving crystallization and exsolution of water. This process releases heat (the heat of crystallization) and does mechanical work, due to the large positive volume change associated with the release of fluids from the magma (Burnham, 1979, p. 110). In this model continued crystallization causes a fluid pressure build up that eventually results in hydraulic fracturing at shallow levels. If mineral deposition seals the fracture, a build-up, fracturing and deposition cycle can create a brecciated mineralized pipe above the top of the stock.

Another consequence of rapid fluid production is the possibility of developing an accumulation of fluid at the top of the magma chamber. If the rate of fluid production is higher than the rate of diffusive escape, a pocket of fluid can grow at the top of the magma chamber. Recent conceptual models of ore deposit formation invoke the formation of fluid pockets in the formation of mineral deposits (Candela, 1991; Giggenbach, 1992). Formation of such pockets probably

requires a domal roof or 'cupola' on top of the crystallizing magma chamber that facilitates the physical concentration of fluids.

Another view of the mineralization process (Cloos et al., 1995) proposes an additional condition necessary for formation of ore deposits. In this view, the accumulation of fluid inside the ductile carapace (or 'cupola') commonly continues to the point of catastrophic failure, that is, an explosive volcanic eruption. To form ore deposits, some method of systematically draining the fluid pocket in a controlled manner is necessary. Cloos et al. (1995) proposed tectonically created permeability as a key factor in releasing and focusing magmatically derived fluids into small regions that can become ore deposits.

If the formation of fluid pocket is important, it seems likely that the shape of the magma chamber during the fluid production period will have a strong influence on the mineralizing potential of a magmatic system. A cupola forms wherever there is an upward projection of the magma chamber into the overlying country rock or solidified magma. Gravity will drive buoyant bubbles of exsolved fluid upward through the liquid magma or crystal mush to accumulate in the cupola. Bubble transport is feasible on the spatial and temporal scales considered here (<10 km, >10 ky). A 1 cm radius water vapor bubble may ascend at 2 km/ky in a silicic melt, and transport through a porous network of bubbles may be much faster (Candela, 1991; Shinohara et al., 1995). The fluid accumulation thus formed can be an initiation point for hydraulic fracturing (Burnham, 1979) or could be tapped by tectonically created permeability (Cloos et al., 1995).

The combination of crystallization rate and magma chamber geometry has a strong influence on the geological effects of exsolved fluids, ranging from a slow

diffuse discharge producing little or no mineralization, to rapid, concentrated discharge that could drive an eruptive volcano. Three end member models are illustrated here. All three have the same material properties, initial conditions and boundary conditions. They differ only in the geometry of the stock-batholith system.

Model c22 (Figure 1.14a, b) is an example of a system that is likely to produce eruptive volcanoes and is capable of producing high-grade, vein-hosted mineral deposits. Fluid production is rapid (Figure 1.14b), and the magma chamber geometry provides a focusing point. This model intrusion crystallizes rapidly, reaching a peak rate of approximately 40 $km^3$/ky about halfway through the crystallization history of ~ 150 ky. A pronounced tall narrow cupola is maintained past 1/2 of the total crystallization time, throughout the period of high fluid production. An incompletely crystallized zone extends downwards and outwards into the batholith, allowing upwards bubble transport of deep-derived fluids into a shallow cupola. Because partitioning of Cu into an aqueous fluid is greater at higher pressures, maintaining connectivity with deep-seated crystallization may be a critical requirement for the formation of copper porphyry deposits. Rich Cu deposits may only form where shallow pooling of fluids exsolved at >2 kb has occurred (see Cu partitioning models of Candela and Holland, 1984; Cline and Bodnar, 1991).

Model f12 (Figure 1.15a, b) is a system which, although it is massive and will exsolve large amounts of fluid, is unlikely to concentrate fluids or transport them to shallow depths. Crystallization is slow, requiring ~390 ky total. A peak of

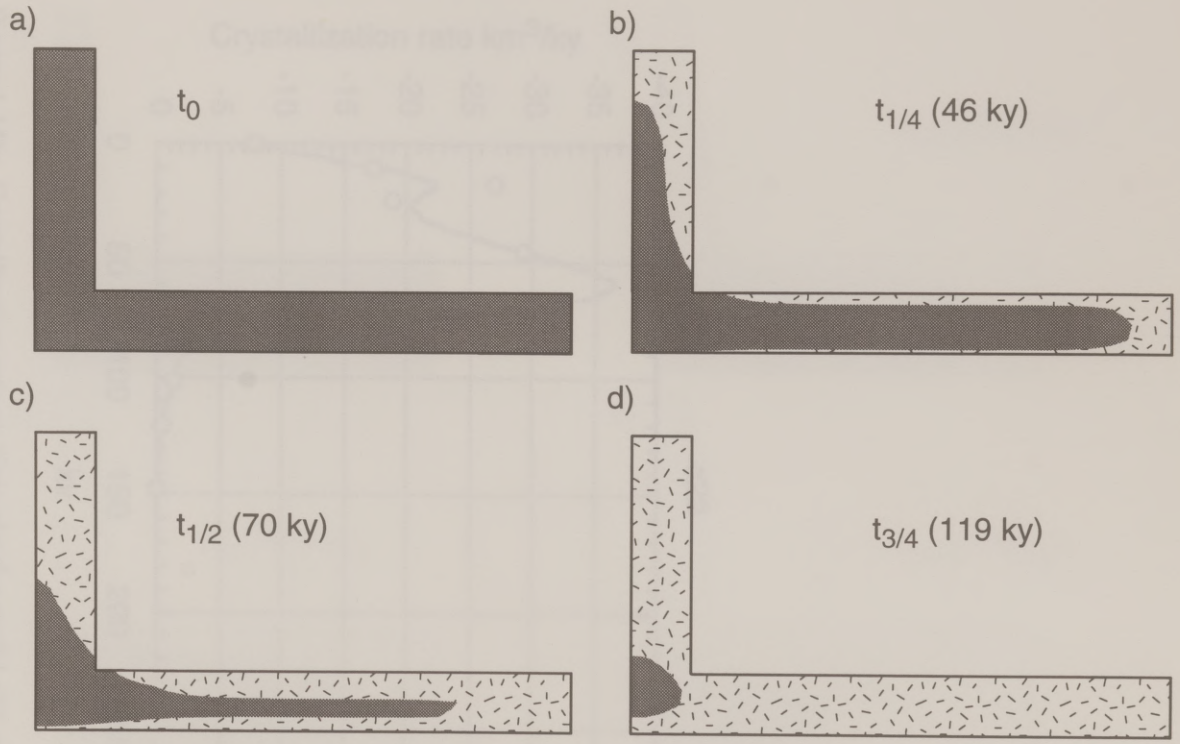


Figure 1.14a: Plot of progress of crystallization front with time. Grey region is above solidus (800°C), stippled region is below. This system evolves fluids rapidly, and provides a geometry capable of focussing them.

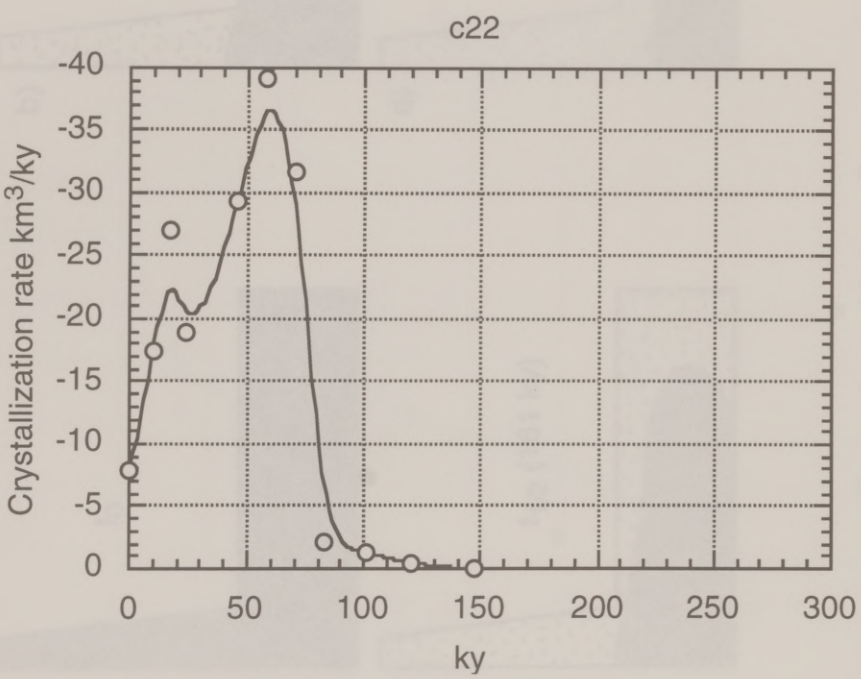


Figure 1.14b: Crystallization rate vs. time plot for model c22, to accompany Figure 1.14a. Circles are calculated crystallization rates, line is moving average of these values.

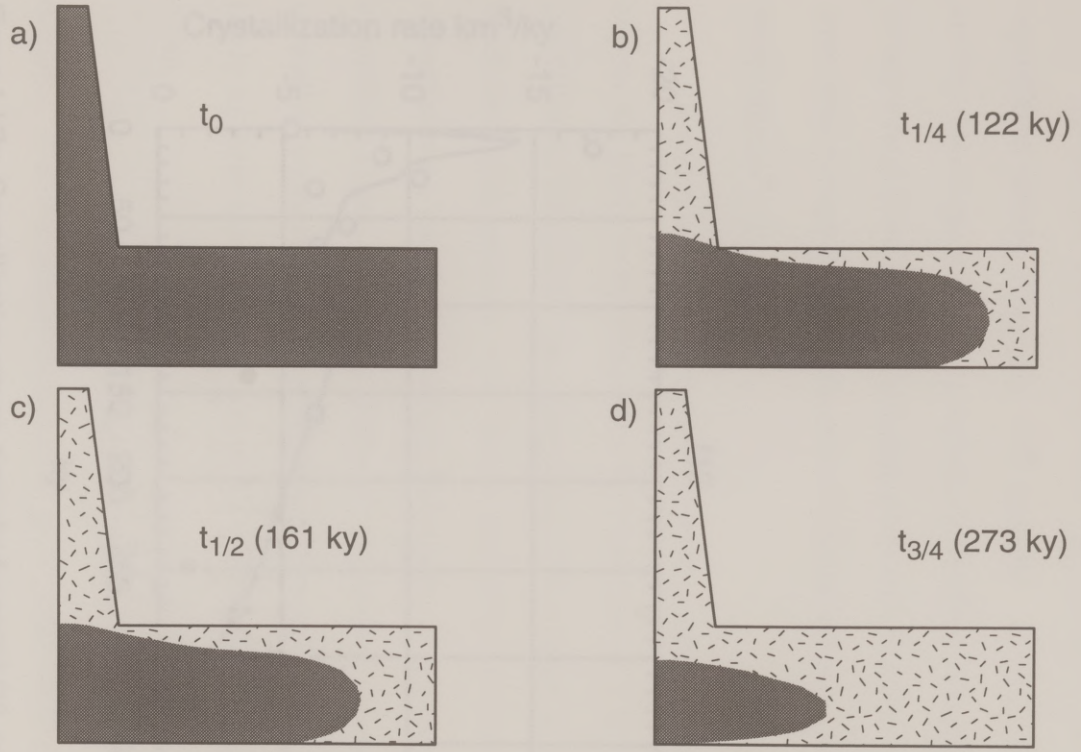


Figure 1.15a: Plot of progress of crystallization front with time. Grey region is above solidus (800°C), stippled region is below. This system evolves fluids rapidly, and provides a geometry capable of focussing them. Thisis a system which, although it produces a large quantity of fluid, is unlikely to efficiently concentrate fluids or transport them to shallow depths.

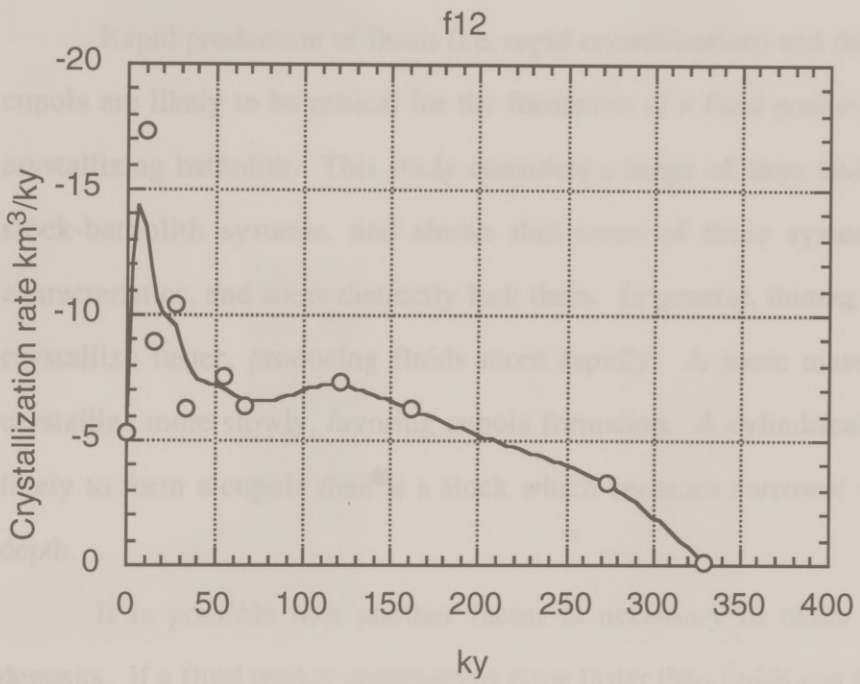


Figure 1.15b: Crystallization rate vs. time plot for model f12, to accompany Figure 1.15a. Circles are calculated crystallization rates, line is moving average of these values.

approximately 17 $km^3$/ky is attained shortly after intrusion. Any cupola is very short-lived, and there is no narrow cupola in which produced fluids could pool.

Model f24 (Figure 1.16a, b) is intermediate in its behavior. This model crystallizes slowly, requiring ~400 ky total. A peak rate of approximately 10 $km^3$/ky occurs early in the crystallization history. Nonetheless, the massive stock creates a long lived cupola, providing an area for fluids to accumulate if production were rapid enough to exceed the rate of leakage into the wall rock.

## DISCUSSION

Rapid production of fluids (i.e. rapid crystallization) and the existence of a cupola are likely to be critical for the formation of a fluid pocket at the top of a crystallizing batholith. This study considers a range of sizes and geometries of stock-batholith systems, and shows that some of these systems have these characteristics, and some distinctly lack them. In general, thinner batholiths will crystallize faster, producing fluids more rapidly. A more massive stock will crystallize more slowly, favoring cupola formation. A cylindrical stock is more likely to form a cupola than is a stock which becomes narrower with shallower depth.

It is possible that another factor is necessary to make economic ore deposits. If a fluid pocket continues to grow faster than fluids can be released, the buoyant fluid bubble will grow to the point of catastrophic failure, that is, an explosive volcanic eruption. Economic volcanogenic deposits do exist, however it is not likely that they formed by explosive sub-aerial processes.

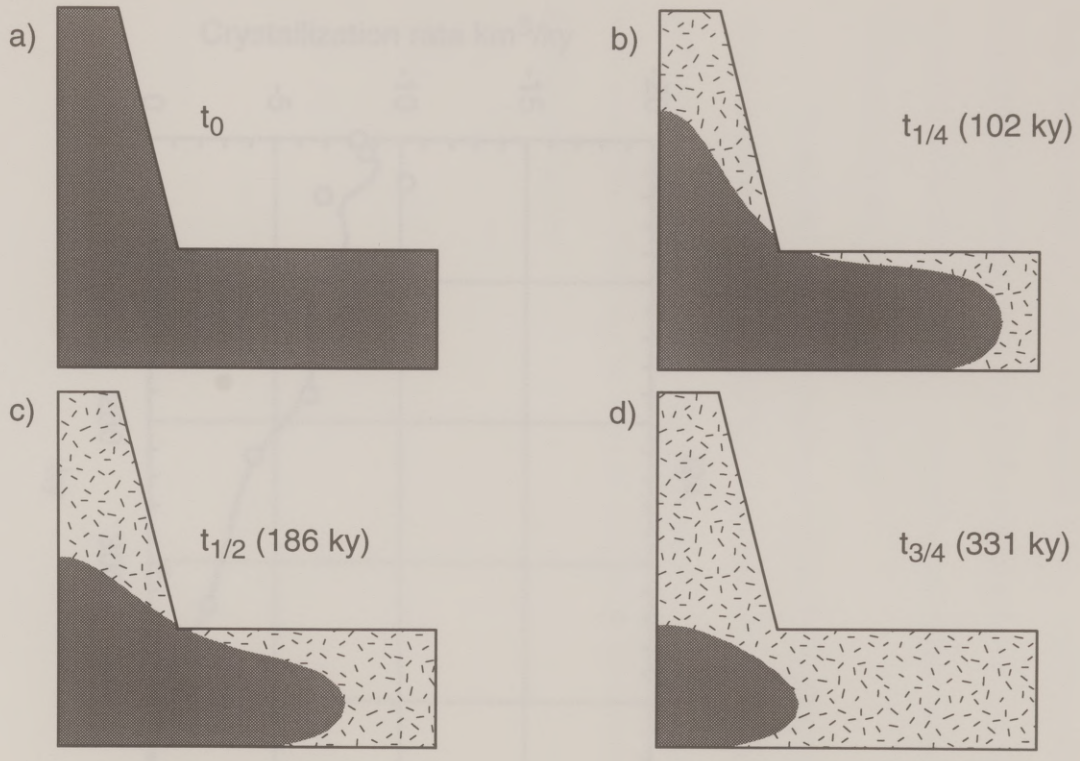


Figure 1.16a: Plot of progress of crystallization front with time. Grey region is above solidus (800°C), stippled region is below. This system evolves fluids rapidly, and provides a geometry capable of focussing them. This model is intermediate in its behavior. This model crystallizes slowly, with a peak rate of approximately 10 $km^3$/ky occurring early in the crystallization history. Nonetheless, the massive stock creates a long lived cupola, providing an area for fluids to accumulate if production were rapid enough.

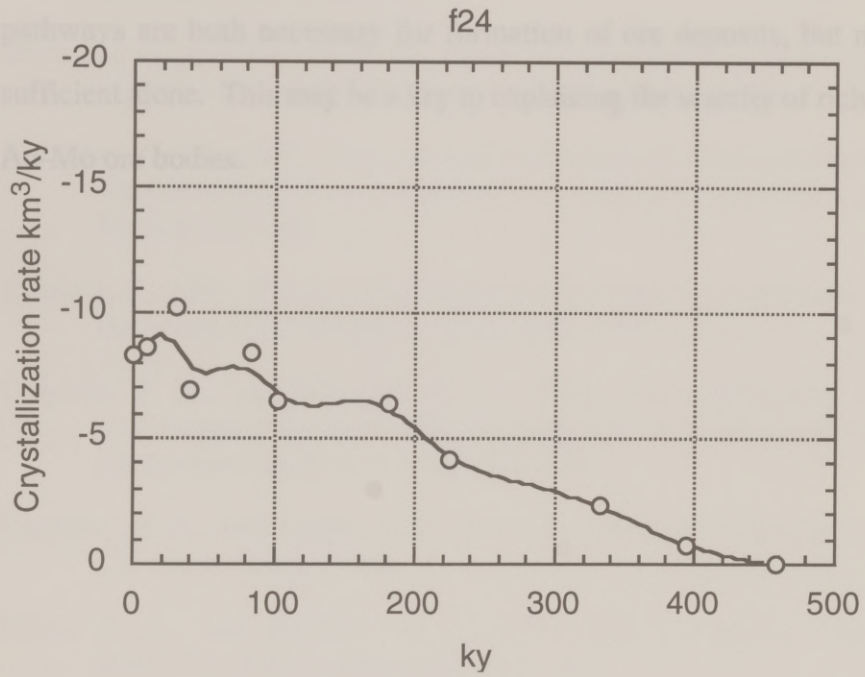


Figure 1.16b: Crystallization rate vs. time plot for model f24, to accompany Figure 1.16a. Circles are calculated crystallization rates, line is moving average of these values.

The coincidence of tectonic permeability with a rapidly charging fluid pocket may be the key to forming economic ore deposits. Episodic tapping of the fluid bubble could prevent catastrophic failure, and feed pulses of metal-rich fluids into fractures forming vein deposits at shallow levels. In addition, an environment of active extensional tectonics, or a pull-apart within a strike-slip fault zone, seem likely to favor the formation of stocks.

In summary, the formation of a fluid-filled cupola (a function of magma chamber-size and shape) and the existence of tectonically created permeable pathways are both necessary for formation of ore deposits, but neither may be sufficient alone. This may be a key to explaining the scarcity of rich magmatic Cu-Au-Mo ore bodies.

## REFERENCES


Bates, R. L., and Jackson, J. A., 1987, Glossary of geology: Alexandria, American Geological Institute, 788 p.

Best, M. G., 1982, Igneous and metamorphic petrology: New York, W. H. Freeman, 630 p.

Bowers, J. R., Kerrick, D. M., and Furlong, K. P., 1990, Conduction model for the thermal evolution of the Cupsuptic aureole, Maine: American Journal of Science, v. 290, p. 644-665.

Brandeis, G., and Marsh, B. D., 1989, The convective liquidus in a solidifying magma chamber: a fluid dynamic investigation: Nature, v. 339, p. 613-616.

Burnham, C. W., 1979, Magmas and hydrothermal fluids, *in* Barnes, H. L., ed., Geochemistry of hydrothermal ore deposits: New York, John Wiley & Sons, p. 71-136.

Candela, P., 1991, Physics of aqueous phase evolution in plutonic environments: American Mineralogist, v. 76, p. 1081-1091.

Candela, P. A., and Holland, H. D., 1984, The partitioning of copper and molybdenum between silicate melts and aqueous fluids: Geochimica et Cosmochimica Acta, v. 48, p. 373-380.

Carslaw, H. S., and Jaeger, J. C., 1959, Conduction of heat in solids: Oxford, Clarendon Press, 510 p.

Cline, J. S., and Bodnar, R. J., 1991, Can economic porphyry copper mineralization be generated by a typical calc-alkaline melt?: Journal of Geophysical Research, v. 96, p. 8113-8126.

Cloos, M., Sapiie, B., and Penniston-Dorland, S., 1995, Formation of the Grasberg Cu-Au orebody, Irian Jaya, Indonesia: strike-slip faulting, cupolas, and bubbling magma chambers: Geological Society of America, Abstracts with Program, v. 27, p. A65.

Furlong, K. P., Hanson, R. B., and Bowers, J. R., 1991, Modeling thermal regimes, *in* Kerrick, D. M., ed., Contact Metamorphism: Reviews in mineralogy: Washington, Mineralogical Society of America, p. 437-505.

Giggenbach, W. F., 1992, Magma degassing and mineral deposition in hydrothermal systems along convergent plate boundaries: Economic Geology, v. 87, p. 1927-1944.

Hedenquist, J. W., and Lowenstern, J. B., 1994, The role of magmas in the formation of hydrothermal ore deposits: Nature, v. 370, p. 519-527.

Le Cloarec, M. F., Allard, P., Ardouin, B., Giggenbach, W. F., and Sheppard, D., S., 1992, Radioactive isotopes and trace elements in gaseous emissions from White Island, New Zealand: Earth and Planetary Science Letters, v. 108, p. 19-28.

Marsh, B. D., 1988, On convective style and vigor in sheet-like magma chambers: Journal of Petrology, v. 30, p. 479-530.

McMahon, T. P., 1994, Pliocene intrusions in the Gunung Bijih (Ertsberg) mining district, Irian Jaya, Indonesia: Major- and trace-element chemistry: International Geology Review, v. 36, p. 925-946.

Parmentier, E. M., and Schedl, A., 1981, Thermal aureoles of igneous intrusions: Some possible indications of hydrothermal convective cooling: Journal of Geology, v. 89, p. 1-22.

Rubey, W. R., 1951, Geologic history of sea water: Geological Society of America Bulletin, v. 62, p. 1111-1148.

Shinohara, H., and Kazahaya, K., 1995, Degassing processes related to magma-chamber crystallization, *in* Thompson, J. F. H., ed., Magmas, Fluids, and Ore Deposits: Short Course Series: Nepean, Mineralogical Association of Canada, p. 47-70.

Shinohara, H., Kazahaya, K., and Lowenstern, J. B., 1995, Volatile transport in a convecting magma column: implications for porphyry Mo mineralization: Geology, v. 23, p. 1091-1094.

Smith, R. L., 1979, Ash-flow magmatism, *in* Chapin, C. E., and Elston, W. E., eds., Ash-flow Tuffs: Boulder, Geological Society of America, p. 5-27.

Stüwe, K., 1995, Thermal buffering effects at the solidus. Implications for the equilibration of partially melted metamorphic rocks: Tectonophysics, v. 248, p. 39-51.

Turcotte, D. L., and Schubert, G., 1982, Geodynamics: New York, John Wiley and Sons, 450 p.

# Chapter 2: Forward models of porphyroblast growth and rotation and inclusion trail formation


## ABSTRACT

Trails of mineral inclusions within metamorphic porphyroblasts can provide useful kinematic information, but the interpretation of these structures is plagued by ambiguity. Spiral trails, or differences in orientation between internal and external foliations, can be interpreted as reflecting either differential rotation of porphyroblast and cleavage during growth, or as static overgrowth of earlier foliations. These contrasting interpretations have conflicting implications for the behavior of deforming rocks.

This paper presents a computer program that uses previously published descriptions of the rotation of rigid inclusions and potential foliation-forming planes to simulate the growth and rotation of porphyroblasts and cleavages. This program models synkinematic porphyroblast growth as a series of steps of growth and rotation. The porphyroblast is considered to be a rigid inclusion in a viscous matrix. As the porphyroblast grows it includes one of three model 'foliations'. Foliation may be the plane of maximum finite strain, maximum infinitesimal strain, or a preexisting passive marker. Both the finite and passive foliations may rotate as deformation proceeds. The program incorporates different growth laws in order to simulate growth in different metamorphic conditions. The porphyroblast

may grow by adding fixed increments of radius, surface area, or volume per unit time. Porphyroblasts may be equant or elongate.

Resultant inclusion trails are complex. This complexity is a result of the variable relative rates of rotation of the inclusion and the cleavage. Different growth laws cause the curvature of the trails to be distributed differently within the porphyroblast. In some cases foliations are generated that could easily be interpreted as an included crenulation cleavage; other cases give an apparent sense of rotation opposite to the actual rotation. Because complex patterns can be produced by simple input parameters this model has the potential to reconcile puzzling inclusion patterns with other structural and kinematic data.

## INTRODUCTION

An important goal for structural geologists is the determination of strain paths. This information can often provide insight additional to that from finite strain data, which can be the end result of an infinite variety of strain histories. Rigid porphyroblasts can preserve the foliation at intermediate stages in the strain history of a rock and have often been used to determine the kinematics of deformation. Consequently the attempt to obtain information about strain paths has become entwined with a debate over the behavior of rigid objects in a deforming medium.

When foliation within a porphyroblast is not parallel to external foliation a rotation is inferred. Often the internal foliation shows a sigmoidal or spiral pattern, which is assumed to be the result of simultaneous growth and rotation. Apparent rotations of porphyroblasts have been interpreted as representing two different deformation histories. One view (Spry, 1963; Rosenfeld, 1970; Williams and Schoneveld, 1981) is that apparent rotation of porphyroblasts results from actual rotation of porphyroblasts during growth in simple shear. The other view (Bell, 1985; Bell et al., 1992b) is that apparent rotation of porphyroblasts results from the reorientation of external foliation by pure shear.

Because the principles that govern the motion of particles in a deforming viscous medium have been quantified, this problem is suitable to computational experiments, and several have been published (Masuda and Mochizuki, 1989;

Bjørnerud and Zhang, 1994; Gray and Busa, 1994) . All of these previous studies consider spherical porphyroblasts.

Masuda and Mochizuki (1989) model the incorporation into a growing rigid spherical porphyroblast of passive marker planes in the surrounding matrix, which is a Newtonian viscous fluid deforming in simple shear. This model incorporates deflection of the marker planes adjacent to the porphyroblast. The sphere rotates at one-half the rate of simple shearing ( $\dot{\gamma}/2$ ), and grows by addition of increments of constant volume (dv/dt = constant). The matrix deforms according to the solution of Masuda and Ando (1988) for a rigid spherical inclusion in a Newtonian viscous matrix undergoing simple shear. The flow is deflected around the inclusion, leading to distortion of material lines in the adjacent matrix. In simple cases, with the marker planes initially parallel to the shear plane, the modeled porphyroblasts show an increase in curvature of the trails towards the outside of the sphere, due to the volumetric growth law. Also shown are cases in which the initial orientation of the marker planes is oblique to the shear plane. Because the rotation rate of the passive marker planes is variable, and the rotation rate of the porphyroblast constant, this can form complex inclusion trails, including reversals in the curvature of the resultant inclusion trail. This result is not surprising given the existing knowledge of the rotation of passive markers, which shows that a passive marker may rotate faster or slower than a spherical porphyroblast, depending on the orientation of the passive marker relative to the shear plane (Ghosh and Ramberg, 1976; Ghosh, 1993).

Bjørnerud and Zhang (1994) perform an analysis similar to Masuda and Mochizuki (1989), but extend it to investigate the effect of the degree of mechanical

coupling between the rigid porphyroblast and viscous matrix in simple shear. The matrix deforms according to the solution of Bjørnerud (1989) for a rigid spherical inclusion in a Newtonian viscous matrix undergoing simple shear. This solution seems to be essentially the same as that of Masuda and Ando (1988); Gray and Busa (1994, p. 576) have a detailed discussion of this issue, and of the development of descriptions of kinematics of deformation. As in Masuda and Mochizuki (1989), the flow is deflected around the inclusion, leading to distortion of material lines in the adjacent matrix. The porphyroblast in Bjørnerud and Zhang (1994) overgrows passive marker planes that are initially parallel to the shear plane. They show that curved inclusion trails may form even with no coupling (free slip along the porphyroblast-matrix boundary), as the porphyroblast overgrows foliation that is deflected around it. Episodic growth produces abrupt changes in inclusion trail curvature in their model.

Gray and Busa (1994) extend the analysis of simulated inclusion trails formed during simple shearing to three dimensions. The matrix deforms according to the solution of Einstein (1956) for a rigid spherical inclusion in a Newtonian viscous matrix. In the case of simple shearing, this solution is the same as those used in Masuda and Mochizuki (1989) and Bjørnerud and Zhang (1994), and again the flow is deflected around the inclusion, leading to distortion of material lines in the adjacent matrix. Gray and Busa (1994) consider a spherical porphyroblast fully coupled to its matrix, overgrowing passive marker planes initially parallel to the shear plane. Growth is by increment of constant radius, area, or volume. This model incorporates deflection of the marker planes adjacent to the porphyroblast. Slices through the modeled porphyroblast show complex patterns,

including some that look like the 'millipede' structures of Bell and Rubenach (1980), which those authors interpret as precluding a simple shear deformation history.

All of the models above have some features in common. They all consider spherical porphyroblasts, in simple shear, with passive marker foliations. Consideration of other shapes and foliations, however, can provide more fruitful and less ambiguous results (Fisher, 1990; Orange, 1990; Busa and Gray, 1992). The model presented here considers some more general cases.

## Model Design

This model is purely kinematic, relying on the descriptions of particle and foliation movement in simple shear, and combinations of pure and simple shear published in Ghosh and Ramberg (1976), and Ghosh (1982; 1993). This model is thus able to consider more general cases than some previous models, but at the expense of some realism. In particular, distortion of foliation by deflection of matrix flow around the porphyroblast is not modeled. This model assumes that the medium around the porphyroblast has a linear viscous rheology, that the porphyroblast is rigid, and that there is no slip along the interface between the two. Only the central inclusion trail is modeled.

This program simulates the formation of inclusion trails by calculating the orientation of porphyroblasts and foliations in progressive general shear. Foliation may be modeled as the plane of maximum finite strain, maximum infinitesimal strain, or as a preexisting passive marker. The strain history is divided into

increments, and particles of the foliation are included at each increment. Once a particle is included it rotates with the porphyroblast (Figure 2.1a).

To perform this simulation, it is necessary to have quantitative descriptions of all the structural elements involved, under all the conditions modeled. These are drawn from a variety of sources. The orientation ($\theta$) of the major axis of the infinitesimal strain ellipse for combined pure and simple shear is given by:

$$\theta = \frac{1}{2}\tan^{-1}\left(\frac{1}{2\,s_r}\right) \tag{2.1}$$

(Ghosh, 1982, equation 10) where $s_r$ is the ratio of the rate of pure shear to the rate of simple shear, that is:

$$s_r = \frac{\dot{\varepsilon}}{\dot{\gamma}} \tag{2.2}$$

In the case of simple shear only:

$$\lim_{s_r \to \infty}(\theta) = 45° \tag{2.3}$$

The orientation ($\theta'$) of the major axis of the finite strain ellipse for combined pure and simple shear is given by:

$$\tan 2\,\theta' = \frac{\frac{1}{s_r}\left(1 - \exp\left(-2\gamma s_r\right)\right)}{\left(\frac{1}{s_r}\sinh(\gamma s_r)\right)^2 + \left(\exp\left(2\gamma s_r\right) - \exp\left(-2\gamma s_r\right)\right)} \tag{2.4}$$

(Ghosh, 1982, equation 8) where $\gamma$ is simple shear strain. In the case of simple shear only, this is:

$$\tan 2\,\theta' = \frac{2}{\gamma} \tag{2.5}$$

(Ghosh, 1993). The rotation of a passive marker line in combined pure and simple shear is given by:

$$\tan\phi = \exp\left(2\gamma s_r\right)\tan\phi_0 + \frac{1}{2s_r}\left(\exp\left(2\gamma s_r\right) - 1\right) \tag{2.6}$$

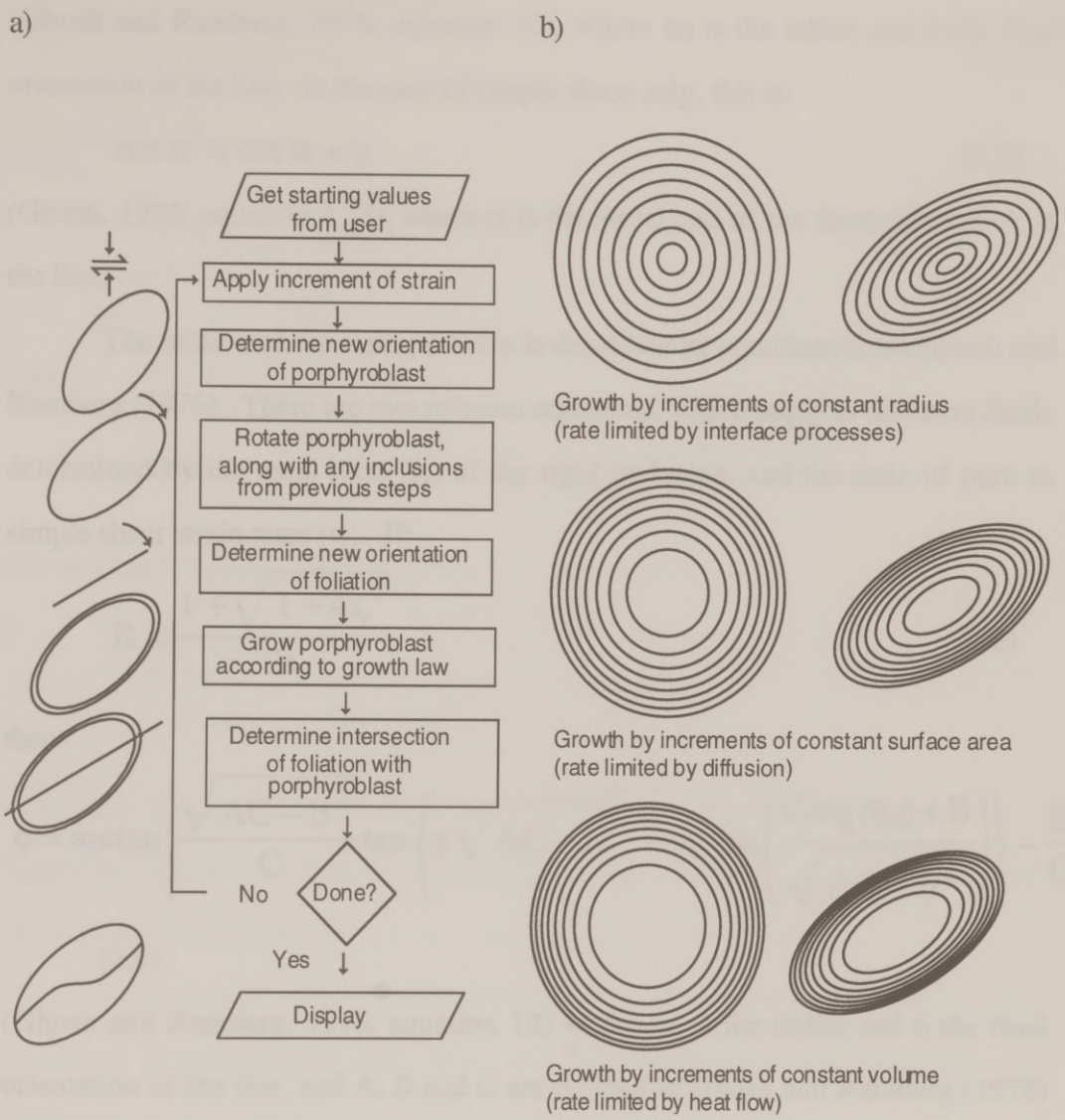


Figure 2.1. a: Flow chart showing general operation of program, which determines orientation of foliation and porphyroblast, and the intersection between the two at successive increments.
b: Effect of growth law, illustrated by growth rings, for porphyroblasts with circular or elliptical cross sections.

(Ghosh and Ramberg, 1976, equation 16), where $\phi_0$ is the initial and $\phi$ the final orientation of the line. In the case of simple shear only, this is:

$$\cot \alpha' = \cot \alpha + \gamma \tag{2.7}$$

(Ghosh, 1993, equation 8.73), where $\alpha$ is the initial and $\alpha'$ the final orientation of the line.

The motion of the rigid particles is described by equations from Ghosh and Ramberg (1976). There are two relevant equations, which apply in different fields determined by the axial ratio (R) of the rigid inclusion, and the ratio of pure to simple shear strain rates ($s_r$). If:

$$R < \frac{1 + \sqrt{1 + 4s_r^2}}{2s_r} \tag{2.8}$$

then

$$\phi = \arctan\left[\frac{\sqrt{AC - B^2}}{C}\tan\left\{\gamma\sqrt{AC - B^2} + \arctan\left(\frac{C\tan[\phi_0] + B}{\sqrt{AC - B^2}}\right)\right\} - \frac{B}{C}\right] \tag{2.9}$$

(Ghosh and Ramberg, 1976, equation 12) where $\phi_0$ is the initial and $\phi$ the final orientation of the line, and A, B and C are defined in Ghosh and Ramberg (1976) as:

$$A = \frac{R^2}{R^2 + 1} \tag{2.10}$$

$$B = \frac{s_r\left(R^2 - 1\right)}{R^2 + 1} \tag{2.11}$$

$$C = \frac{1}{R^2 + 1} \tag{2.12}$$

When:

$$R > \frac{1 + \sqrt{1 + 4s_r^{\,2}}}{2s_r} \tag{2.13}$$

then:

$$\phi = \arctan \frac{P\left(B + \sqrt{B^2 - AC}\right) - B + \sqrt{B^2 - AC}}{C(1 - P)} \tag{2.14}$$

(Ghosh and Ramberg, 1976, equation 11), where P is:

$$P = \frac{C\tan\phi_0 + B - \sqrt{B^2 - AC}}{C\tan\phi_0 + B + \sqrt{B^2 - AC}} \cdot \exp\left[2\gamma\sqrt{B^2 - AC}\right] \tag{2.15}$$

with A, B and C defined in equations 2.10, 2.11, and 2.12, respectively. These equations are valid for simple and combined simple and pure shear, and for equant and elongate inclusions.

The relative rates of porphyroblast growth and rotation determine the curvature of an inclusion trail. Variation of growth with time determines the geometry of that curvature. This program divides the strain history into equal increments. During each increment a shell of material must be added to the porphyroblast. This program allows an increment of constant radius, area, or volume. These options correspond to different geological scenarios. According to Carlson (1989), the constant radius growth corresponds to growth rate limited by interface processes, the constant area to growth rate limited by diffusion, and the

constant volume to growth rate limited by heat flow. These different growth laws make substantial differences in the growth pattern of the porphyroblast (Figure 2.1b). All of these options may be input by the user in a dialog; it is not necessary to reenter all the choices to rerun the analysis. This makes it easy to perform exploratory analysis (Figure 2.2). Results may be displayed as a series of points representing the intersection of the cleavage and porphyroblast at each growth increment, as a line connecting these points, or as a series of line segments corresponding to the cleavage segments captured during each growth increment.

## RESULTS

These calculations can produce simple patterns similar to classic porphyroblast textures (Figure 2.2). In some cases the inclusion trails constructed using these simple governing equations are complex (Figure 2.3). This is a result of the varying relative rates of rotation of the porphyroblast and foliation. Because the inclusion trail records the relative rotation of the porphyroblast and foliation, inclusion trails may show an apparent rotation larger or smaller than the true porphyroblast rotation (relative to a fixed external reference frame). Some cases preserve a sense of rotation opposite to the true rotation. In addition, the changing relative rate of rotation can cause reversals in the inclusion trail (also seen in Masuda and Mochizuki, 1989); which sometimes produces patterns that could be interpreted as included crenulation cleavages. Varying the growth law produces substantial changes in inclusion trail geometry. A porphyroblast will undergo the same rotation history regardless of growth law, but the curvature of the trail will be distributed differently within the porphyroblast (Figure 2.4). When growth is by

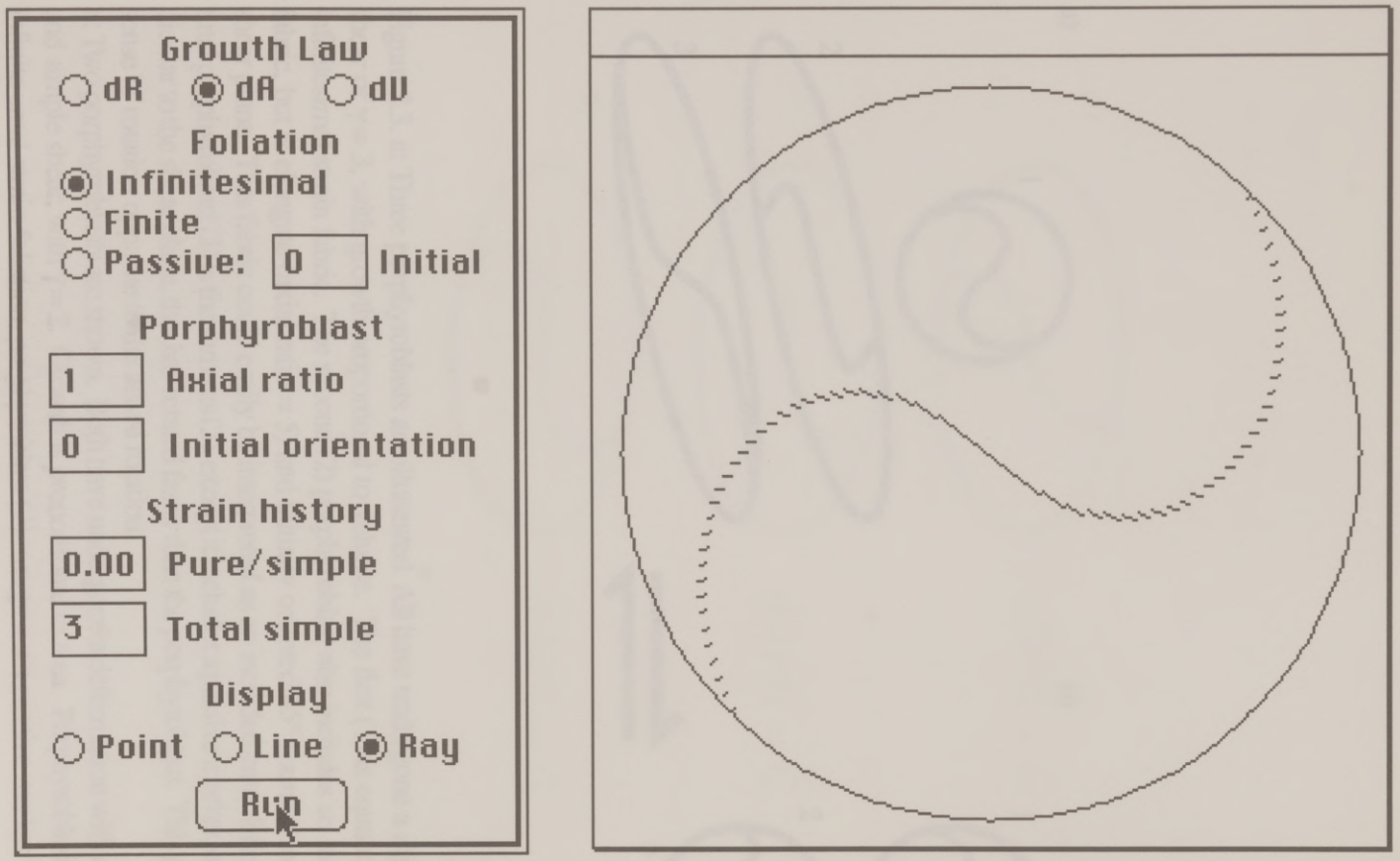


Figure 2.2. User interface of program, which allows users to rapidly investigate many combinations of input values, and immediately see the results. In this case simple shear of a spherical porphyroblast has produced a smoothly curving sigmoidal inclusion trail.

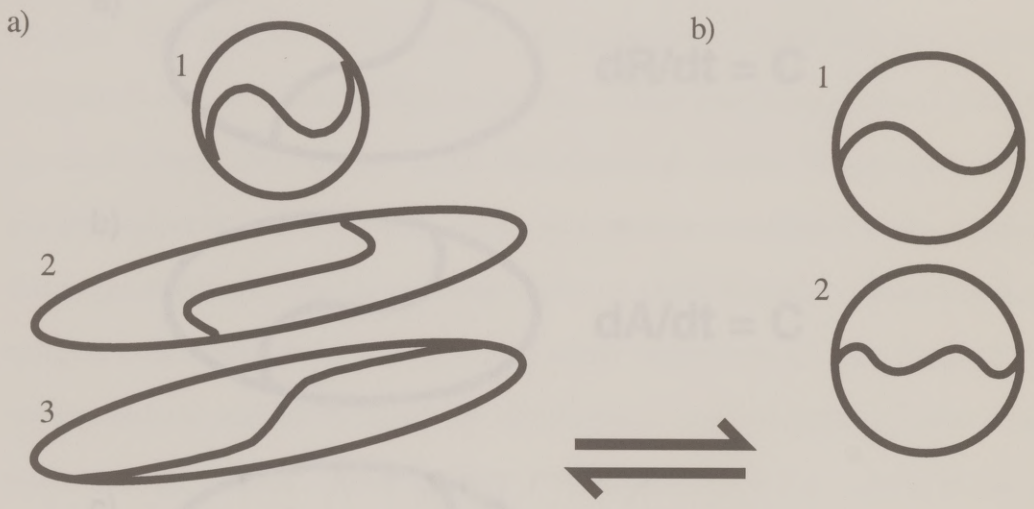


Figure 2.3. a: Three porphyroblasts are illustrated. All have undergone a right-lateral simple shear of $\gamma = 3$, with growth proportional to volume. The first (1) is equant and includes an infinitesimal strain fabric. The second (2) porphyroblast also includes an infinitesimal strain fabric, but is elongate (axial ratio = 5) and initially oriented 45° counterclockwise from the shear plane. This fabric could easily be interpreted as an included crenulation cleavage. The final porphyroblast (3) is the same as (2), except it includes a passive marker, originally perpendicular to the shear plane, that has rotated faster than the porphyroblast. This gives an apparent sense of rotation opposite to the actual rotation.
b: Two porphyroblasts are shown. Both have undergone a deformation with equal rate of pure and simple shear, with $\gamma = 2$. Growth is proportional to area. Porphyroblast (1) overgrows a infinitesimal strain foliation, porphyroblast (2) overgrows a passive marker foliation initially perpendicular to the shear plane.

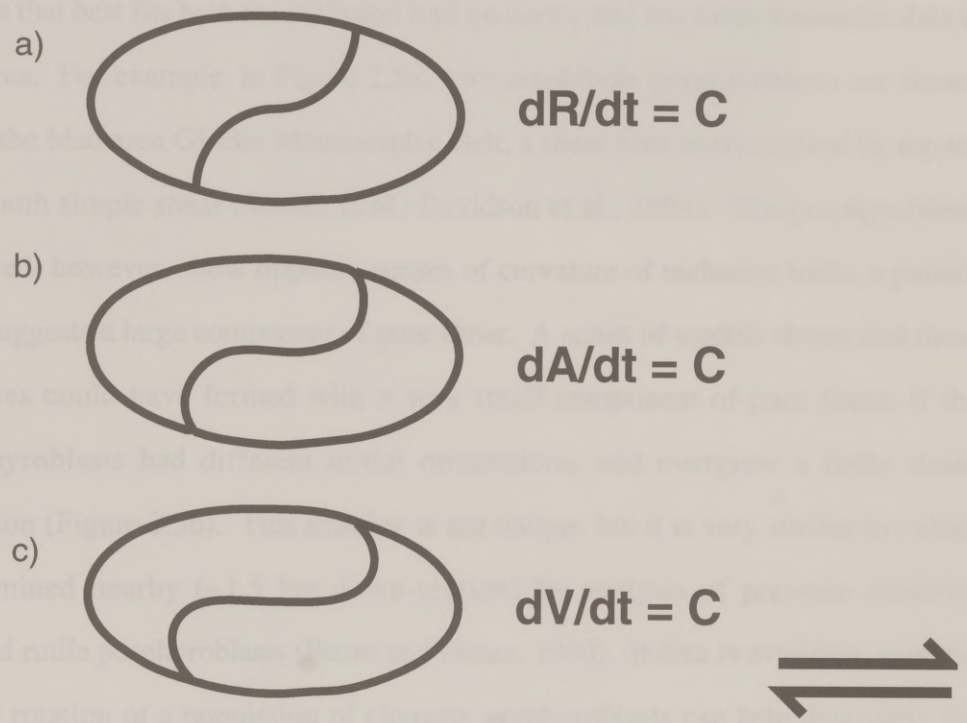


Figure 2.4. a: Three porphyroblasts are illustrated here. All have undergone a right-lateral simple shear of $\gamma = 3$, overgrowing an infinitesimal strain foliation. All have an axial ratio of 2, with the long axes initially oriented 45° counterclockwise from the shear plane. Porphyroblast (a) grows by increment of constant radius, porphyroblast (b) grows by increment of constant surface area, and porphyroblast (c) grows by increment of constant volume. The change in curvature from center to margin is more abrupt in (c), although all have identical rotation histories.

increments of constant volume, an abrupt change in curvature may be interpreted as a truncation. This has been used as a criterion for identifying non-rotated porphyroblasts (Bell et al., 1992a).

Because the user of this model can easily vary entered values, a rapid search of parameter space may be made, enabling the user to find the combination of values that best fits both the inclusion trail geometry and any other kinematic data in the area. For example, in Figure 2.5a, two amphibole porphyroblasts are shown from the Maclaren Glacier Metamorphic Belt, a shear zone characterized by top-to-the-south simple shear (Smith, 1981; Davidson et al., 1994). The porphyroblasts pictured, however, show opposite senses of curvature of inclusion trails, a pattern that suggests a large component of pure shear. A series of models shows that these textures could have formed with a very small component of pure shear, if the porphyroblasts had different initial orientations, and overgrew a finite strain foliation (Figure 2.5b). This solution is not unique, but it is very similar to values determined nearby (~1.5 km down-section) by analysis of pressure shadows around rutile porphyroblasts (Beam and Fisher, 1990). If data is available, analysis of the rotation of a population of elongate porphyroblasts can help determine the correct interpretation. In Chapter 3 this approach is used on the thin section shown in Figure 2.5a.

## CONCLUSIONS

Simple governing principles can result in complex inclusion trail geometries. Opposite senses of rotation can be explained by one deformation history. Abrupt changes in inclusion trail geometry are a natural result of

a)

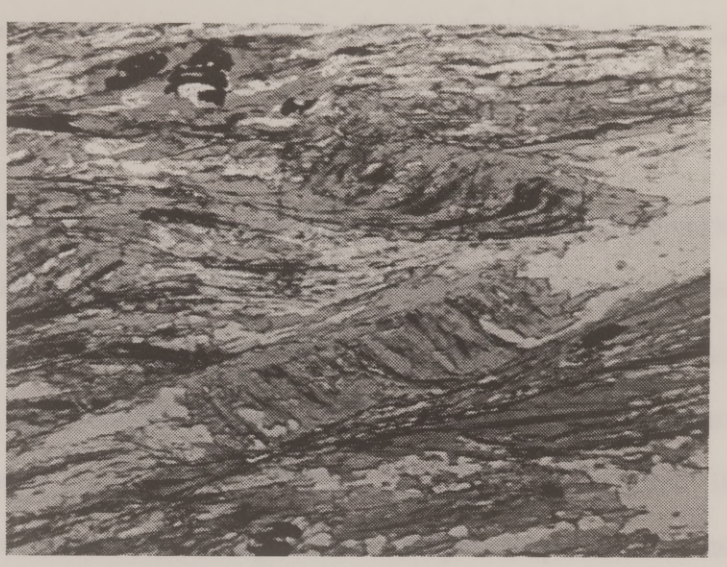

b)

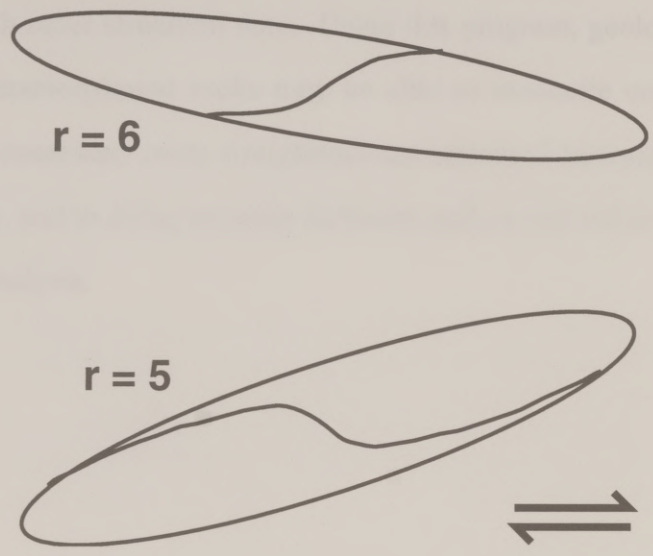


Figure 2.5. a: Two amphibole porphyroblasts from the Maclaren Glacier Metamorphic Belt, south-central Alaska. Trails are made up of inclusions of quartz and graphite. Long axis of photo ~ 2 mm.
b: One possible explanation of the observed texture. Both porphyroblasts have undergone the same strain history. The ratio of pure/simple shearing = 0.2, total simple shear ($\gamma$) = 2, foliation is long axis of finite strain ellipse. Growth is proportional to volume. The upper porphyroblast had an initial orientation close to the shear plane (10° clockwise), consequently it rotated slower than the finite strain foliation. The lower porphyroblast had an initial orientation far from the shear plane (90° counterclockwise); it rotated faster than the finite strain foliation.

porphyroblast growth laws, and of the shapes of porphyroblasts. Geometries that resemble included crenulations are easily produced by continuous growth and rotation.

Structural geologists may find that they are able to produce a coherent kinematic history that is consistent with all their observations except for inclusion trails. In light of this conflict, it is tempting to regard complex inclusion trails as a potential "... interpretative tool unrivaled by any other geometric or microstructural phenomenon..." (Bell, 1985, p. 115). However, it is more likely that the complexity of inclusion trails represents a complex response to a kinematic history consistent with other structural data. Using this program, geologists working in deformed, metamorphosed rocks may be able to reconcile complex inclusion patterns with somewhat more straightforward structural histories determined by other methods, and in doing so make inclusion trails a tool rather than an obstacle in kinematic analysis.

## REFERENCES


Beam, E. C., and Fisher, D. M., 1990, Rotation of elongate porphyroblasts in a shear zone, Kahiltna terrane, south central Alaska: Geological Society of America Abstracts with Program, v. 22, p. A183.

Bell, T. H., 1985, Deformation partitioning and porphyroblast rotation in metamorphic rocks: a radical reinterpretation: Journal of Metamorphic Geology, v. 3, p. 109-118.

Bell, T. H., Forde, A., and Hayward, N., 1992a, Do smoothly curving, spiral-shaped inclusion trails signify porphyroblast rotation?: Geology, v. 20, p. 59-62.

Bell, T. H., Johnson, S. E., Davis, B., Forde, A., Hayward, N., and Wilkins, C., 1992b, Porphyroblast inclusion-trail orientation data: eppur non son girate!: Journal of Metamorphic Geology, v. 10, p. 295-307.

Bell, T. H., and Rubenach, M. J., 1980, Crenulation cleavage development-evidence for progressive bulk inhomogeneous shortening from "millipede" microstructures in the Robertson River Metamorphics: Tectonophysics, v. 68, p. T9-T15.

Bjørnerud, M., 1989, Mathematical model for folding of layering near rigid objects in shear deformation: Journal of Structural Geology, v. 11, p. 245-254.

Bjørnerud, M. G., and Zhang, H., 1994, Rotation of porphyroblasts in non-coaxial deformation: insights from computer simulations: Journal of Metamorphic Geology, v. 12, p. 135-139.

Busa, M. D., and Gray, N. H., 1992, Rotated staurolite porphyroblasts in the Littleton Schist at Bolton, Connecticut, USA: Journal of Metamorphic Geology, v. 10, p. 627-636.

Carlson, W. D., 1989, The significance of intergranular diffusion to the mechanisms and kinetics of porphyroblast crystallization: Journal of Metamorphic Geology, v. 103, p. 1-24.

Davidson, C., Schmid, S. M., and Hollister, L. S., 1994, Role of melt during deformation in the deep crust: Terra Nova, v. 6, p. 133-142.

Einstein, A., 1956, Investigations on the theory of the Brownian movement: New York, Dover, 119 p.

Fisher, D. M., 1990, Orientation history and rheology in slates, Kodiak and Afognak Islands, Alaska: Journal of Structural Geology, v. 12, p. 483-498.

Ghosh, S. K., 1982, The problem of shearing along axial plane foliations: Journal of Structural Geology, v. 4, p. 63-67.

Ghosh, S. K., 1993, Structural Geology, Fundamentals and Modern Developments: Oxford, Pergamon, 598 p.

Ghosh, S. K., and Ramberg, H., 1976, Reorientation of inclusions by combination of pure shear and simple shear: Tectonophysics, v. 34, p. 1-70.

Gray, N. H., and Busa, M. D., 1994, The three-dimensional geometry of simulated porphyroblast inclusion trails: inert marker, viscous-flow models: Journal of Metamorphic Geology, v. 12, p. 575-587.

Masuda, T., and Ando, S., 1988, Viscous flow around a rigid spherical body: a hydrodynamical approach: Tectonophysics, v. 148, p. 337-346.

Masuda, T., and Mochizuki, S., 1989, Development of snowball structure: numerical simulation of inclusion trails during synkinematic porphyroblast growth in metamorphic rocks: Tectonophysics, v. 170, p. 141-150.

Orange, D. L., 1990, Criteria helpful in recognizing shear-zone and diapiric melanges: examples from the Hoh accretionary complex, Olympic Peninsula, Washington: Geological Society of America Bulletin, v. 102, p. 935-951.

Rosenfeld, J. L., 1970, Rotated garnets in metamorphic rocks: Boulder, Geological Society of America Special Paper 129, 105 p.

Smith, T. E., 1981, Geology of the Clearwater Mountains, South-central Alaska, Geologic Reports: Anchorage, Alaska Division of Geological and Geophysical Surveys, 72 p.

Spry, A., 1963, The origin and significance of snowball structure in garnet: Journal of Petrology, v. 4, p. 211-222.

Williams, P. F., and Schoneveld, C., 1981, Garnet rotation and the development of axial plane crenulation cleavage: Tectonophysics, v. 78, p. 307-334.

# Chapter 3: Inverse models of porphyroblast rotation, and strain distribution adjacent to a tonalite sill


## ABSTRACT

Biotite, garnet, and amphibole porphyroblasts are used to evaluate the sense of shear, magnitude of strain, and strain path (pure vs. simple shear) in deformed metamorphosed rocks adjacent to a tonalite sill in the Maclaren Glacier Metamorphic Belt, south-central Alaska. A theory that accounts for the variable rotation rate of elongate inclusions is used to estimate strain magnitude. The axial ratio of biotite porphyroblasts ranges from 1.35 to 8.56, that of garnet from 1.09 to 1.69, and that of amphibole from 2.47 to 5.56.

Inclusions of quartz and graphite inside these minerals form an internal foliation ($S_i$) that is often curved, and discordant with the external foliation ($S_e$). Measurements of the difference between $S_i$ and $S_e$, the axial ratio of the porphyroblast, and the orientation of the long axis of the porphyroblast are related to a theory predicting the behavior of elongate rigid inclusions in general shear.

Six thin sections with multiple porphyroblasts containing curved inclusion trails, collected over a traverse from 2.4 to 1.3 km away from the sill contact, are analyzed. Mean strains for entire thin sections yield $\gamma$ (finite simple shear strain) ranging from 2.4 to 3.3. Strains determined from biotite increase towards the sill. Strains recorded in garnet are lower than those determined from biotite porphyroblasts in the same thin section. The amphibole sample closest to the

intrusion was deformed in a flow that had equal components of pure and simple shear.

Peak metamorphic temperatures in these rocks increase towards the sill, based on garnet-biotite thermometry measurements by previous workers. The coincidence of the strain and temperature gradients supports the hypothesis that the thermal effects of the intrusion focused strain in the adjacent rocks.

## INTRODUCTION

This chapter presents strain data from the Maclaren Glacier Metamorphic Belt (MGMB), where a ~1 km-thick sill was emplaced in the Late Cretaceous and deformed while still hot. Analysis of inclusion trails in mineral porphyroblasts constrain the amount of strain, and the ratio of pure to simple shear in this regional shear zone. Because both temperature and strain gradients are exhibited in the MGMB it may be an appropriate site for the evaluation of the geologic applicability of theoretical thermal/strain models.

Samples were collected in the Clearwater Mountains of south central Alaska. The MGMB there comprises a well documented, deep–seated (~20 km) shear zone which makes up an inverted metamorphic sequence in the pelitic rocks of the Kahiltna terrane (Smith, 1981; Davidson, 1991; Davidson and Hollister, 1992). These flysch deposits mark the boundary between the Wrangellia oceanic basalt plateau and North America (Nokleberg et al., 1985; Wallace, 1989), and the shear zone records some of the convergent history of this boundary.

## BRIEF TECTONIC BACKGROUND: THE MGMB AND THE ACCRETION OF WRANGELLIA

The distinctive stratigraphy and low latitude paleomagnetic signature of the Wrangellia terrane make it one of the most compelling cases for the accretion of a major oceanic terrane. Fragments of Wrangellia are exposed as far south as Vancouver Island and as far east as Hells Canyon, Idaho (Jones et al., 1977; Jones et al., 1986), while some fragments were translated northward along post-accretion

strike–slip faults as far north as the western Clearwater mountains (Silberling et al., 1981; Silberling et al., 1987), where a study of 28 samples of Triassic basalt yielded a paleolatitude of 15.5 ±11.8°. This corresponds to a minimum paleolatitude anomaly of 26.8 ±12.3° with respect to North America (Stone et al., 1982; Hillhouse, 1987). In another study in the eastern part of the area of this investigation, samples from seven basalt flows indicated a paleolatitude of 18°, a minimum paleolatitude anomaly of 25° with respect to North America (Hillhouse and Grommé, 1984).

Based on a compilation of paleomagnetic data from the region, Hillhouse (1987) concluded that the rocks of Wrangellia were accreted to North America between 100 and 55 Ma, most likely around 65 Ma. Flysch basins of Jurassic-Cretaceous age form the Kahiltna terrane along the inboard boundary Wrangellia (Figure 3.1). The Late Cretaceous deformation, plutonism, and metamorphism of the MGMB appears to be a manifestation of the accretion of Wrangellia to North America.

### Recent Work

The MGMB is an well-characterized area of inverted metamorphic zonation and syntectonic plutonism. A series of studies (Smith, 1981; Davidson, 1991; Davidson and Hollister, 1992) have documented the close association of plutonism and deformation in schists and gneisses, and an increase in metamorphic temperatures with higher structural level, approaching the sill. These workers also identify south-directed simple shear in the metamorphosed rocks.. Regional dip is to the north, and the metamorphic facies of pelitic rocks increases progressively

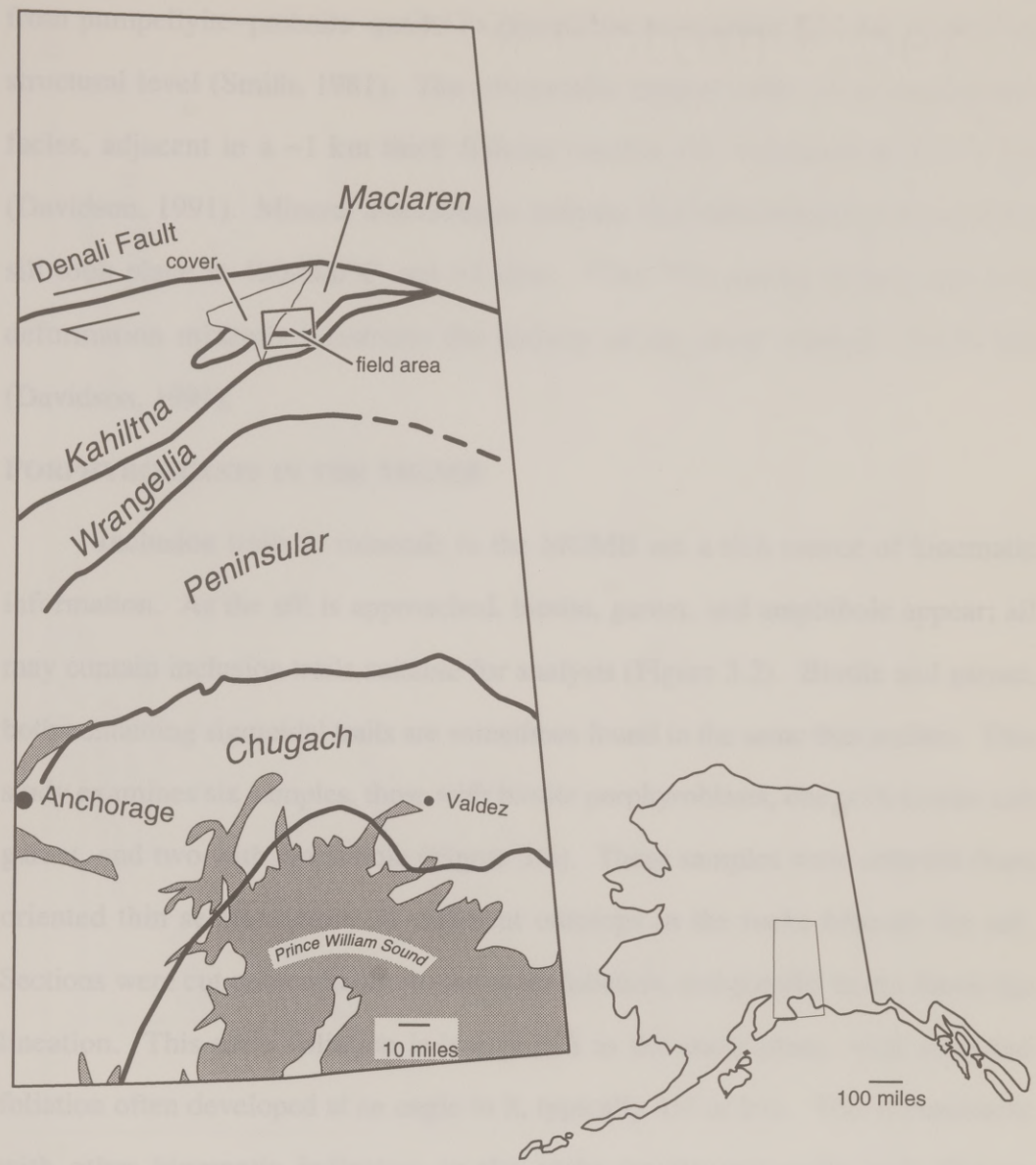


Figure 3.1: Terrane map of south central Alaska, showing study location at the northern edge of Wrangellia. Modified after Silberling et al. (1987).

from pumpellyite–prehnite–quartz to greenschist to amphibolite with increasing structural level (Smith, 1981). The structurally highest rocks are at amphibolite facies, adjacent to a ~1 km thick foliated tonalite sill, emplaced at 78–74 Ma (Davidson, 1991). Mineral assemblages indicate that metamorphism beneath the sill took place at 400-600°C and >5 kbar. $^{40}Ar/^{39}Ar$ dating of syn- and post deformation minerals constrains the activity of the shear zone to ~78-68 Ma (Davidson, 1991).

## PORPHYROBLASTS IN THE MGMB

Inclusion trails in minerals in the MGMB are a rich source of kinematic information. As the sill is approached, biotite, garnet, and amphibole appear; all may contain inclusion trails suitable for analysis (Figure 3.2). Biotite and garnet, both containing sigmoidal trails are sometimes found in the same thin section. This study examines six samples, three with biotite porphyroblasts, one with biotite and garnet, and two with amphibole (Figure 3.3). These samples were selected from oriented thin sections from 30 different outcrops in the rocks beneath the sill. Sections were cut perpendicular to the main foliation, and parallel to the down-dip lineation. This main foliation is interpreted as the shear plane, with a second foliation often developed at an angle to it, typically 45° or less. This is consistent with other kinematic indicators in the rocks (pyrite and rutile with fibrous overgrowths, rotated boudins, and pressure shadows around garnet), and with the data from boudinaged biotite, discussed below. The sections chosen have multiple ($\geq 5$) analyzable porphyroblasts per thin section. They are from a relatively small

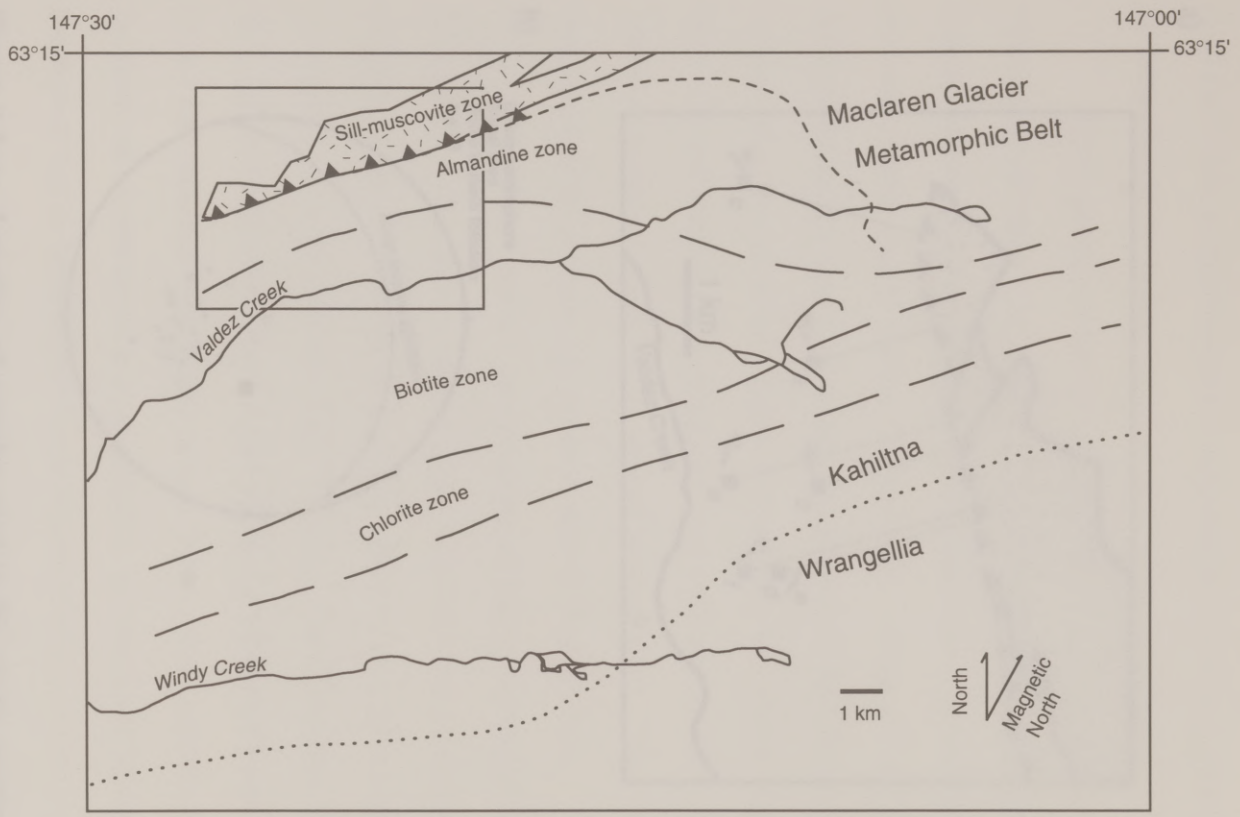


Figure 3.2: Metamorphic zonation map of Maclaren Glacier Metamorphic Belt, showing broad distribution of metamorphic minerals. Inset shows location of figure 3. Map modified after Smith (1981), Figures 46 and 47.

a)

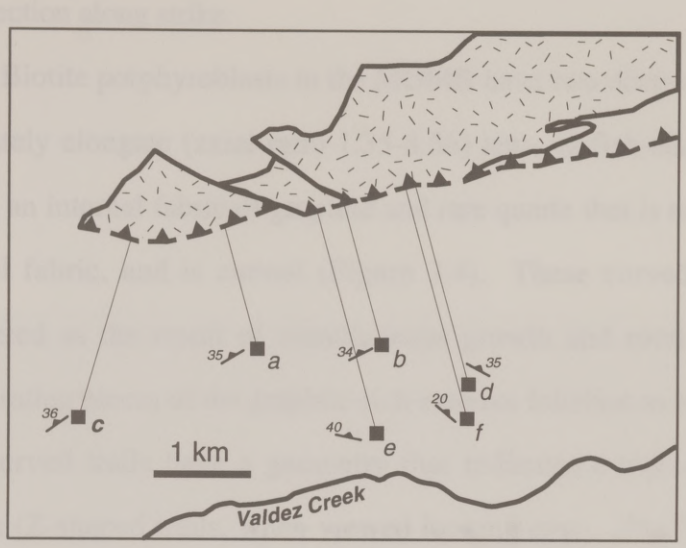


b)

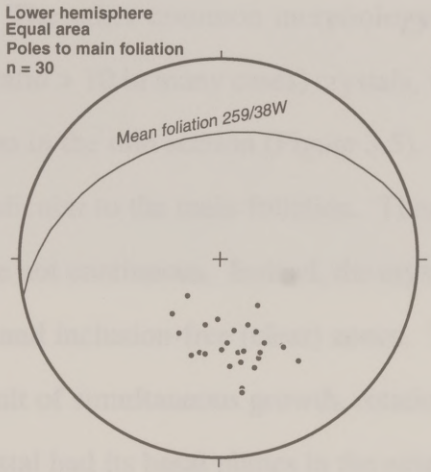


Figure 3.3: a: Location of samples used in this study relative to tonalite sill in MGMB. Distances from sill measured along lines marked. Modified after Smith (1981, Plate 1). b: Poles to main foliation in region.

(~10 $km^2$) area of approximately uniform dip, allowing a profile to be constructed by projection along strike.

Biotite porphyroblasts in the MGMB have two distinctive forms: equant to moderately elongate (axial ratio 1.35-8.56) lens- or fish-shaped crystals. These contain an internal fabric of graphite and rare quartz that is often discordant to the external fabric, and is curved (Figure 3.4). These curved inclusion trails are interpreted as the result of simultaneous growth and rotation, with the biotite incorporating pieces of the graphite-rich external foliation as it grew. In most cases these curved trails have a geometry that indicates a top-to-the-south sense of rotation (Z-shaped trails, when viewed looking east). The basal (001) planes of these crystals do not have any apparent preferred orientation.

The other common morphology of biotite porphyroblasts is as elongate (axial ratio > 10 in many cases) crystals, with long axes close to parallel to the main foliation in the thin section (Figure 3.5). Basal planes of these crystals are close to perpendicular to the main foliation. There are inclusion trails in these crystals, but they are not continuous. Instead, the crystal is made up of alternating inclusion-rich (dirty) and inclusion-free (clear) zones. These biotite crystals are interpreted to be the result of simultaneous growth, rotation and micro-boudinage. In this scenario, the crystal had its basal planes in the extension field at the start of deformation. In simple shear, this is the interval extending from the shear plane normal to shear plane parallel, in the synthetic direction (see Figure 3.6). As deformation progressed, the crystal pulled apart normal to the basal planes, growing clear zones between the dirty zones. Both the increase in axial ratio and the rotation towards the shear plane tend to decrease the rotation rate, favoring final orientations close to the

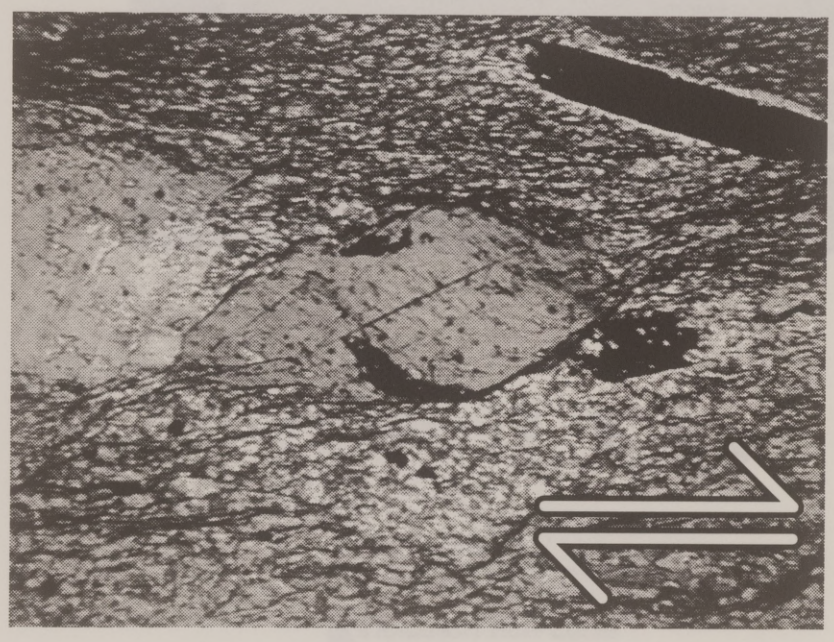

Figure 3.4: Biotite from sample E (location shown in figure 3.3) with curved inclusion trails defined by graphite, typical of those found in MGMB. Long axis of photo is 3 mm. North is to the left.

a)

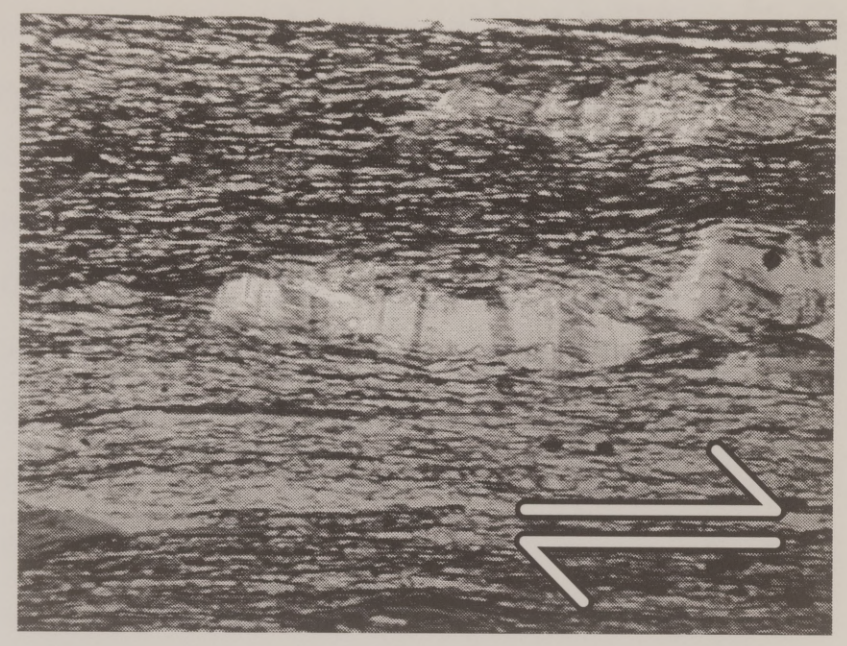

b)

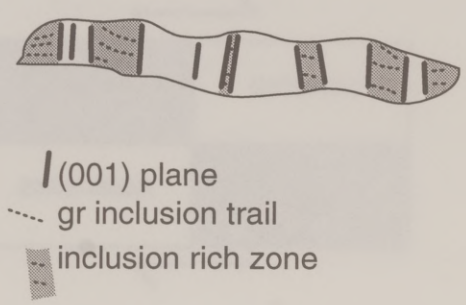


Figure 3.5: (a) Biotite from sample B (location shown in figure 3.3) pulled apart normal to basal cleavage. Long axis of photo is 3 mm. North is to the left. (b) Interpretive sketch of features in (a)

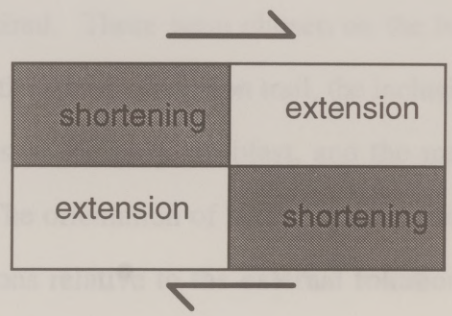


Figure 3.6: Fields of instantaneous shortening and extension in simple shear deformation.

shear plane. This mechanism is similar to that proposed for biotite porphyroblasts in the Pyrenees Mountains by Lister et al. (1986) and for chlorite-white mica porphyroblasts by Clark and Fisher (1995). Some biotite in the MGMB exhibits both curved inclusion trails and pull-apart zones.

Garnets in the MGMB are relatively equant (axial ratio 1.09-1.69) and have inclusion trails defined by both quartz and graphite, with quartz predominating (Figure 3.7). Amphibole porphyroblasts are extremely inclusion-rich, with quartz the most common inclusion (Figure 3.8). Axial ratios range from 2.47-5.56. Both garnets and amphiboles have curved inclusion trails

## TECHNIQUES

Digital or photographic images of 79 porphyroblasts from the six thin sections were acquired. These were chosen on the basis of clarity of inclusion trails. The trace of the central inclusion trail, the inclusion trails at the margins, the long and short axes of the porphyroblast, and the main external foliation were marked by hand. The orientation of biotite basal planes was also measured. The angle of the foliations relative to the external foliation (assumed to be the shear plane) and the length and angles of the porphyroblast axes were then measured on a electronic digitizing tablet connected to a personal computer.

A number of measures of rotation of porphyroblasts have been proposed (Busa and Gray, 1992, p. 582). The measure used here is the difference between the internal foliation at the center of the porphyroblast, (presumably the earliest included fabric) and the distant, undeflected external foliation. This is called the 'true rotation' by Busa and Gray, (1992). This quantity actually represents the total

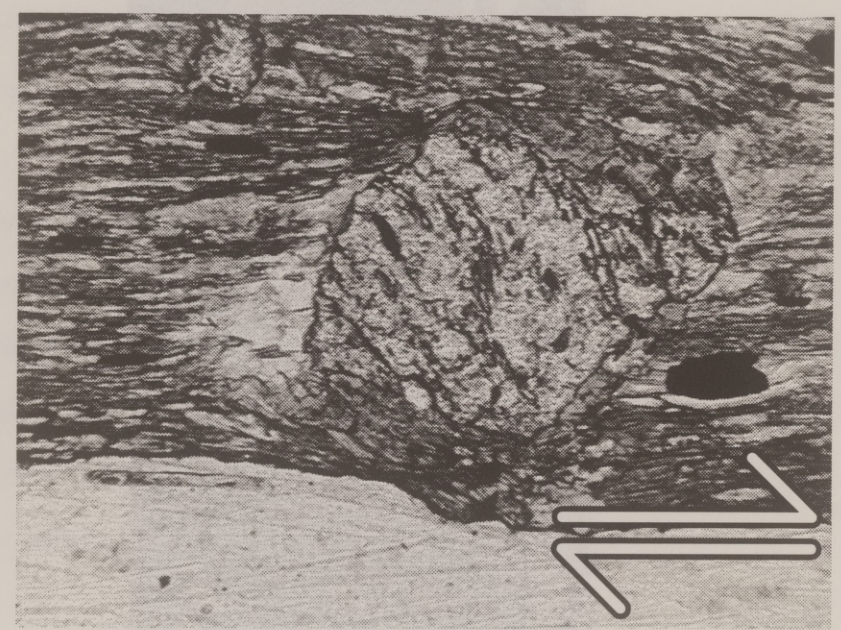

Figure 3.7: Garnet from sample B (location shown in figure 3.3) with curved inclusion trails of quartz and graphite. Long axis of photo is 3 mm. North is to the left.

Figure 3.8: Amphibole from sample A (location shown in figure 3.3) with curved inclusion trails, primarily of quartz. Long axis of photo is ~5 mm. North is to the left.

apparent relative rotation between the porphyroblast and foliation. Also measured here is the turn angle, the difference in orientation of the inclusion trail from the center to the edge of the porphyroblast. If the turn is less than 90° (as it is in all cases here) then the 'true rotation' equals the turn plus the deflection of the foliation in the matrix adjacent to the porphyroblast. These measures are summarized in Figure 3.9, an adaptation of Figure 6 from Busa and Gray (1992). In this study, the turn is used primarily as a check on the 'true rotation'.

In five of the six samples analyzed all but one of the measured rotations have the same sense as the top-to-the-south sense of regional shear. This allows some simplifications in the analysis of these sections. The absence of back rotation allows constraints to be put on the pure shear component of the deformation. As discussed in Chapter 2, the analysis of Ghosh and Ramberg (1976) shows that back rotation (antithetic to the sense of simple shear) will only occur when the conditions of equation 2.13, are met:

$$R > \frac{1 + \sqrt{1 + 4s_r^2}}{2s_r} \qquad (2.13)$$

Using the mean axial ratio of the population of porphyroblasts in each thin section not containing back rotation allows an upper limit to be placed on the ratio of pure to simple shearing, $s_r$. The calculated values are shown in Table 3.1, and range from 0.25 to 1.6. The value of 1.6, however, is from garnet that occurs in a sample also containing more elongate biotite porphyroblasts. Longer porphyroblasts are more sensitive to the effects of pure shear. The biotite in the garnet bearing section gives an upper limit of $s_r = 0.37$, so the true range is from 0.25 to 0.53.

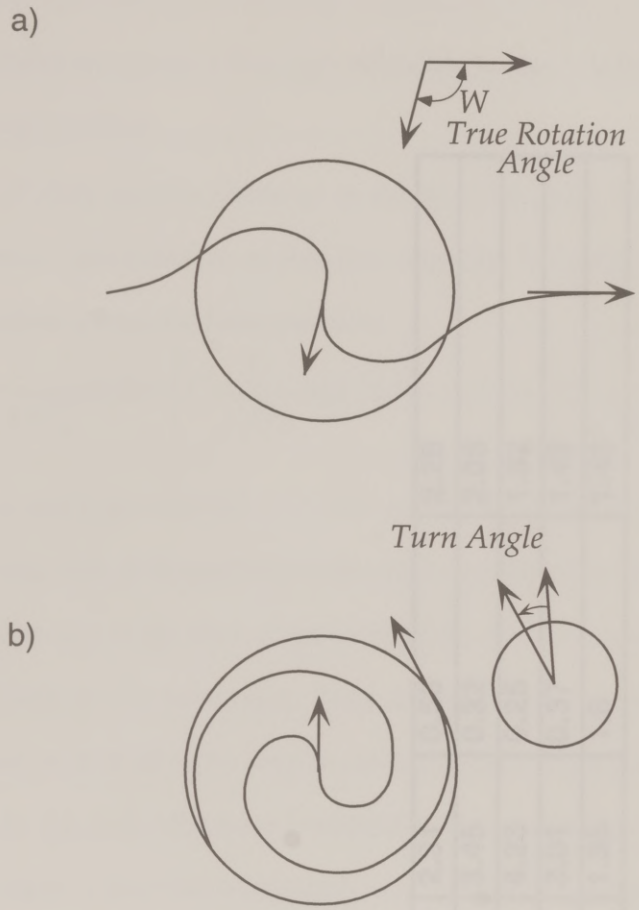


Figure 3.9: Measures of rotation, after Gray and Busa (1992, figure 6). The quantity measured here is the angular difference between the central inclusion trail and a distant, undeflected foliation. This is labeled the 'true rotation' by Gray and Busa (1992). It is, however, an apparent relative rotation of the porphyroblast and foliation.

| | | | |
|---|---|---|---|
| 31 (biotite) | 2.31 | 0.53 | 2.26 |
| 40 (biotite) | 3.45 | 0.32 | 2.03 |
| 29 (amphibole) | 4.23 | 0.25 | 1.82 |
| 32 (biotite) | 3.01 | 0.37 | 1.43 |
| 32 (garnet) | 1.35 | 1.6 | 1.43 |

Table 3.1: Mean axial ratios and critical $s_r$ (ratio of pure to simple shearing) for samples from which a mean finite simple shear strain was calculated. If $s_r$ exceeds the critical ratios, back rotations may occur.

Given that simple shear predominates, the porphyroblasts may be analyzed as if only simple shear was operating during the deformation. This reduces the unknown variables controlling the rotation history from two ($s_r$ and $\gamma$, finite simple shear strain) to one ($\gamma$), allowing a strain to be calculated from the measurements of each porphyroblast.

If only simple shearing is assumed ($s_r = 0$), then the term $B$ (eq. 2.11) becomes 0. Substitution of this into equation 2.9 yields a new equation relating simple shear strain and finite rotation:

$$\gamma = \frac{1}{\sqrt{AC}}\left(\arctan\left[C\frac{1}{\sqrt{AC}}\tan\{\phi\}\right] - \arctan\left[C\frac{1}{\sqrt{AC}}\tan\{\phi_0\}\right]\right) \qquad (3.1)$$

where $A$ and $C$ are defined in (2.10) and (2.12), respectively. The final orientation of the long axis of the porphyroblast ($\phi$) is measured in the thin section. The initial orientation ($\phi_0$) is the final orientation minus the measured rotation angle. $A$ and $C$ depend only on the axial ratio. Thus an independent strain estimate (that accounts for variation in axial ratio) may be calculated from each porphyroblast.

In the case where no assumption may be made about the ratio of pure to simple shear, a less direct approach must be taken. A graph of the final orientation of the porphyroblasts versus the observed rotations is fit with a curve predicting these values for a porphyroblast with the mean axial ratio of the population. The best fit yields an estimate of $\gamma$, repeated fits for different assumed $s_r$ yield a combined estimate of $\gamma$ and $s_r$ for a sample.

## RESULTS

Porphyroblast measurements produce a coherent strain profile, but only if care is taken to separate various effects on the porphyroblasts analyzed. If all biotites are included, no pattern to the strains determined emerges (Figure 3.10). The results are dramatically different if the orientation history of the biotite basal cleavage planes is considered. As noted previously, biotites that start with the normals to their basal planes in the extension field pull apart along those planes of weakness. This effect occurs even in those crystals that are only in the extension field for a short period of time. These often have visible clear pull-apart zones, in addition to curved inclusion trails (Figure 3.11). Because the calculated shear strain depends strongly on axial ratio (R), an error in estimating R, or a change in R during deformation is likely to cause errors in the strain determination. This can be avoided by only using those porphyroblasts whose basal planes have remained in the shortening field throughout the deformation. These can be identified by taking the final orientation of the basal planes and subtracting the rotation determined from inclusion trails. Those crystals that have been stretched can then be discarded. When strains are calculated on this basis, a pattern of increasing strain towards the sill is clear (Figure 3.12).

The variation in the strain determined from biotite falls within the 95% confidence intervals calculated. falls within the 95% confidence intervals for the mean of each sample (plotted as error bars in Figure 3.12). The confidence intervals are calculated assuming an underlying normal distribution, and are corrected for small numbers of observation (using Student's t rather than Z

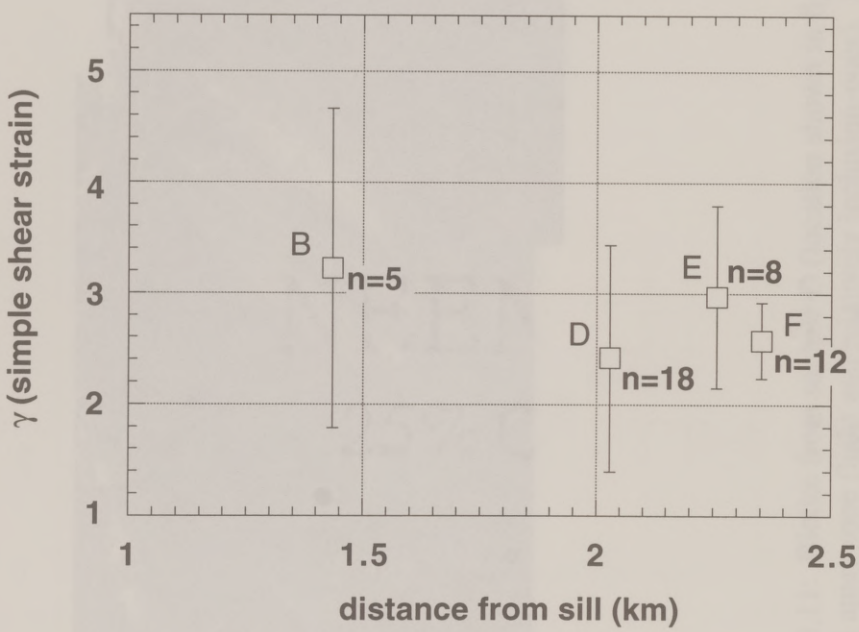


Figure 3.10: Mean simple shear strain in four samples, determined from all biotites in the samples. Error bars are 95% confidence interval for the mean.

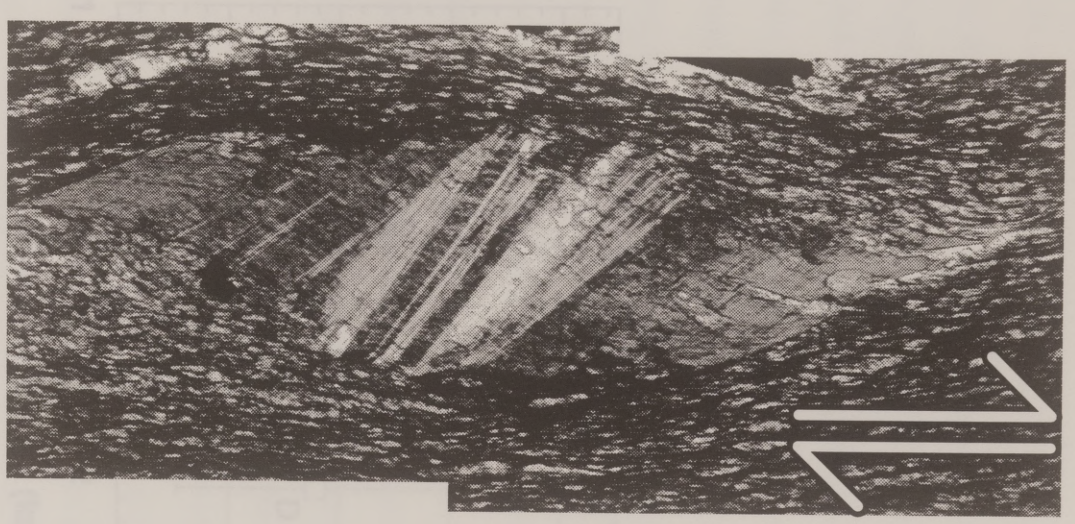

Figure 3.11: Biotite from sample D (location shown in figure 3.3) with curved inclusion trails and pull apart zone (light and relatively inclusion-poor). Pull apart zones are parallel to biotite basal planes, which started in extension field, but have rotated into shortening field. Long axis of photo is ~5.5 mm. North is to the left.

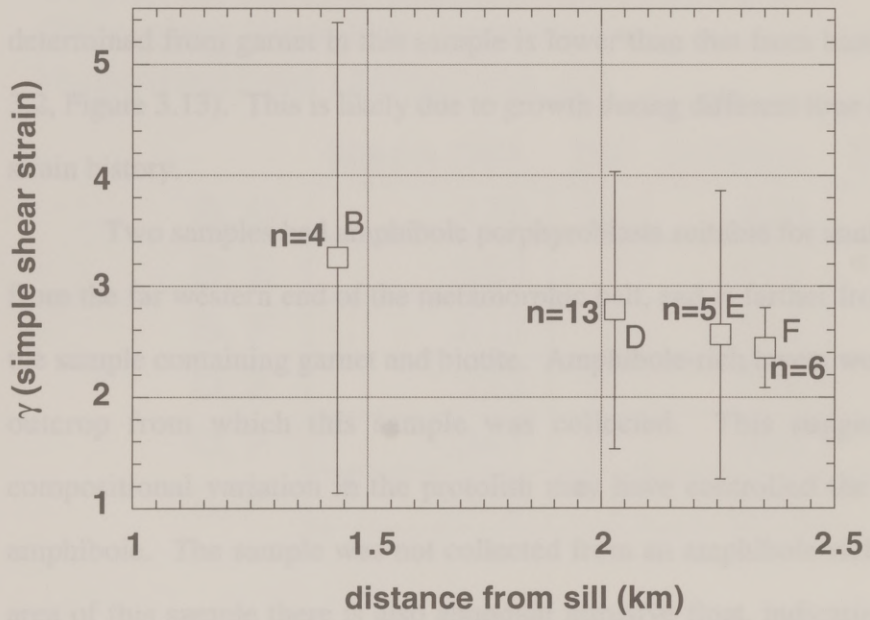


Figure 3.12: Mean strain in four samples, determined from biotites with basal plane normals that remained in the shortening field throughout their rotation history. Error bars are 95% confidence interval for mean.

distribution). In order to asses the reality of the apparent increase of mean strains, an unpaired t-test is calculated for each combination of samples. Results (shown in Table 3.2) show that the most widely separated samples (B and F) have a difference in the recorded strain, at about 80% confidence. The less widely separated pairs do not have a significant difference in their means. Non-parametric tests (which do not assume an underlying normal distribution) give the same conclusion. More widely separated samples, and more measurements from each sample could help strengthen evidence for a strain gradient.

One sample has both garnet and biotite porphyroblasts. The strain determined from garnet in this sample is lower than that from biotite ($\gamma = 2.2$ vs. 3.2, Figure 3.13). This is likely due to growth during different time intervals of the strain history.

Two samples had amphibole porphyroblasts suitable for analysis. One was from the far western end of the metamorphic belt, and is farther from the sill than the sample containing garnet and biotite. Amphibole-rich layers were noted in the outcrop from which this sample was collected. This suggests that some compositional variation in the protolith may have controlled the abundance of amphibole. The sample was not collected from an amphibole-rich layer. In the area of this sample there is also abundant intrusive float, indicating the possible presence of a minor sill or dike. All amphibole porphyroblasts exhibit forward rotation, and the mean strain is $\gamma = 2.8$ (Figure 3.13).

The second amphibole-bearing sample is the closest sample to the sill (1.26 km) and the most geometrically complex. Both forward and backward rotations are exhibited, in approximately equal numbers. This indicates that there was a

**Unpaired Means Comparison for strain**
**Grouping Variable: sample #s**
**Hypothesized Difference = 0**

| | Mean Diff. | DF | t-Value | P-Value |
|---|---|---|---|---|
| B, D | .470 | 15 | .423 | .6784 |
| B, E | .693 | 7 | .876 | .4099 |
| B, F | .812 | 8 | 1.464 | .1813 |
| D, E | .223 | 16 | .226 | .8238 |
| D, F | .341 | 17 | .395 | .6976 |
| E, F | .119 | 9 | .264 | .7980 |

Table 3.2: Comparison of mean strain determined from biotite porphyroblasts in different samples. The most widely separated samples (B, F) show a significant difference in their means (indicated by the low p value).

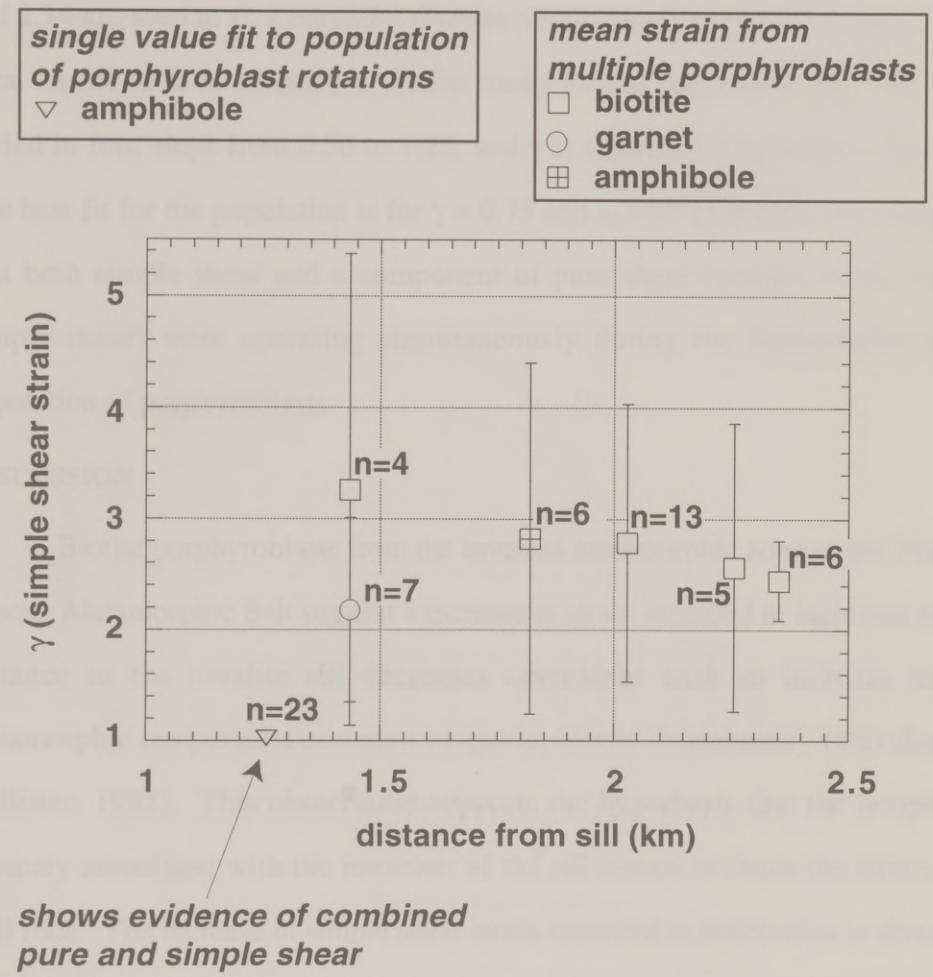


Figure 3.13: Strain in all six samples. Values are mean of multiple porphyroblasts in sample, except for amphibole plotted as triangle, which also shows evidence of combined pure and simple shear. Fit is shown in Figure 3.14. Error bars are 95% confidence interval for mean.

substantial component of pure shear in this deformation, and the analysis used for the other samples is not valid. Data from all 23 porphyroblasts measured in this sample can be combined for a more thorough analysis. In this case equations 2.9 and 2.14 are used to fit a curve for rotation versus final orientation to the observed data. Axial ratio is assumed to be the mean for the population (R = 4.23), $s_r$ is varied in four steps from 0.50 to 1.25, and $\gamma$ is determined by a least squares fit. The best fit for the population is for $\gamma = 0.75$ and $s_r = 1.0$ (Figure 3.14), indicating that both simple shear and a component of pure shear (normal to the plane of simple shear) were operating simultaneously during the deformation of this population of porphyroblasts.

**DISCUSSION**

Biotite porphyroblasts from the inverted metamorphic zone of the Maclaren Glacier Metamorphic Belt suggest a increase in strain recorded in inclusion trails as distance to the tonalite sill decreases coincident with an increase in peak metamorphic temperature recorded by garnet-biotite thermometry (Davidson and Hollister, 1992). This observation supports the hypothesis that the temperature anomaly associated with the intrusion of the sill served to focus the strain in the wall rock. The increase in simple shear strain recorded in the biotites is about 33% over a 900 meter map distance. This corresponds to a structural thickness of 550 m, for the mean dip of 38°. Given the experimentally determined exponential dependence of rock strength on temperature, a larger increase might be expected. Peak temperatures, however, are short-lived, and it is the integrated strain during porphyroblast growth that is recorded here. The garnets measured record lower

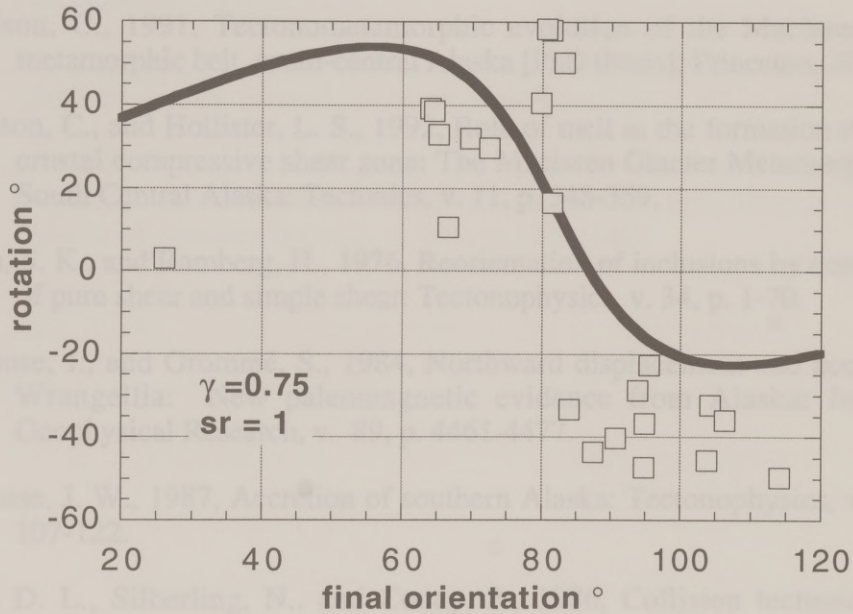


Figure 3.14: Least squares best fit of theoretical rotation vs. final orientation curve to population of amphibole porphyroblasts from sample A. Best fit is for $\gamma = 0.75$, $s_r = 1$.

## REFERENCES


Busa, M. D., and Gray, N. H., 1992, Rotated staurolite porphyroblasts in the Littleton Schist at Bolton, Connecticut, USA: Journal of Metamorphic Geology, v. 10, p. 627-636.

Clark, M. B., and Fisher, D. M., 1995, Strain partitioning and crack-seal growth of chlorite-muscovite aggregates during progressive noncoaxial strain: an example from the slate belt of Taiwan: Journal of Structural Geology, v. 17, p. 461-474.

Davidson, C., 1991, Tectonometamorphic evolution of the Maclaren glacier metamorphic belt, south-central Alaska [PhD thesis]: Princeton, 201 pp.

Davidson, C., and Hollister, L. S., 1992, Role of melt in the formation of a deep-crustal compressive shear zone: The Maclaren Glacier Metamorphic Belt, South Central Alaska: Tectonics, v. 11, p. 348-359.

Ghosh, S. K., and Ramberg, H., 1976, Reorientation of inclusions by combination of pure shear and simple shear: Tectonophysics, v. 34, p. 1-70.

Hillhouse, J., and Grommé, S., 1984, Northward displacement and accretion of Wrangellia: New paleomagnetic evidence from Alaska: Journal of Geophysical Research, v. 89, p. 4461-4477.

Hillhouse, J. W., 1987, Accretion of southern Alaska: Tectonophysics, v. 139, p. 107-122.

Jones, D. L., Silberling, N., and Coney, P., 1986, Collision tectonics in the Cordillera of western N. America: examples from Alaska, *in* Coward, M., and Ries, A., eds., Collision Tectonics, Special Publication, Geological Society, p. 367-387.

Jones, D. L., Silberling, N. J., and Hillhouse, J., 1977, Wrangellia - A displaced terrane in northwestern North America: Canadian Journal of Earth Sciences, v. 14, p. 2565-2577.

Lister, G. S., Boland, J. N., and Zwart, H. J., 1986, Step-wise growth of biotite porphyroblasts in pelitic schists of the western Lys-Caillaouas massif (Pyrenees): Journal of Structural Geology, v. 8, p. 543-562.

Nokleberg, W. J., Jones, D. L., and Silberling, N. J., 1985, Origin and tectonic evolution of the Maclaren and Wrangellia terranes, eastern Alaska Range, Alaska: Geological Society of America Bulletin, v. 96, p. 1251–1270.

Silberling, N. J., Jones, D. L., Blake, M. C., and Howe, D. G., 1987, Lithotectonic terrane map of the western conterminous United States: U. S. Geological Survey Map 1874-C.

Silberling, N. J., Richter, D. H., and Jones, D. L., 1981, Recognition of the Wrangellia terrane in Clearwater Mountains and vicinity, southcentral Alaska: U. S. Geological Survey Circular, v. 823-B, p. 51-54.

Smith, T. E., 1981, Geology of the Clearwater Mountains, South-central Alaska, Geologic Reports: Anchorage, Alaska Division of Geological and Geophysical Surveys, 72 p.

Stone, D., Panuska, B., and Packer, D., 1982, Paleolatitudes versus time for southern Alaska: Journal of Geophysical Research, v. 87, p. 3697-3707.

Wallace, W. K., Hanks, C. L., Rogers, J. F., 1989, The southern Kahiltna terrane: Implications for the tectonic evolution of southwestern Alaska: Geological Society of America Bulletin, v. 101, p. 1389–1407.

# Chapter 4: Thermally focused deformation: A major tectonic process


## ABSTRACT

Zones of concentrated strain are widespread in deformed rocks and are commonly associated with igneous intrusions. To demonstrate the effect of a syntectonic temperature anomaly on deforming rocks, coupled temperature-displacement finite element models have been constructed to simulate a cooling pluton in a zone of simple shear, using a realistic power law rheology.

Thermal anomalies should focus strain because hotter material is weaker than colder material of the same composition. A model was constructed to simulate the emplacement of a 1.0 x 1.8 km rectangular pluton in the middle or lower crust. Node spacing is 200 m near the pluton. The nodes that make up the pluton were assigned an initial temperature of 900°C. The remaining nodes were set at 400°C, an approximation of mid-crustal conditions. Because there is no deformation at the start of the model, this could be considered 'passive' emplacement. All parts of the model obey the same power law creep relationship, and strength contrasts are entirely due to temperature variations. The pluton is allowed to cool for $1x10^5$ yr, bringing most of it below 700°C. As the pluton continues to cool by conduction, the model is subjected to simple shear, with a bulk finite strain rate of $1x10^{-14}$ $s^{-1}$. The base of the model is fixed; the other boundaries can move in the x-direction. All other nodes are unconstrained. Total bulk shear strain ($\gamma$) is 0.318.

This model predicts that a thermal anomaly associated with a cooling pluton concentrates deformation not just in the pluton, but into a laterally extensive zone that also transects the wall rocks. Values of $\gamma$ in this zone are as much as 69% higher than in the least strained parts of the modeled space.

Model results are compared with results of microstructural strain analysis in the Maclaren Glacier Metamorphic Belt (MGMB) of south-central Alaska, where a synkinematic tonalite sill intruded pelites during top-to-the-south shearing. Analysis of inclusion trails in biotite, amphibole and garnet shows that finite strain increases with decreasing distance from the pluton, supporting the hypothesis that the thermal anomaly associated with the pluton was key in nucleating the shear zone.

## INTRODUCTION

It is has long been recognized from field studies that rock rheologies are strongly temperature dependent. Since the 1960s, experimentalists have worked to calibrate the constitutive equations, referred to as rock flow laws, for a variety of rock types (Tullis, 1979; Singh, 1981; Kirby and McCormick, 1989). Experimentally derived flow laws, along with observations from field work and earthquake seismology, provide the basis for understanding the rheology of the lithosphere. Relatively little has been done, however, to apply the calibrated flow laws to geologic processes whose manifestations are observable at the map and outcrop scales. The particular problem addressed here is the interplay between plutonism and shear zone evolution. The new approach applied here is finite element modeling that directly couples heat flow and strain evolution. The general theoretical results are compared to structural and petrographical observations from the Maclaren Glacier Metamorphic Belt (MGMB) in southeast Alaska, and to published studies of two other areas where the heat input from magmatism may have influenced deformation.

## PREVIOUS WORK: THERMAL EFFECTS IN SHEAR ZONES

Most quantitative models of shear zone evolution that have assessed thermal effects have been developed with strain heating as an implicit assumption. In the early days of plate tectonics, it was assumed that strain heating of the top of the descending plate at subduction zones was the source of heat that generated arc magmas by melting subducted ocean crust (Oxburgh and Turcotte, 1970; Turcotte

and Schubert, 1973). It remains uncertain how much heat will be generated by deformation at displacement rates of cm/yr, and whether this will have significant geological effects. In contrast, it is apparent from studies of material properties that a temperature anomaly of the magnitude associated with an igneous intrusion can have a large effect on the nature of deformation near the anomaly.

Representative of previous work linking heat and deformation is the model Nicolas et al. (1977) use to explain metamorphism along the Angers–Lanvaux, Montagne Noire, and Maydan shear zones. These authors see this as an effect of strain (viscous) heating, and hypothesize that this heating was also responsible for localization of strain. Theirs was a purely a one-dimensional heat conduction model, with a constant strain rate and constant shear zone width. The authors hypothesized that strain heating is sufficient to cause melting at depth.

Similar in approach is the model of Poirier et al. (1979), who developed a one-dimensional shear zone model that assumed constant width and strain rate. Their model incorporated an experimentally determined creep law. From the calculated stresses, the amount of strain heating was calculated using the relationship $dT = \frac{\sigma}{\rho C_p} d\gamma$, where $\sigma$ is stress, $\rho$ is density, Cp is heat capacity, and $\gamma$ is shear strain. Results differ from Nicolas et al. (1977) in that Poirier et al. (1979) concluded that some initial weakness is required to concentrate deformation into a zone, and that although strain heating acts to focus strain into a shear zone, not enough heat is generated to cause melting. Poirier et al. (1979, p. 452) state that "An external source of heat might cause …activation of the shear zone."

Brun and Cobbold (1980) and Fleitout and Froideveaux (1980) both evaluated the effect of strain heating on the evolution of shear zones using realistic rheologies. While these models predict variations in strain and temperature, Brun and Cobbold (1980, p. 158) state that evidence for strain heating is "...scanty and controversial."

In contrast, the qualitative importance of localized thermal weakening associated with plutonism is increasingly being recognized as profoundly significant in a variety of geologic settings. Hutton (1982) showed that synchronous deformation and magmatism in the Donegal (Ireland) complex was responsible for both creation of space for the granite and determining the final configuration of the shear zone into which it was emplaced. Hollister and Crawford (1986) concluded that melt–bearing shear zones in the Coast Ranges of British Columbia were responsible for concentrating strain into narrow zones and enabling rapid (> 1 mm/yr) vertical movements. Karlstrom (1989, p. 763) postulates that granitoid magmatism and regional deformation are so closely linked that "All granitoids are syntectonic in the broad sense that they are emplaced into crust that is experiencing regional deformation."

Strain around a syntectonic pluton undergoing non–coaxial deformation was evaluated by Brun and Pons (1981) using a purely kinematic model. They assumed that a pluton was simultaneously ballooning and undergoing simple shear. By adding the displacements due to each process, they predicted patterns of strain and cleavage. Similar kinematic models have been developed for three dimensions by Guglielmo (1993). The way in which the ambient temperature and stress fields control the development of strain distributions is not addressed by these purely

kinematic models, however, and the rheological behavior of rocks is not considered.

Emplacement mechanisms of plutons are a topic of current controversy. Many studies attempt to infer the kinematics of emplacement and neglect the thermal effects on rock strength and post-emplacement strain history. A variety of mechanisms have been proposed for pluton emplacement, summarized in Paterson et al. (1991b). Distinguishing between hypotheses is difficult, because it requires separation of strain due to emplacement from that due to later deformation. Nonetheless, Paterson et al. (1991a) used a variety of meso- and micro-structural analyses to propose that intense strain around the Papoose Flat pluton is due to post-emplacement deformation.

The heat flow equations for the conductive cooling of plutons of various geometries were presented by Carslaw and Jaeger (1959) and Jaeger (1961; 1964). Analytical solutions such as these provide important constraints on the thermal effects of plutons, but have considerable limitations as to geometry. Numerical models can address not only more complex geometries, but also non-static problems. Barton and Hansen (1989), and Hansen and Barton (1989) used two-dimensional numerical models that included geothermal gradients to evaluate the effect of magmatic advection of heat on regional thermal budgets. As part of their study they showed that a single large (~17x12 km) two-dimensional pluton crystallized in times of the order $10^5$ yr, but took on the order $10^6$ yr to cool to background temperatures. Bowers et al. (1990) showed the importance of geometry in a study that modeled the Cupsuptic pluton of Maine, USA. They showed that metamorphic patterns near the pluton were strongly controlled by the

two-dimensional shape of the intrusion. Previous work with a modeling approach closest in principle (but not in technique) to the one employed here is Gettings (1988), in which an attempt is made to quantitatively evaluate the evolution of wall rock strength around a cooling pluton. For a 20 x 20 x 5 km pluton, he found that the flow strength of mid-crustal wall rocks was reduced by as much as 50% because of the thermal perturbation. Gettings' (1988) calculations involve a static thermal/strength model and strains were not calculated.

The goal of this study is to quantify the effect on strain distribution of introducing a large thermal anomaly into rocks modeled with a realistic temperature-dependent rheology. This work may aid in the study of emplacement mechanisms by determining the distribution of post-crystallization, thermally controlled, strain during the syntectonic cooling of plutons to ambient conditions.

## ROCK STRENGTH AND THE NECESSITY FOR COUPLED TWO-DIMENSIONAL THERMAL–MECHANICAL MODELING

Coupled thermal-mechanical models of pluton-related deformation requires a variety of input data, the most important of which specify the mechanical behavior of rocks.

Deformation of rocks in the laboratory demonstrates the strong dependence of strength upon temperature and an order of magnitude contrast in rock strength between different lithologies. Vernon and Flood (1988), for example, concluded that even subtle lithologic contrasts, such as small variations in quartz and biotite content, can cause marked contrasts in the response of granites to deformation.

Thus, lithological controls (e.g. granite versus metamorphosed sediment) on strain distribution should generally be very significant.

The effect of local temperature variations on regional deformation is evident from the work of Fletcher and Karlstrom (1990). They show that Precambrian shear zones in basement terranes of the eastern Mojave desert are narrow and tend to follow the contact between granitic plutons and surrounding supracrustal gneisses but widen and become diffuse away from plutons.

Recent deformation experiments to determine flow laws (Wilks and Carter, 1990; Shea and Kronenberg, 1992) confirm that such effects should be typical and that a "cross-over" in rock strength may even occur. For instance, the flow strength (at $10^{-14}$ $s^{-1}$) of a biotite schist may be twice that of a quartz-feldspar granulite at <400°C (upper to mid crustal conditions), but ten times weaker at 600°C (lower crustal conditions). This is indicative of important controlling factors in metamorphism and deformation: the contrasting rheologies of different lithologies and the change in behavior with temperature. Obviously, such an argument involves extrapolation outside of the range of conditions in laboratory experiments, but the range and accuracy of laboratory measurements is rapidly improving (Gleason and Tullis, 1993; Mares and Kronenborg, 1993; Kohlstedt et al., 1995).

The conceptual model for the relationship of plutonism and deformation in this investigation is as follows. Upon intrusion, a magma body will have very low strength and will play a major role in localizing deformation, as Hollister and Crawford (1986) and Hollister (1993) concluded. As the pluton cools and crystallizes, it transfers heat to the surrounding rocks, which become thermally weakened. Quantification of this weakening is the focus of this study. Two end-

member situations appear likely in the middle to upper crust. If the pluton intrudes into host rocks with a temperature-dependent rheology that is similar to or stronger than itself for given P-T-strain rate conditions, the pluton will remain the weakest area throughout its cooling history. Alternatively, if the country rock is weaker (a micaceous schist, for example), the pluton can eventually become stronger than the surrounding rocks. In either case, the thermal effect of the intrusion is to strongly focus deformation, either within the pluton, or around its margins. Only by simultaneously considering temperature and displacement fields can this effect be understood.

## TECHNIQUES

The method of finite elements is a well established means of solving continuum equations (Zienkiewicz, 1989; Zienkiewicz and Taylor, 1991), that has found a variety of applications in the geological sciences (De Bremaecker and Becker, 1978; Lan and Hudleston, 1991).

In a continuum, force equilibrium must exist over any arbitrary volume. In the finite element method, a less rigorous requirement of average equilibrium over a discrete volume is imposed. The area of interest is then divided into nodes and elements, so that displacements are a function of nodal displacements, and volumes are the sums of the volumes of individual elements. With the introduction of the strain-displacement matrix and a constitutive law, a series of algebraic equations result.

This study uses the commercial software ABAQUS, a flexible, modular, non-linear, Lagrangian finite element program, which has special routines to solve

coupled heat transfer-stress analysis equations. This coupling is crucial, for this study concerns the behavior of rock as a thermal anomaly decays. A simultaneous solution for temperature and displacement will offer insight not available by other means.

A series of coupled temperature-displacement finite element models of a cooling pluton in a zone of simple shear are constructed to demonstrate the effect of a temperature anomaly on deforming rocks. Rheological parameters are taken from Wilks and Carter (1990) for Adirondack granulite, which consists of 45% potassium feldspar, 21% quartz, 20% clinopyroxene, 5% plagioclase, 4% oxides, and 1% horneblende, garnet and orthopyroxene. In a series of experiments ranging from 575 to 900°C, 0.86 to 1.01 GPa confining pressure, and $10^{-4}$ to $10^{-7}$ $s^{-1}$ strain rate, they found that the behavior of this rock was best described by a power law creep relation of the form $\dot{\varepsilon} = A\sigma^n e^{-Q/RT}$ with A = $8x10^{-3}$ $MPa^{-n}$ $s^{-1}$, Q = 243kJ/mol, and n = 3.1. Quartz dominates the rheological behavior of this rock. In the models below this is approximated by a relationship $\dot{\varepsilon} = A\sigma^n$, with the $e^{-Q/RT}$ term accounted for by appropriately varying A with temperature. The variation of flow stress with temperature is shown in Figure 4.1. While this flow law is particular to the Adirondack granulite, it has the same form as many other experimentally determined flow laws. The general results of this study should be applicable to any place where a thermally activated deformation process is operative.

To verify that these models reproduce the published rheology measured by Wilks and Carter (1990), tests were performed on single elements and groups of elements. In addition, numerical models that recreated the geometry and

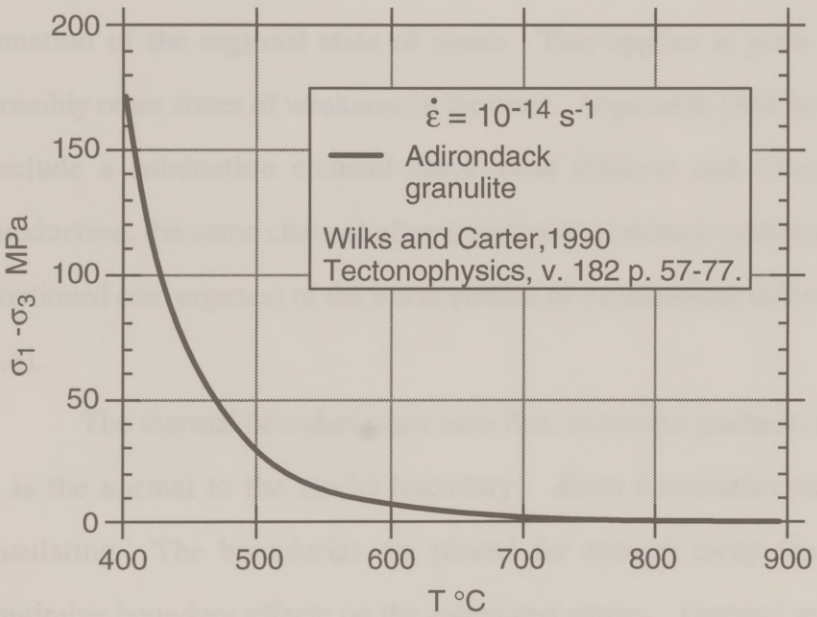


Figure 4.1: Variation of flow stress with temperature for a strain rate of $10^{-14}s^{-1}$. Data from Wilks and Carter (1990).

measurement conditions reported by Wilks and Carter (1990) were performed (see Figure 4.2). These tests showed the finite element model is a reasonable representation of the published flow law over a wide range of conditions.

Mechanical boundary conditions were selected to model a regional simple shear deformation. The upper and lower edges of the model domain have specified displacements. The upper edge moves a specified distance in x in a specified time; the lower boundary does not move. The left and right edges are free to move in x only. This configuration is illustrated in Figure 4.3. These boundary conditions are appropriate for any place where displacement is externally controlled, rather than a function of the regional state of stress. This applies at plate boundaries, and possibly other zones of weakness in the crust. Applicable plate boundary situations include a subduction channel shear zone (Shreve and Cloos, 1986) during subduction, the same channel after a continent-continent collision (but with some continued convergence) or the lower portion of a continental strike-slip fault (Figure 4.4).

The thermal boundaries are zero flux, (constant gradient, $dT/dn = 0$, where n is the normal to the model boundary). Such boundaries can be considered insulating. The boundaries are placed far enough away from the pluton to minimize boundary effects on the calculated strains. Thermal material properties are given in Table 4.1, and are appropriate for intermediate to silicic intrusions at mid- to upper-crustal levels.

The finite element mesh was chosen to balance spatial and temporal resolution and computational costs. Elements are smaller in the region of interest.

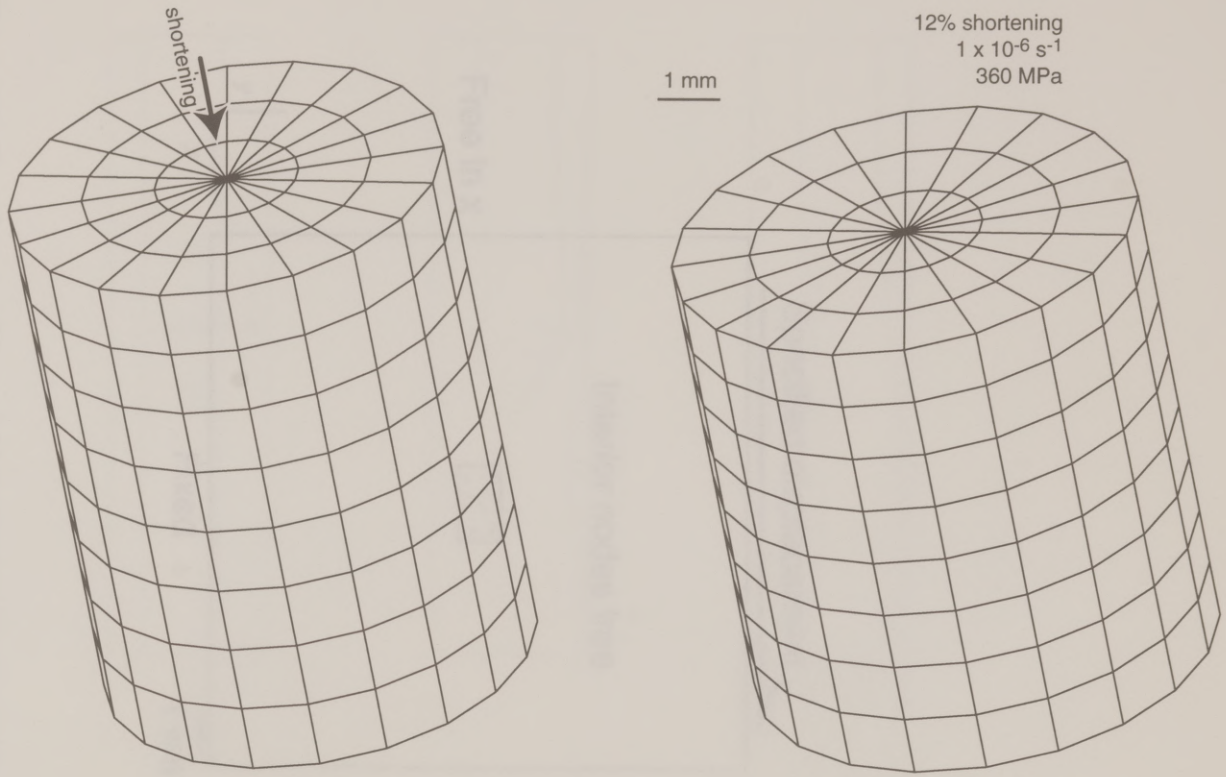


Figure 4.2: One of the tests used to verify the finite elemnt techniques used in this study. These numerical models recreated the geometry and measurement conditions reported by Wilks and Carter (1990). These tests show a reasonable numerical approximation to the published flow law over a wide range of conditions.

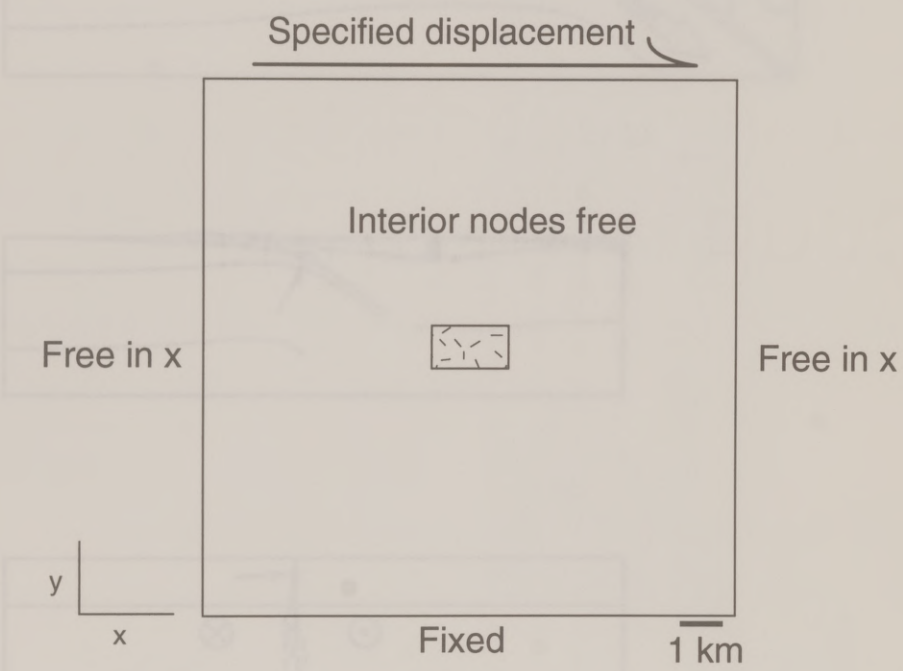


Figure 4.3: Boundary conditions, which simulate passive emplacement into a regional simple shear deformation.

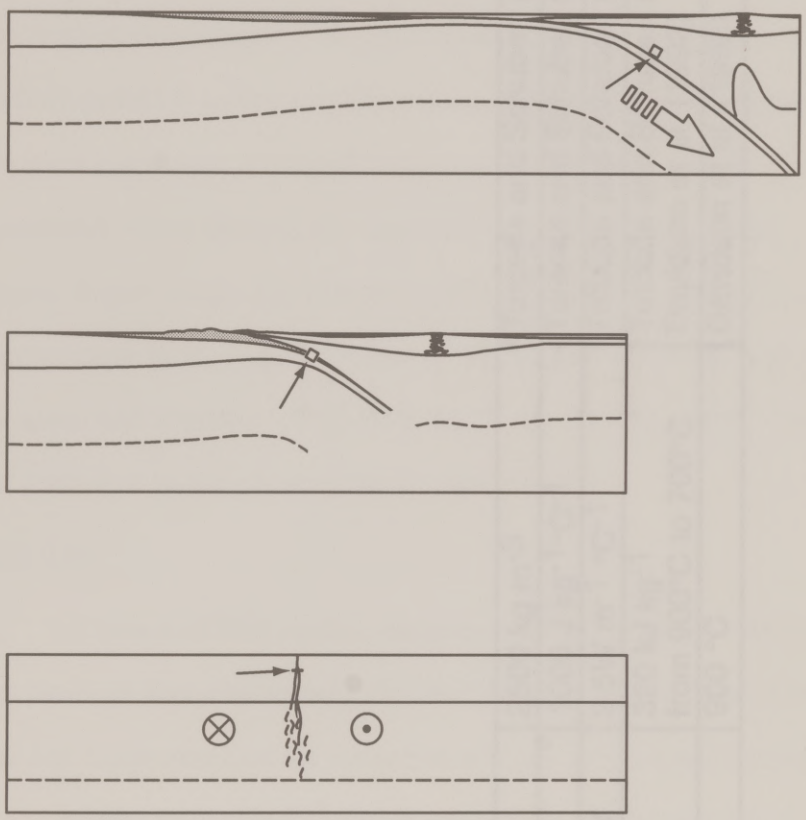

Figure 4.4: Possible tectonic settings for the model shear zone: subduction channel shear zone during subduction, a shear zone after a continent-continent collision (but with some continued convergence) or lower portion of a continental strike slip fault.

| | | |
|---|---|---|
| Density | 2500 kg $m^{-3}$ | Turcotte and Schubert (1982) |
| Heat Capacity | 1000 J $kg^{-1}°C^{-1}$ | Turcotte and Schubert (1982) |
| Thermal conductivity | 2.5W $m^{-1}$ $°C^{-1}$ | Turcotte and Schubert (1982) |
| Latent heat (of pluton) | 320 kJ $kg^{-1}$ from 900°C to 700°C | Turcotte and Schubert (1982) Davidson et al. (1992) |
| Emplacement T | 900 °C | Davidson et al. (1992) |

Table 4.1: Thermal material properties.

The mesh is shown in Figure 4.5, where the elements representing the pluton are shaded.

The initial temperature conditions are a uniform temperature field throughout the country rock (400 °C in most models) and an intrusion temperature of 900 °C. The intrusion is allowed to cool for 10 ky before deformation begins. The temperature pattern at the start of deformation is shown in Figure 4.6. There are both practical and conceptual reasons for this initial pre-deformational cooling. The practical reason is the difficulty in achieving convergence of the finite element algorithms when there is an extremely high strength contrast. The conceptual reason is that when the pluton is still partially molten, strain is likely to be concentrated in the liquid portion of the system (Hollister and Crawford, 1986; Davidson and Hollister, 1992; Hollister, 1993; Davidson et al., 1994). It is the late- and post-melt-bearing history that is considered here.

## RESULTS

A series of five models are presented to show the influence of magmatic heat input on near-pluton deformation and the general influence of rheology, strain rate, and temperature on the formation of shear zones near intrusions.

Model 1 (Figure 4.7) shows most of the important basic features of thermal focusing of strain. A 1.0 x 1.8 km rectangular pluton is placed in the center of a 12.6 x 12.6 km shear zone. Because there is no deformation at the start of the model, this simulates 'passive' emplacement. The nodes which make up the sill were assigned an initial temperature of 900°C, the remaining nodes were set to 400°C. All parts of the model obey the power law creep relationship, and strength

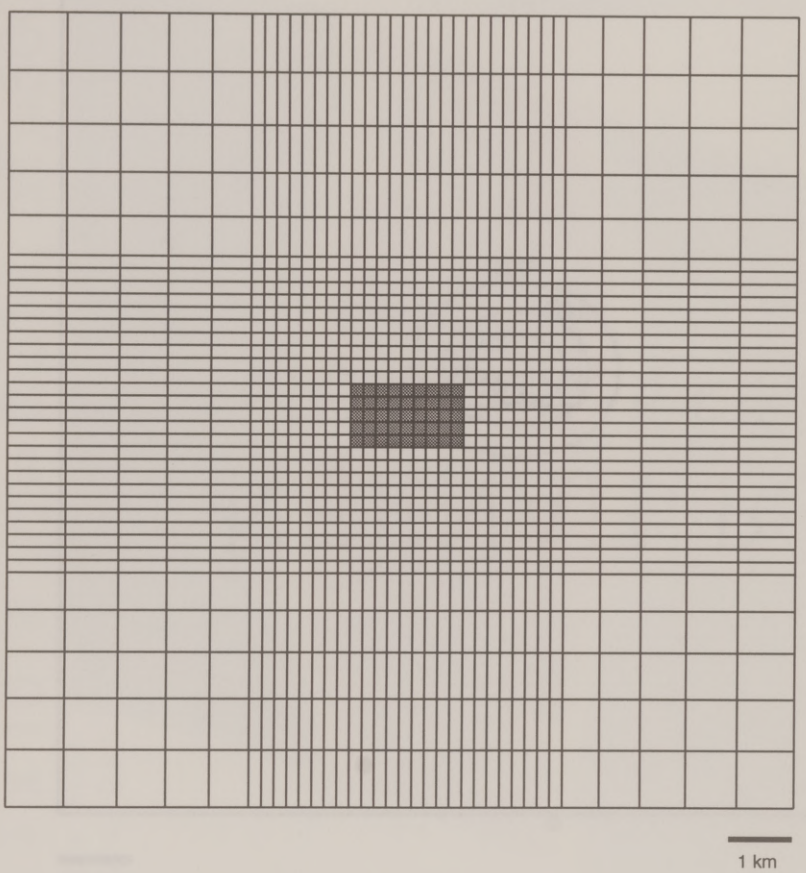


Figure 4.5: The finite element mesh used in these models. This was chosen to balance fineness of discretization and computational costs. Elements are smaller in the region of interest. Elements representing the pluton are shaded.

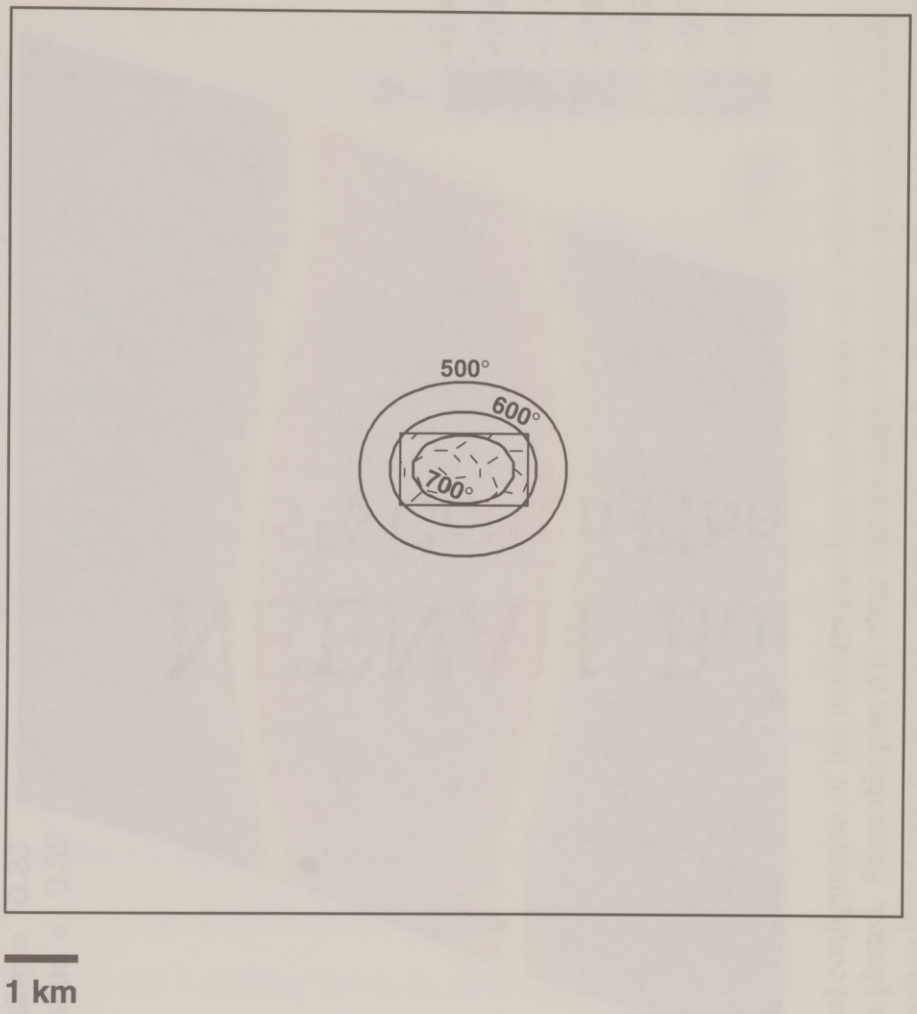


Figure 4.6: Temperature at start of deformation (10 ky after intrusion).

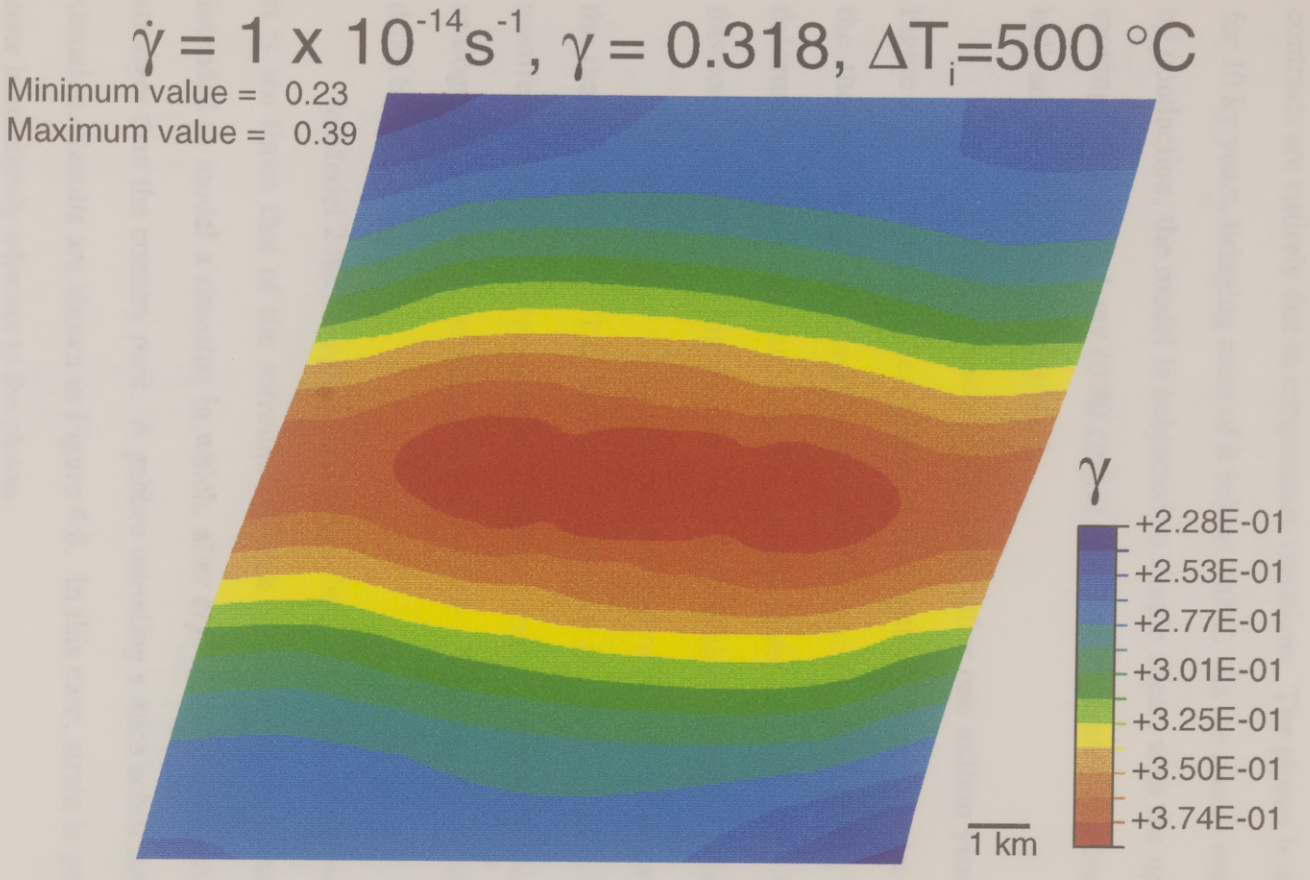


Figure 4.7: Model 1. The final configuration of the uniform rheology model after one million years of deformation. Contours of shear strain ($\gamma$) are plotted. From this plot it is clear that the thermal anomaly associated with the cooling pluton has concentrated deformation into a zone running through the center of the model. Values of $\gamma$ in this zone are up to 69% higher than in the least strained parts of the model.

contrasts are entirely due to temperature variations. The pluton is allowed to cool for 10 ky years, bringing most of it below 700°C. As the pluton continues to cool by conduction, the model is subjected to simple shear, with the upper boundary moving 7.96 km in 1 my (0.80 cm/yr). This displacement rate corresponds to a bulk shear strain rate of $1x10^{-14}$ $s^{-1}$.

The final configuration of the model after one million years is shown in Figure 4.7. Contours of shear strain ($\gamma$) are plotted. From this plot it is clear that the thermal anomaly associated with the cooling pluton has concentrated deformation into a zone running through the center of the model. Values of $\gamma$ in this zone are up to 69% higher than in the least strained parts of the model.

The zone of high shear strain extends laterally beyond the zone affected by the thermal anomaly. The lateral extension of the shear zone is most likely a manifestation of the stress concentration around the thermally weakened zone, analogous to stress concentration around a hole. This effect is illustrated in more detail below.

In Model 2 the strength of the pluton begins to increase below 600°C, until it is ten times that of the surrounding rock at the same temperature. This is intended to model a situation in which, after crystallization, the pluton becomes stronger than the country rock. A gabbro intruding a mica schist might be such a situation. Results are shown in Figure 4.8. In this case, strain is partitioned in a zone immediately adjacent to the pluton.

Model 3 estimates the effect of the applied displacement rate. The strain rate is $2 \times 10^{-14}$ $s^{-1}$ (6.4 cm/yr displacement rate) and same total displacement is the same as Models 1 and 2. Time elapsed during deformation is 500 ky. As in

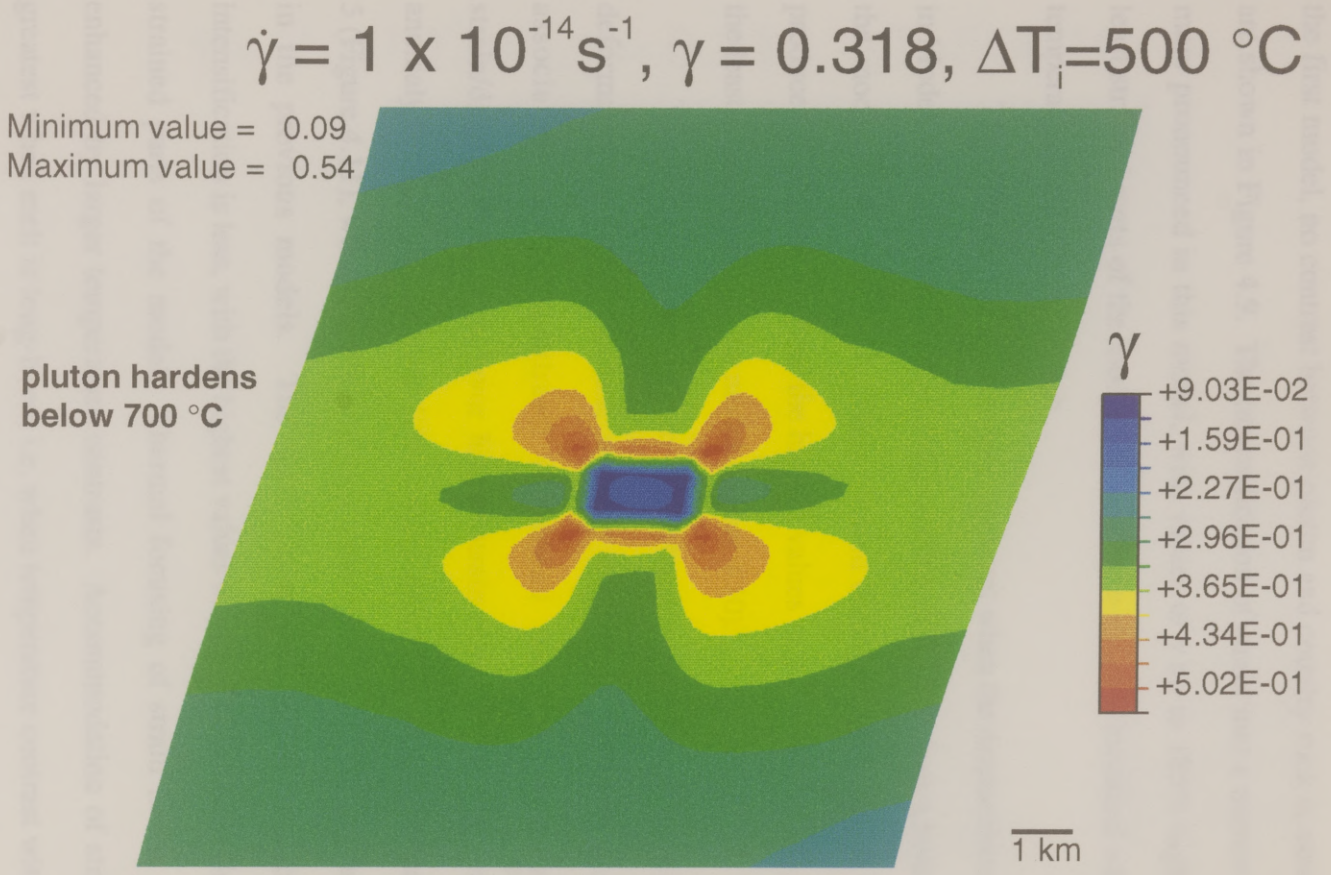


Figure 4.8: Model 2. The effect of a contrast in strength which changes as the pluton cools, This model is identical to model 1 (Figure 7), with the exception that the strength of the pluton begins to increase below 600°C until it is ten times that of the surrounding rock at the same temperature. In this case strain is partitioned in a zone immediately adjacent to the pluton.

the first model, no contrast between pluton and country rock is assumed. Results are shown in Figure 4.9. The intensification of strain into a narrow zone is much more pronounced in this model, with values of $\gamma$ up to 185% higher than in the least strained parts of the model. Much of the strain is localized where and when temperature gradients were high.

The effect of rate is even more apparent when the displacement rate is raised in Model 4 to 12.8 cm/yr, a high but plausible value that gives a bulk strain rate for the model of $4 \times 10^{-14}$ $s^{-1}$. Time elapsed during deformation is 250 ky. This produces a shear zone where the highest values of $\gamma$ are up to 607% higher than in the least strained parts of the model (Figure 4.10).

The models demonstrate the interplay between the rate of regional deformation and the magnitude and rate of decay of the thermal anomaly (and associated strength contrast) associated with the intrusion. Higher strain/displacement rates favor higher strain shear zones. A smaller thermal anomaly should create a more diffuse shear zone. This is demonstrated by Model 5 (Figure 4.11), where the country rock temperature is 600°C, instead of 400°C as in the previous models. The shear zone produced is broader, and strain intensification is less, with the highest values of $\gamma$ only 47% higher than in the least strained parts of the model. Thermal focusing of strain in the solid state is enhanced by larger temperature contrasts. Accommodation of strain in melt is greatest when melt is long-lived, i.e. when temperature contrast with wall rock is low. This result indicates that the process of thermal focusing of strain is likely to be more important at mid- and upper crustal levels, whereas melt accommodated strain will be more important at depth.

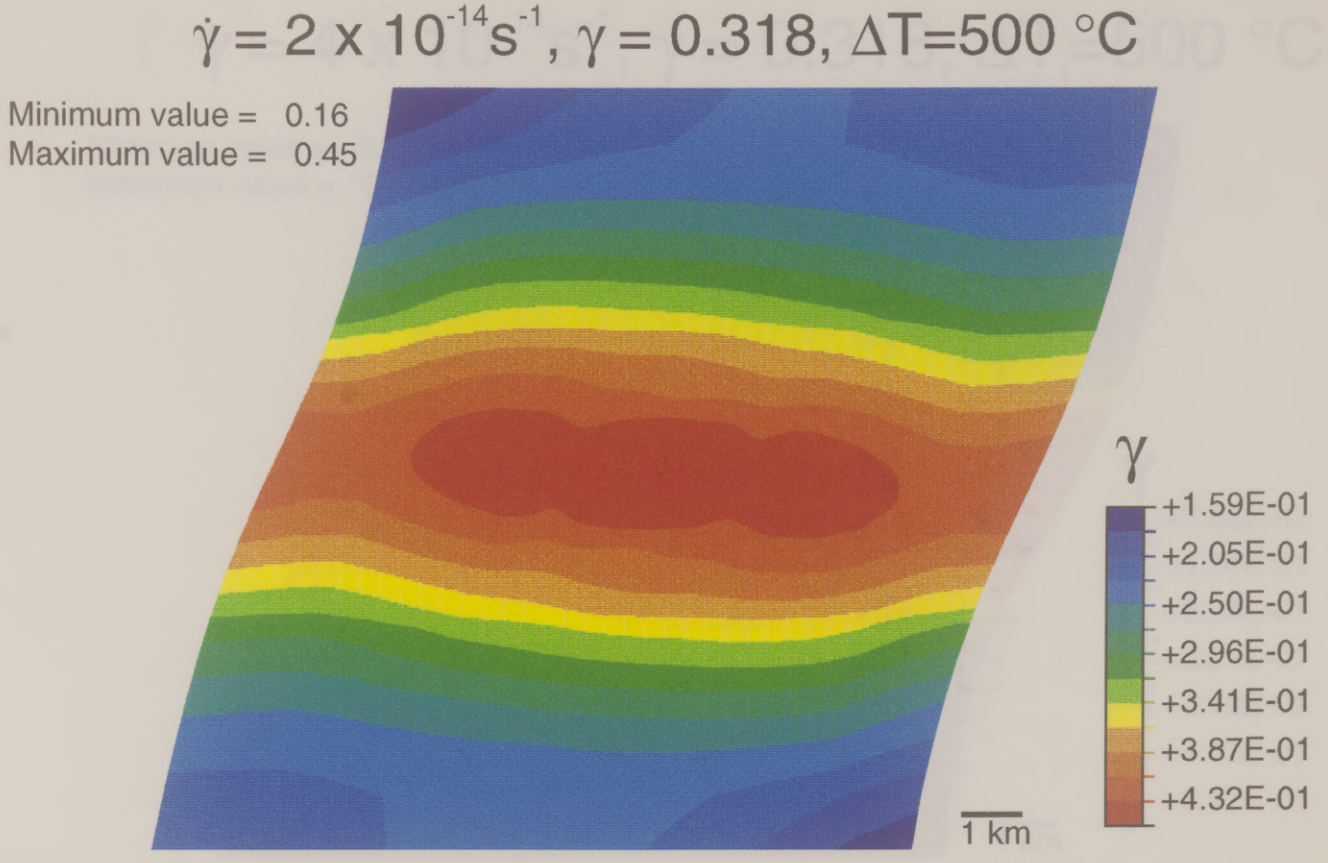


Figure 4.9: The final configuration (after 500 ky of deformation) of Model 3, with a strain rate of $2 \times 10^{-14} s^{-1}$ (6.4 cm/yr displacement rate). Simple shear strain ($\gamma$) is contoured. As in the first model, no contrast between pluton and country rock is assumed. The intensification of strain into a narrow zone is much more pronounced in this model, with the highest values of $\gamma$ up to 185% higher than in the least strained parts of the model. This is because much of the deformation took place when temperature gradients were high.

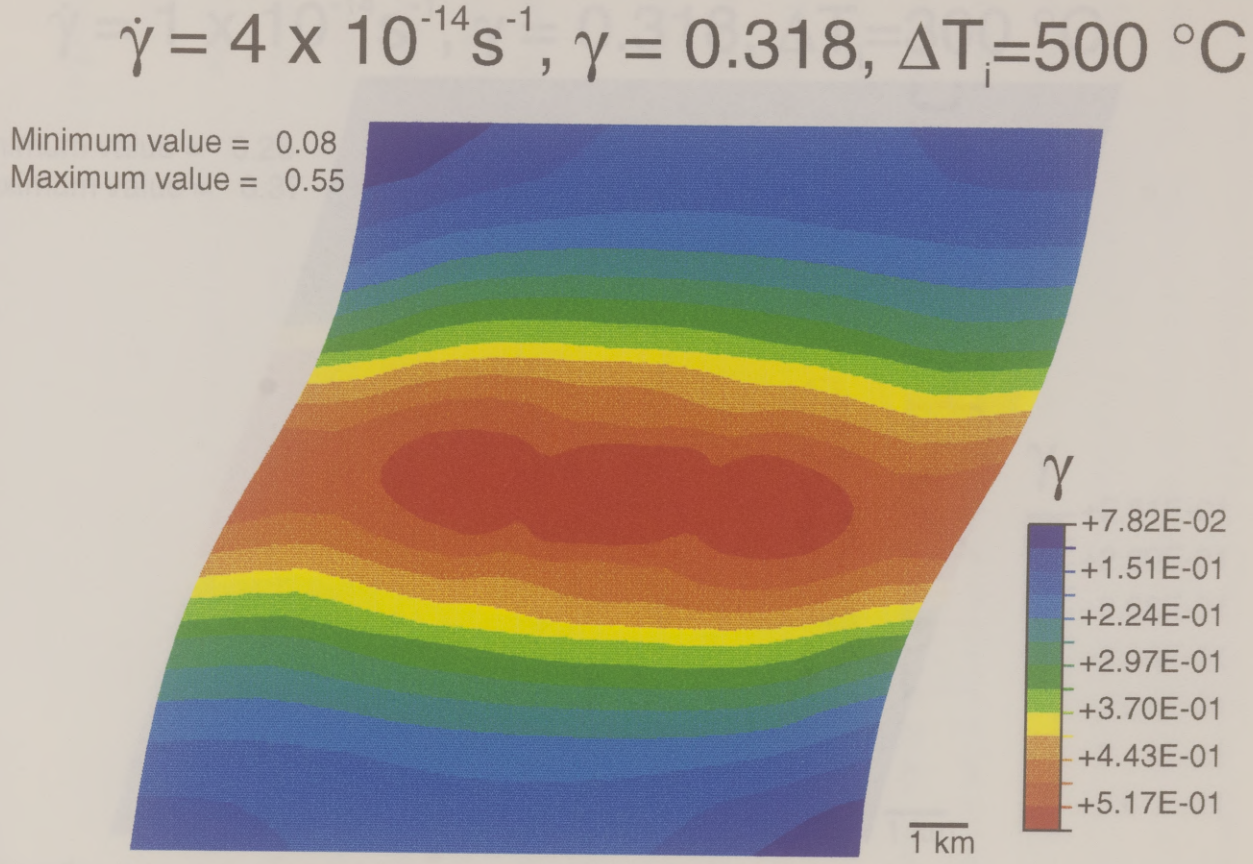


Figure 4.10: The final configuration (after 250 ky of deformation) of Model 4, with a strain rate of 4 x $10^{-14}s^{-1}$ Simple shear strain ($\gamma$) is contoured. Displacement rate is 12.8 cm/yr, a high but plausible value. This produces a shear zone where the highest values of $\gamma$ are up to 607% higher than in the least strained parts of the model.

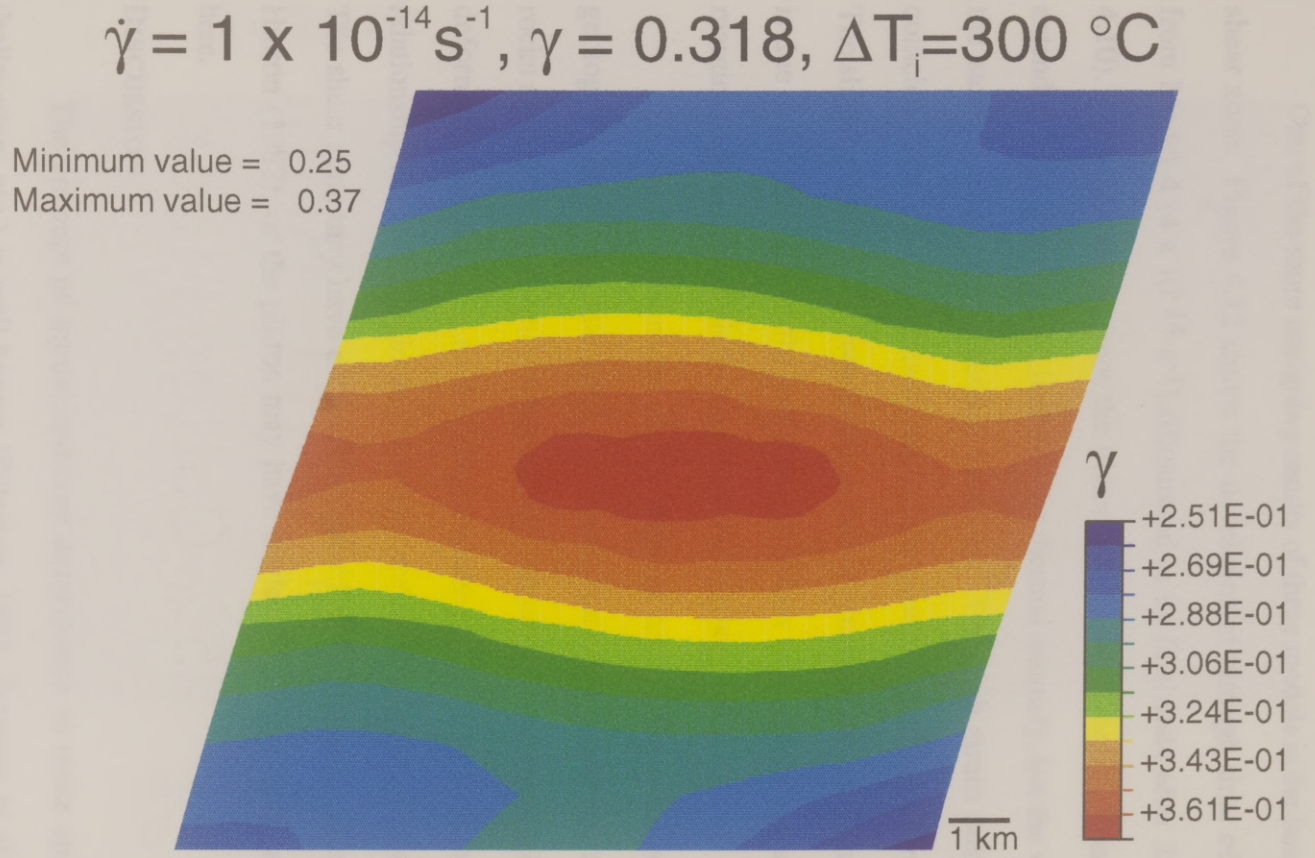


Figure 4.11: The final configuration (after 1 my of deformation) of Model 5, where the country rock temperature is 600°C, instead of 400°C as in the previous models. Simple shear strain ($\gamma$) is contoured. The shear zone produced is broader, and intensification is less, with the highest values of $\gamma$ only 47% higher than in the least strained parts of the model. This indicates that the process of thermal focusing of strain is likely to be more important at mid- and upper crustal levels, whereas melt accommodated strain will be more important at depth.

One of the more intriguing results of these models is the lateral extent of the shear zone. Figure 4.12 shows the development through time of the shear zone from Model 4 ($4 \times 10^{-14}$ $s^{-1}$) (illustrated in its final state after 250 ky in Figure 4.10). Note that throughout the history, the zone of higher than average strain extends laterally beyond the limits of the thermal anomaly, but the vertical extent is the same as that of the thermal anomaly. The high strain zone in the center coincides with the pluton itself, and grows simultaneously outwards and inwards. The slightly lower strain zone in the center of pluton in the early parts of the model is due to the inability of the low strength pluton to transfer displacement from its margins to its center. This decoupling effect is short lived.

The lateral extension of the zone of high strain is important for field geologists, or anyone interpreting regional fabrics of deformed, metamorphosed rocks associated with igneous intrusions. Although a worker might recognize the deformation adjacent to an intrusion as being related to the body, the genetic relationship between a regional shear zone and a pluton could easily be overlooked. The shear zone may have created the space for the pluton to intrude as shown in Hutton (1982), or the pluton may have nucleated a shear zone, as hypothesized here.

## DISCUSSION

The concept of intrusion-driven deformation to make space for magma (ballooning, etc.) is well known (Paterson, 1989; Paterson et al., 1991b). The ability of liquid melt to accommodate large, rapid displacements is well established (Hollister and Crawford, 1986; Davidson and Hollister, 1992; Hollister, 1993;

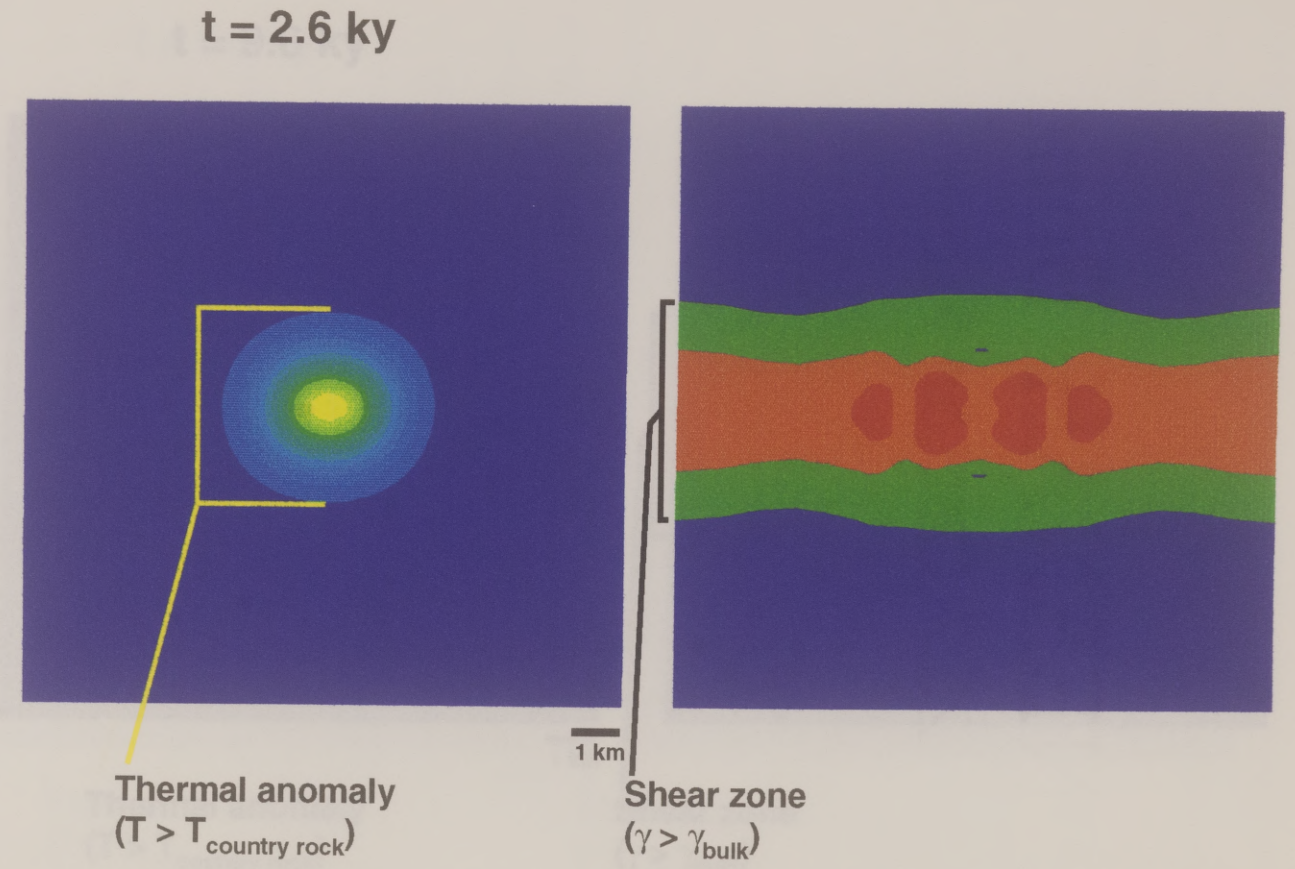


Figure 4.12a: This figure shows the development of the shear zone from model 4 (4 x $10^{-14}$ $s^{-1}$ strain rate, illustrated in its final state in figure 10). Note that throughout the history the shear zone extends laterally beyond the limits of the thermal anomaly, but the vertical extent is the same as that of the thermal anomaly. The high strain zone in the center coincides with the pluton itself, and grows simultaneously outwards and inwards. The slightly lower strain zone in the center of the early parts of the model is due to the inability of the low strength pluton to transfer displacement from its margins to its center. This decoupling effect is short lived.

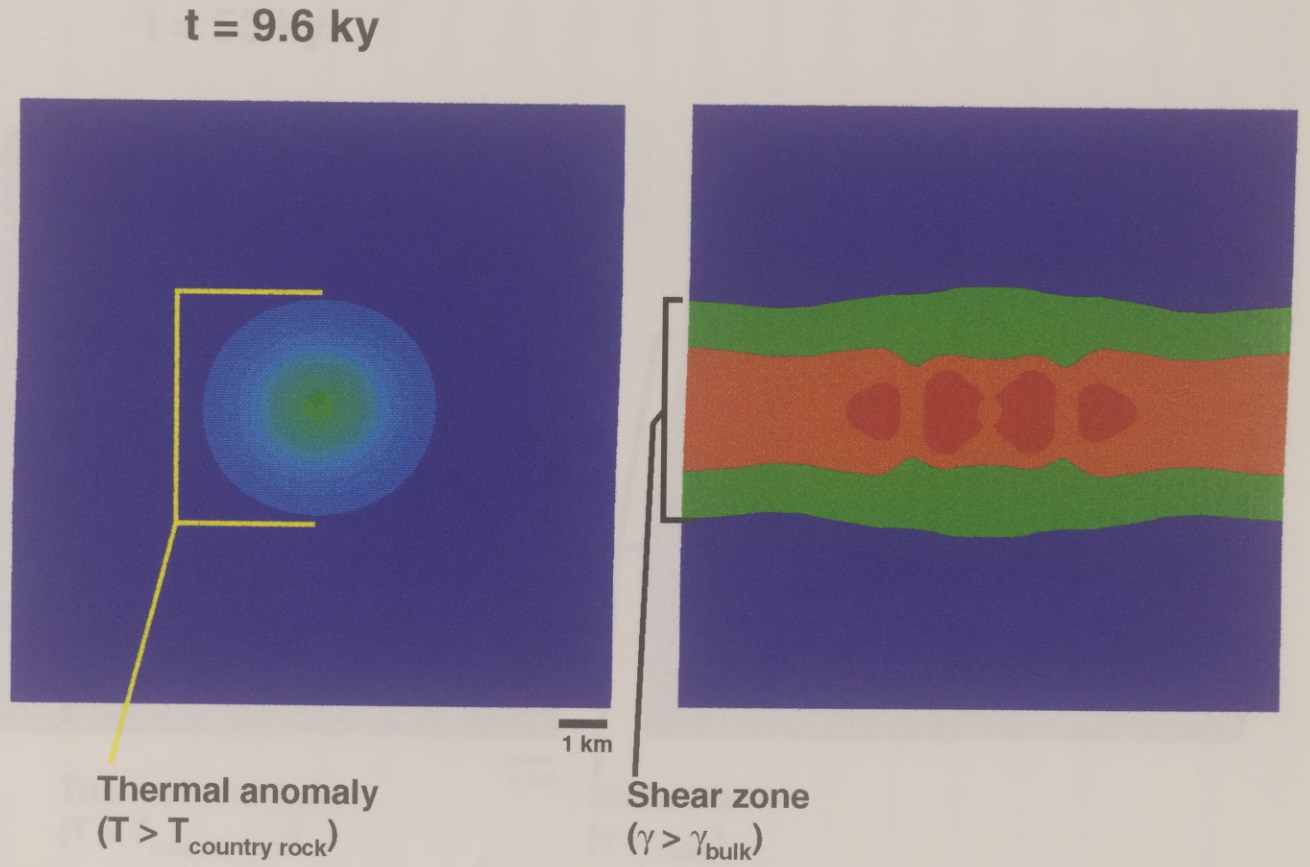


Figure 4.12b: Continued growth of shear zone, t=9600 years since start of deformation.

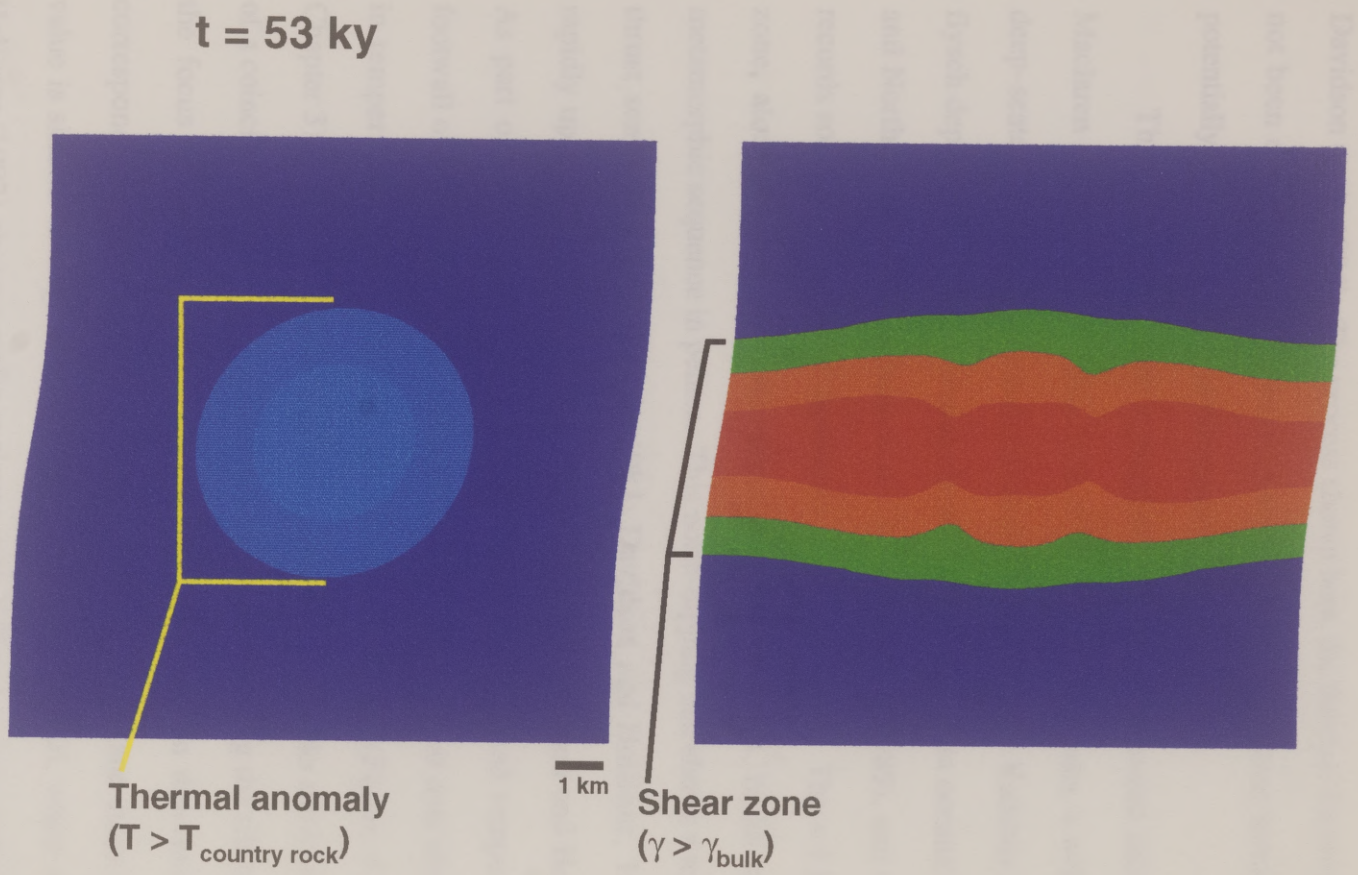


Figure 4.12c: Continued growth of shear zone, t= 53,000 years since deformation began.

Davidson et al., 1994). The process shown here, the thermal focusing of strain, has not been explicitly considered in many studies. Here some examples show the potentially wide occurrence of this process.

The first example of a potential thermally nucleated shear zone is the Maclaren Glacier Metamorphic Belt of south-central Alaska, a well documented, deep–seated (~20 km) shear zone in the pelitic rocks of the Kahiltna terrane. These flysch deposits mark the boundary between the Wrangellia oceanic basalt plateau and North America (Nokleberg et al., 1985; Wallace, 1989), and the shear zone records some, if not most of the history of this boundary. The ~ 1 km thick shear zone, along with several kilometers of footwall rocks, make up an inverted metamorphic sequence in pelites. This north-dipping belt shows a top-to-the-south thrust sense of motion (Smith, 1981; Davidson and Hollister, 1992) and was rapidly uplifted along a melt-bearing shear zone (Davidson and Hollister, 1992). As part of their study, Davidson et al. (1992) measured temperatures in the footwall of this belt using garnet-biotite thermometry. Their data show an increase in temperature with decreasing distance from the sill (Figure 4.13a, see also Chapter 3). Analysis of porphyroblasts in the footwall rocks shows some evidence of a coincident gradient in strain (Figure 4.13b), indicating the sill may have been the focus of footwall deformation. The highest strain determined ($\gamma$ = 3.2) corresponds to a strain ellipsoid X/Z ratio (assuming plane strain) of 12. This value is similar in magnitude to strain recorded in the sill, where Davidson and Hollister (1992) observe mafic enclaves with X/Z ratios ranging from 8 to 18. If the average strain determined from biotite porphyroblasts ($\gamma$ = 2.8) is extrapolated over the 1.45 km structural thickness of the section considered in Chapter 3, a

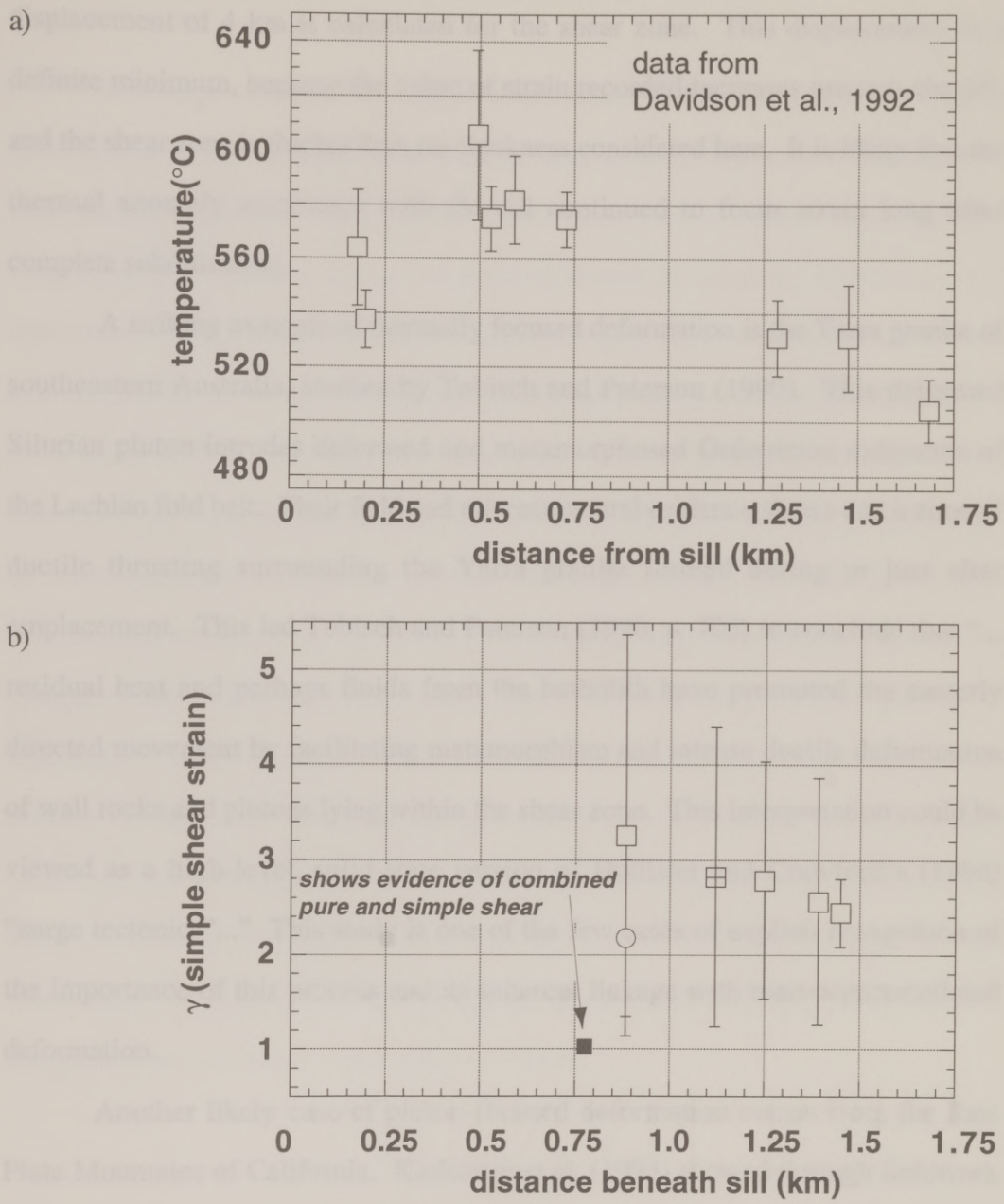


Figure 4.13: Garnet biotite thermometry (a) shows increasing temperature approaching the sill (Davidson et al., 1992). Analysis of porphyroblasts in the footwall rocks suggests a coincident gradient in strain (b), pointing to the sill as the focus of footwall deformation (details in Chapter 3). It is likely that the thermal anomaly associated with the sill continued to focus strain long after all melt was crystallized.

displacement of 4 km is calculated for the shear zone. This displacement is a definite minimum, because the value of strain recorded increases towards the sill, and the shear zone is thicker than the thickness considered here. It is likely that the thermal anomaly associated with the sill continued to focus strain long after complete solidification.

A striking example of thermally focused deformation is the Yarra granite of southeastern Australia, studied by Tobisch and Paterson (1990). This deformed Silurian pluton intrudes deformed and metamorphosed Ordovician sediments of the Lachlan fold belt. Their field and microstructural evidence shows that a zone of ductile thrusting surrounding the Yarra granite formed during or just after emplacement. This led Tobisch and Paterson (1990, p. 703) to conclude that "... residual heat and perhaps fluids from the batholith have promoted the easterly directed movement by facilitating metamorphism and intense ductile deformation of wall rocks and plutons lying within the shear zone. This interpretation could be viewed as a high-level, solid-state version of Hollister and Crawford's (1986) "surge tectonics"..." This study is one of the few cases of explicit recognition of the importance of this process and its inherent linkage with melt-accommodated deformation.

Another likely case of pluton-focused deformation comes from the East Piute Mountains of California. Karlstrom et al. (1993) showed through fieldwork and petrography that ductile deformation of pluton and wallrock occurred while melt was present. Thus this is a site where both melt-accommodated deformation (Hollister and Crawford, 1986; Hollister, 1993) and thermally focused deformation is operative.

## CONCLUSIONS

In models of simultaneous heat conduction and deformation using realistic thermal and mechanical properties, the thermal anomaly associated with a pluton concentrates shear strain into a narrow zone. If the pluton hardens (relative to the country rock) as it cools, strain is concentrated near its margins. Higher regional strain rates cause more focusing of strain, and higher strain shear zones. Duration and magnitude of the thermal anomaly are important factors in determining the final strain concentration into the shear zone. A zone of high strain may extend laterally away from the pluton, and the role of the pluton in creating the zone may be unrecognized if workers are unaware of this possibility. Because of the high heat content of magmas, the association of plutonism with tectonism, and the strongly temperature-dependent strength of rocks, it is likely that this process is important in many settings. While this study considers only the well-quantified process of thermally activated creep, other effects not considered (grain size reduction, reaction-enhanced ductility, foliation development) will augment the basic process of thermally focused deformation. Careful attention to the relationship of magmatism and deformation, and measurement of strain and temperature are necessary to recognize this effect.

## References


Barton, M. D., and Hansen, R. B., 1989, Magmatism and the development of low pressure metamorphic belts: Implications from the western United States and thermal modeling: Geological Society of America Bulletin, v. 101, p. 1051-1065.

Bowers, J. R., Kerrick, D. M., and Furlong, K. P., 1990, Conduction model for the thermal evolution of the Cupsuptic aureole, Maine: American Journal of Science, v. 290, p. 644-665.

Brun, J. P., and Cobbold, P. R., 1980, Strain heating and thermal softening in continental shear zones: A review: Journal of Structural Geology, v. 2, p. 149-158.

Brun, J. P., and Pons, J., 1981, Strain patterns of pluton emplacement in a crust undergoing non-coaxial deformation, Sierra Morena, Southern Spain: Journal of Structural Geology, v. 3, p. 219-229.

Carslaw, H. S., and Jaeger, J. C., 1959, Conduction of heat in solids: Oxford, Clarendon Press, 510 p.

Davidson, C., and Hollister, L. S., 1992, Role of melt in the formation of a deep-crustal compressive shear zone: The Maclaren Glacier Metamorphic Belt, South Central Alaska: Tectonics, v. 11, p. 348-359.

Davidson, C., Schmid, S. M., and Hollister, L. S., 1994, Role of melt during deformation in the deep crust: Terra Nova, v. 6, p. 133-142.

De Bremaecker, J.-C., and Becker, E. B., 1978, Finite element models of folding: Tectonophysics, v. 50, p. 349-367.

Fleitout, L., and Froidevaux, C., 1980, Thermal and mechanical evolution ofshear zones: Journal of Structural Geology, v. 2, p. 159-164.

Fletcher, J. M., and Karlstrom, K. E., 1990, Late Cretaceous ductile deformation, metamorphism and plutonism in the Piute mountains, easterm Mojave desert: Journal of Geophysical Research, v. 95, p. 487-500.

Gettings, M. E., 1988, Variation of the depth to the brittle-ductile transition due to cooling of a midcrustal intrusion: Geophysical Research Letters, v. 15, p. 213-216.

Gleason, G. C., and Tullis, J., 1993, Improving flow laws and piezometers for quartz and feldspar aggregates: Geophysical Research Letters, v. 20, p. 2111-2114.

Guglielmo, G., 1993, Interference between pluton expansion and non–coaxial tectonic deformation: Three–dimensional computer model and field implications: Journal of Structural Geology, v. 15, p. 593–608.

Hansen, R. B., and Barton, M. D., 1989, Thermal development of low-pressure metamorphic belts: Results from two-dimensional numerical models: Journal of Geophysical Research, v. 94, p. 10,363-10,377.

Hollister, L. S., 1993, The role of melt in the uplift and exhumation of orogenic belts: Chemical Geology, v. 108, p. 31-48.

Hollister, L. S., and Crawford, M. L., 1986, Melt-enhanced deformation: a major tectonic process: Geology, v. 14, p. 558-561.

Hutton, D. H. W., 1982, A tectonic model for the emplacement of the Main Donegal Granite, NW Ireland: Journal of the Geological Society of London, v. 139, p. 615–631.

Jaeger, J. C., 1961, The cooling of irregularly shaped igneous bodies: American Journal of Science, v. 259, p. 721-734.

Jaeger, J. C., 1964, Thermal effects of intrusions: Reviews of Geophysics, v. 2, p. 443-466.

Karlstrom, K., 1989, Towards a syntectonic paradigm for granitoids: EOS, v. 70, p. 762, 770.

Karlstrom, K. E., Miller, C. F., Kingsbury, J. A., and Wooden, J. L., 1993, Pluton emplacement along an active ductile thrust zone, Piute Mountains, southeastern California: Interaction between deformational and solidification processes: Geological Society of America Bulletin, v. 105, p. 213-230.

Kirby, S. H., and McCormick, J. W., 1989, Inelastic Properties of rocks and minerals: Strength and rheology, *in* Carmichael, R. S., ed., Physical properties of rocks and minerals: Boca Raton, CRC, p. 177-287.

Kohlstedt, D. L., Evans, B., and Mackwell, S. J., 1995, Strength of the lithosphere: Constraints imposed by laboratory experiments: Journal of Geophysical Research, v. 100, p. 17,587-17,602.

Lan, L., and Hudleston, P. J., 1991, Finite element models of buckle folds in non-linear materials: Tectonophysics, v. 9, p. 1-12.

Mares, V. M., and Kronenborg, A. K., 1993, Experimental deformation of muscovite: Journal of Structural Geology, v. 15, p. 1061-1075.

Nicolas, A., Bouchez, J. L., Blaise, J., and Poirier, J. P., 1977, Geological aspects of deformation in continental shear zones: Tectonophysics, v. 42, p. 55–73.

Nokleberg, W. J., Jones, D. L., and Silberling, N. J., 1985, Origin and tectonic evolution of the Maclaren and Wrangellia terranes, eastern Alaska Range, Alaska: Geological Society of America Bulletin, v. 96, p. 1251–1270.

Oxburgh, E. R., and Turcotte, D. L., 1970, The thermal structure of island arcs: Geological Society of America Bulletin, v. 81, p. 1665-1688.

Paterson, S. R., 1989, Are syntectonic granites truly syntectonic?: EOS, v. 70.

Paterson, S. R., Brudos, T., Fowler, K., Carlson, C., Bishop, K., and Vernon, R. H., 1991a, Papoose Flat pluton: forceful expansion or post-emplacement deformation?: Geology, v. 19, p. 324-327.

Paterson, S. R., Vernon, R. H., and Fowler, T. K., 1991b, Aureole tectonics, *in* Kerrick, D. K., ed., Contact Metamorphism: Washington, Mineralogical Society of America, p. 673-714.

Poirier, J. P., Bouchez, J. L., and Jonas, J. J., 1979, A dynamic model for aseismic ductile shear zones: Earth and Planetary Science Letters, v. 43, p. 441-453.

Shea, W. T., and Kronenberg, A. K., 1992, Rheology and deformation mechanisms of an isotropic mica schist: Journal of Geophysical Research, v. 97, p. 15,201-15,237.

Shreve, R. L., and Cloos, M., 1986, Dynamics of sediment subduction, melange formation, and prism accretion: Journal of Geophysical Research, v. 91, p. 10,229-10,245.

Singh, M. M., 1981, Strength of rock, *in* Toulokian, Y. S., Jud, W. R., and Roy, R. F., ed., Physical properties of rocks and minerals: New York, McGraw Hill, p. 83-121.

Smith, T. E., 1981, Geology of the Clearwater Mountains, South-central Alaska, Geologic Reports: Anchorage, Alaska Division of Geological and Geophysical Surveys, 72 p.

Tobisch, O. T., and Paterson, S. R., 1990, The Yarra Granite: an intradeformational pluton associated with ductile thrusting, Lachlan Fold Belt, southeastern Australia: Geological Society of America Bulletin, v. 102, p. 693-703.

Tullis, J. A., 1979, High temperature deformation of rocks and minerals: Reviews of Geophysics and Space Physics, v. 17, p. 1137-1154.

Turcotte, D. L., and Schubert, G., 1973, Frictional heating of the descending lithosphere: Journal of Geophysical Research, v. 78, p. 5876-5886.

Vernon, R. H., and Flood, R. H., 1988, Contrasting deformation styles of S– and I–type granitoids in the Lachlan Fold Belt, eastern Australia: Tectonophysics, v. 147, p. 127–143.

Wallace, W. K., Hanks, C. L., Rogers, J. F., 1989, The southern Kahiltna terrane: Implications for the tectonic evolution of southwestern Alaska: Geological Society of America Bulletin, v. 101, p. 1389–1407.

Wilks, K. R., and Carter, N. L., 1990, Rheology of some continental lower crustal rocks: Tectonophysics, v. 182, p. 57-77.

Zienkiewicz, O. C., and Taylor, R. L., 1989, The finite element method, v. 1: Basic formulations and linear problems: New York, McGraw Hill, 648 p.

Zienkiewicz, O. C., and Taylor, R. L., 1991, The finite element method, v. 2: Solid and fluid mechanics, dynamics, and non–linearity: New York, McGraw Hill.

# Appendix A

This appendix contains the result of all thermal models run for the study presented in Chapter 1. There are two plots per model, the first is a crystallization rate history (with a moving average curve fit), the second shows the shape of the magma chamber as crystallization progresses. In the second figure, the gray area represent material above the solidus, the stippled area is completely crystallized.

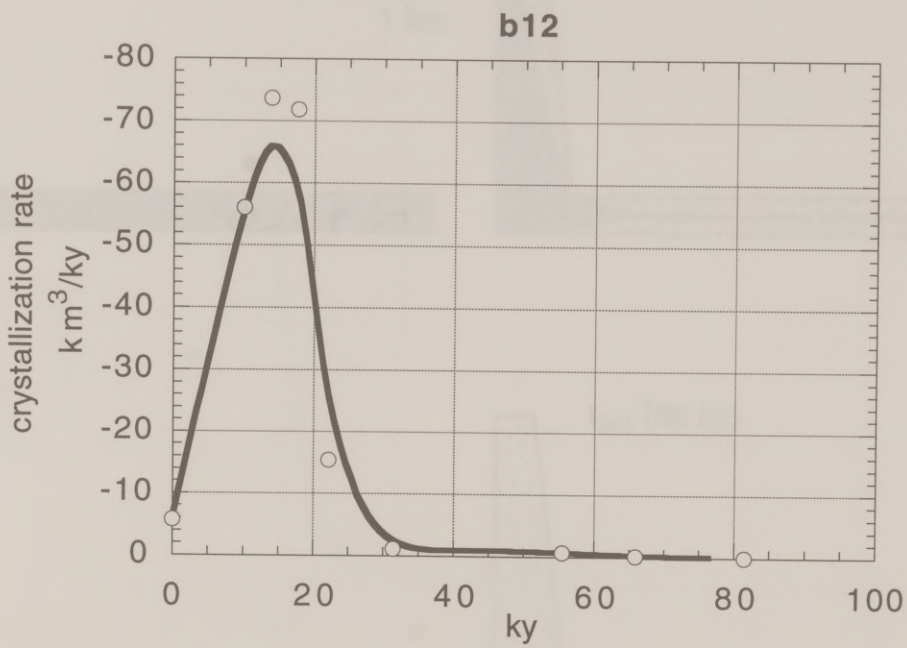
b12
crystallization rate
k m3/ky
-80
-70
-60
-50
-40
-30
-20
-10
0
0
20
40
60
80
100
ky

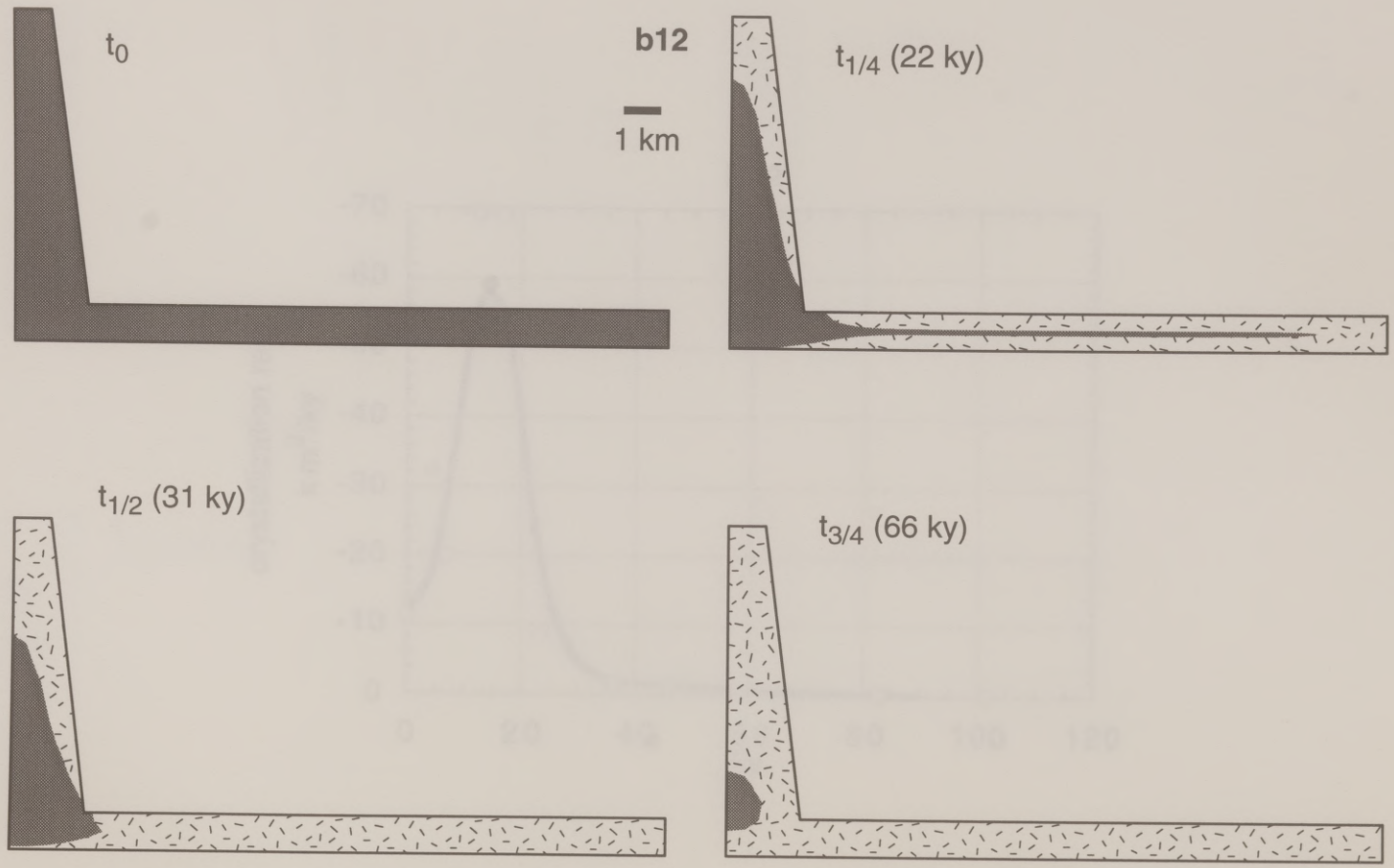
$t_0$
b12
1 km
$t_{1/4}$ (22 ky)
$t_{1/2}$ (31 ky)
$t_{3/4}$ (66 ky)

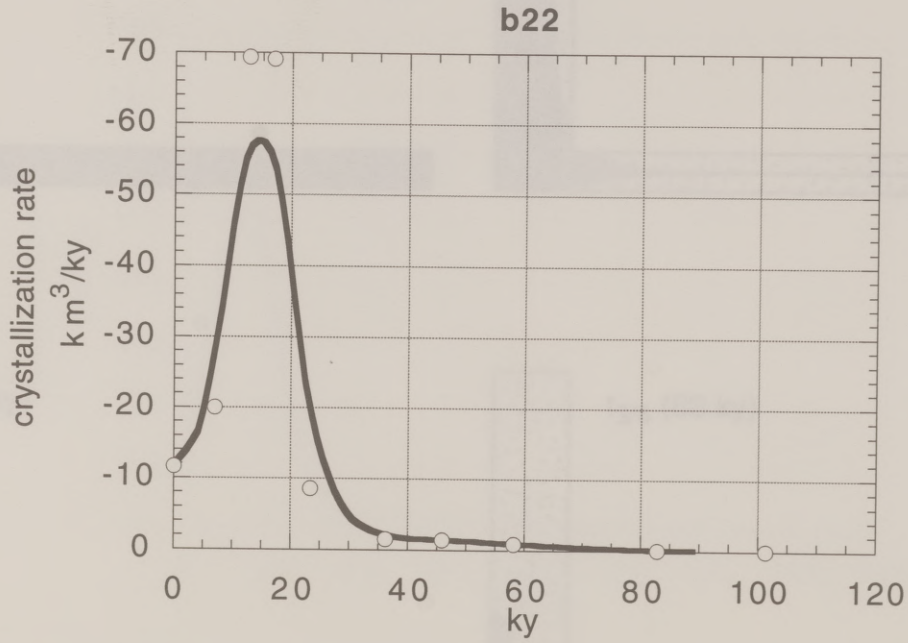
b22
crystallization rate
km3/ky
-70
-60
-50
-40
-30
-20
-10
0
0
20
40
60
80
100
120
ky

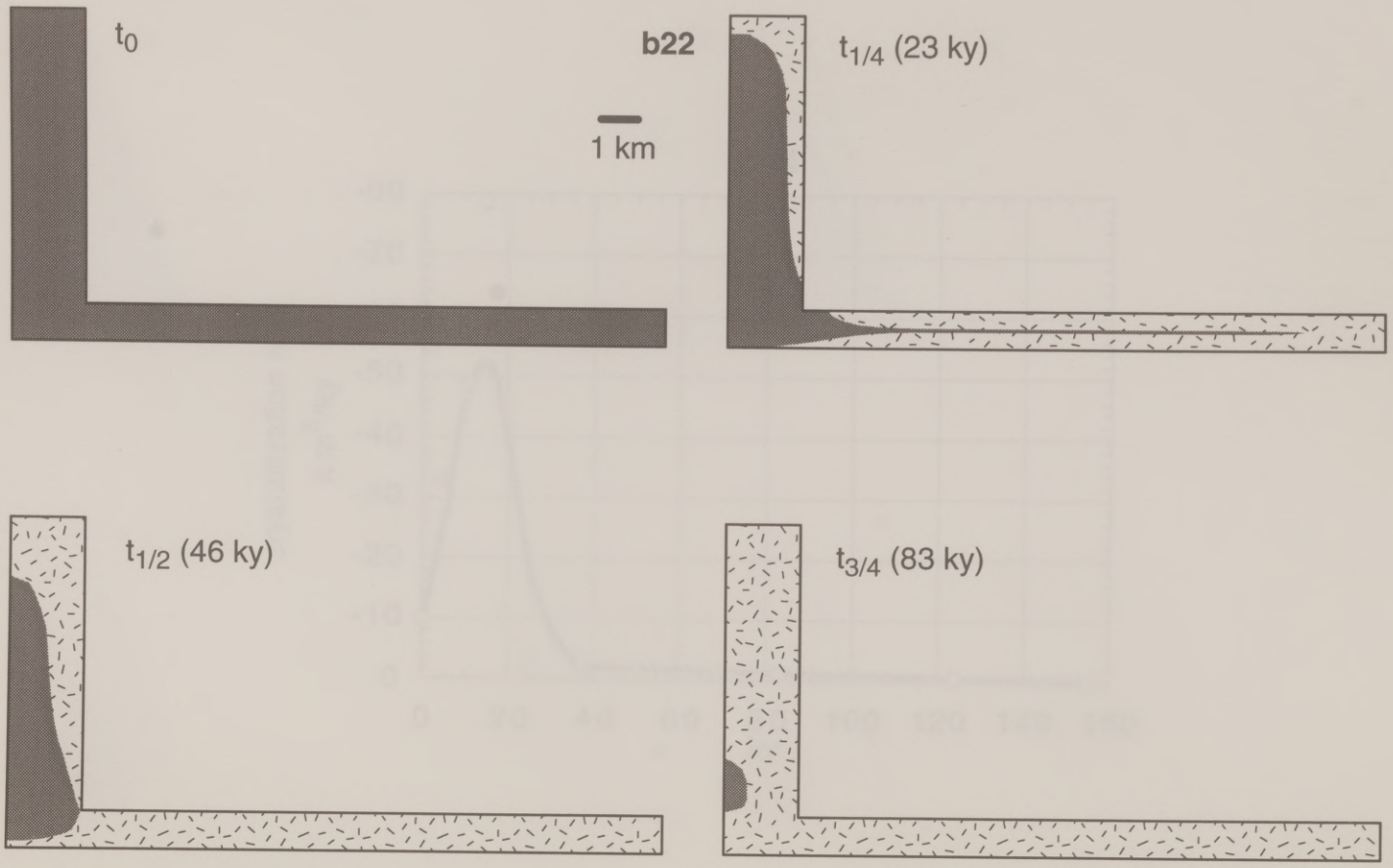
$t_0$
b22
1 km
$t_{1/4}$ (23 ky)
$t_{1/2}$ (46 ky)
$t_{3/4}$ (83 ky)

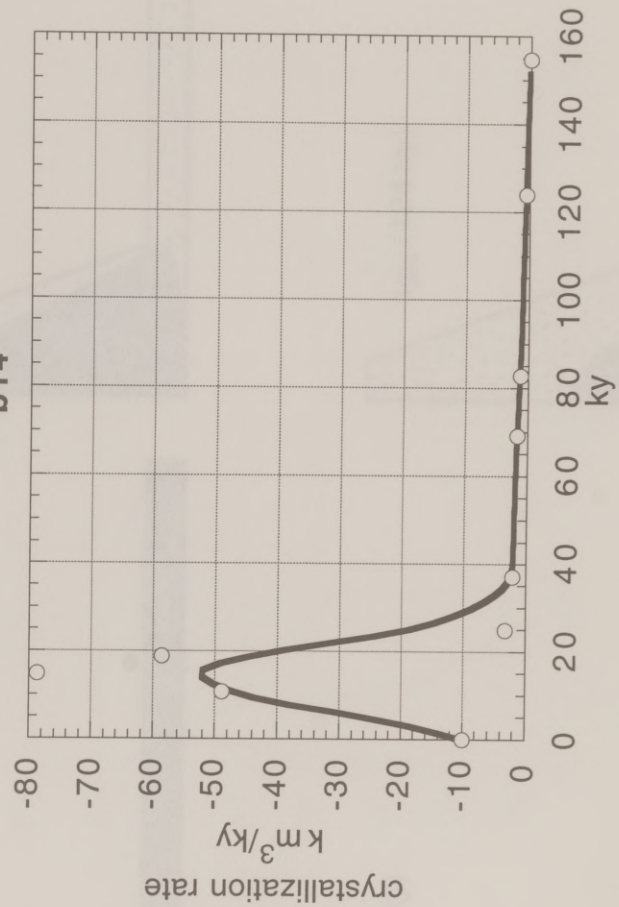
b14
crystallization rate
km³/ky
-80
-70
-60
-50
-40
-30
-20
-10
0
0
20
40
60
80
100
120
140
160
ky

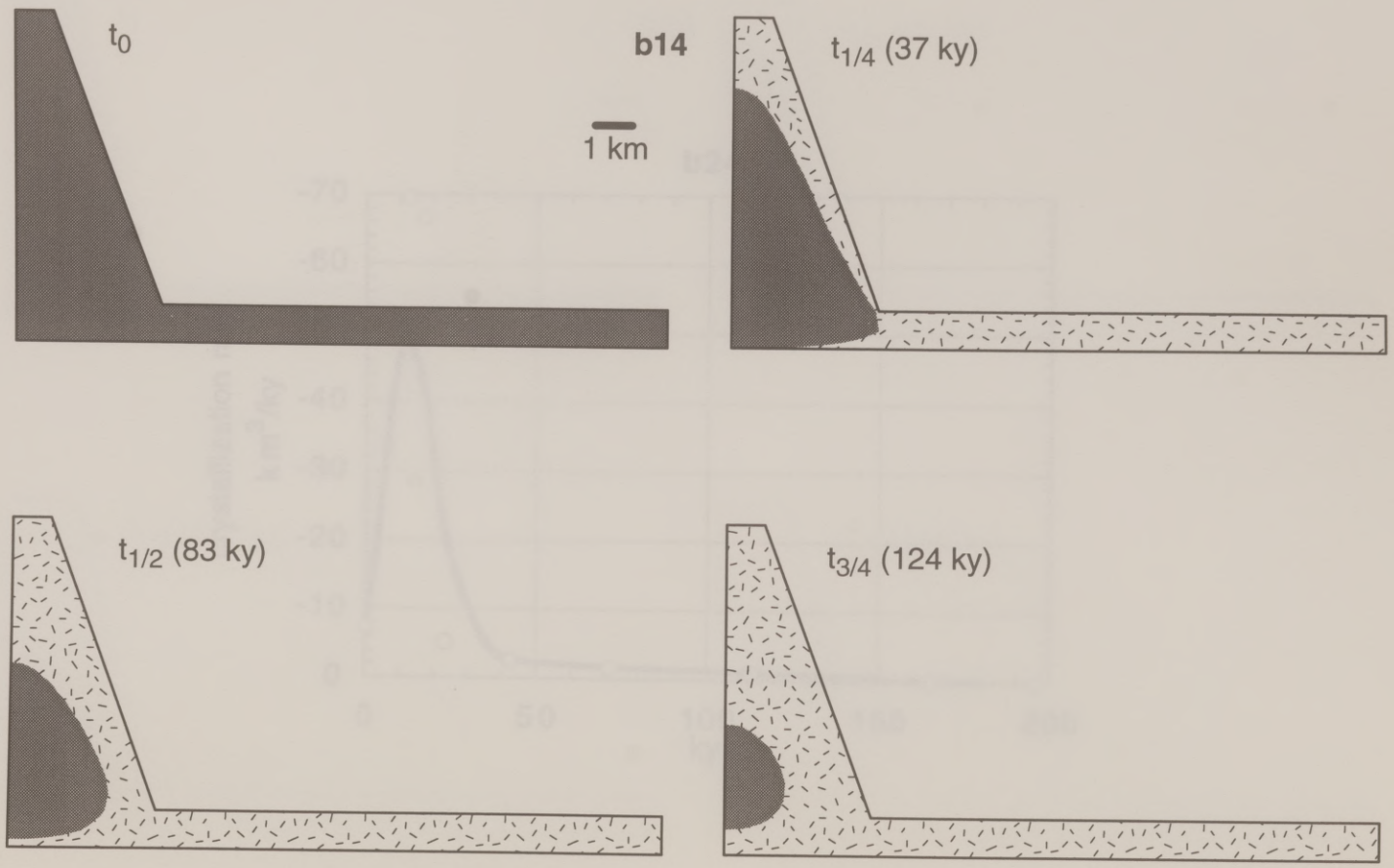
$t_0$
b14
1 km
$t_{1/4}$ (37 ky)
$t_{1/2}$ (83 ky)
$t_{3/4}$ (124 ky)

b24
crystallization rate
km3/ky
-70
-60
-50
-40
-30
-20
-10
0
0
50
100
150
200
ky

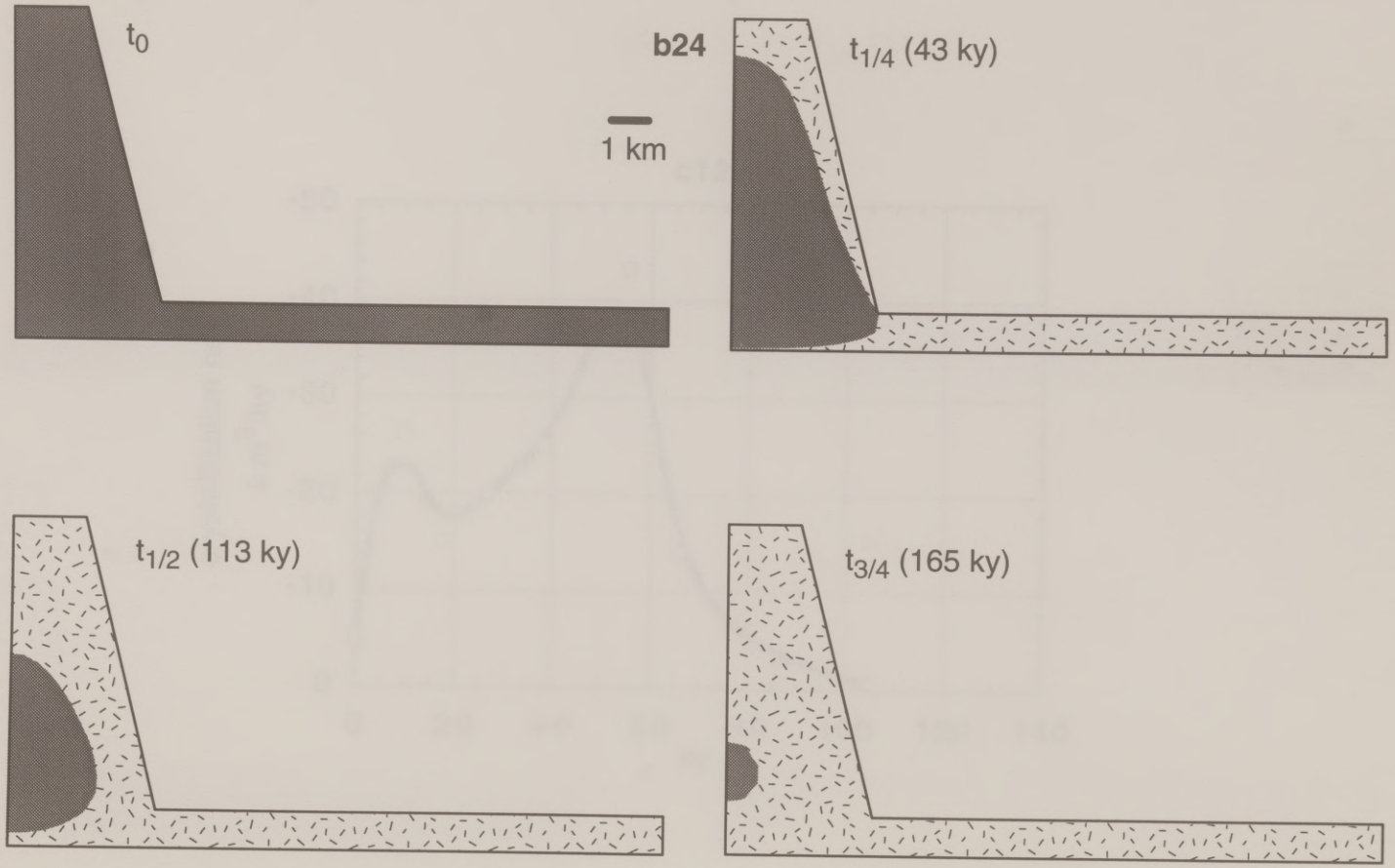
$t_0$
b24
1 km
$t_{1/4}$ (43 ky)
$t_{1/2}$ (113 ky)
$t_{3/4}$ (165 ky)

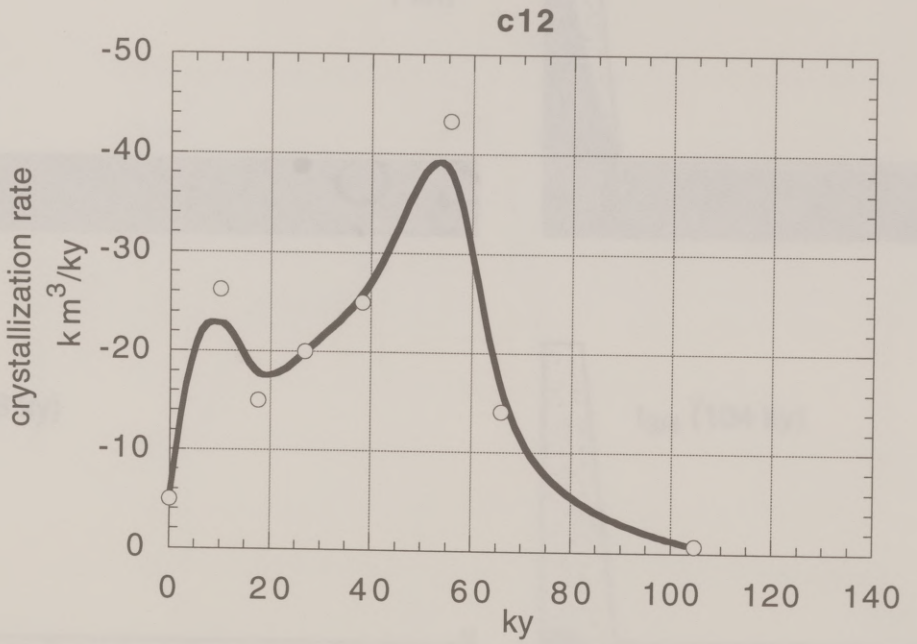
c12
crystallization rate
k m3/ky
-50
-40
-30
-20
-10
0
0
20
40
60
80
100
120
140
ky

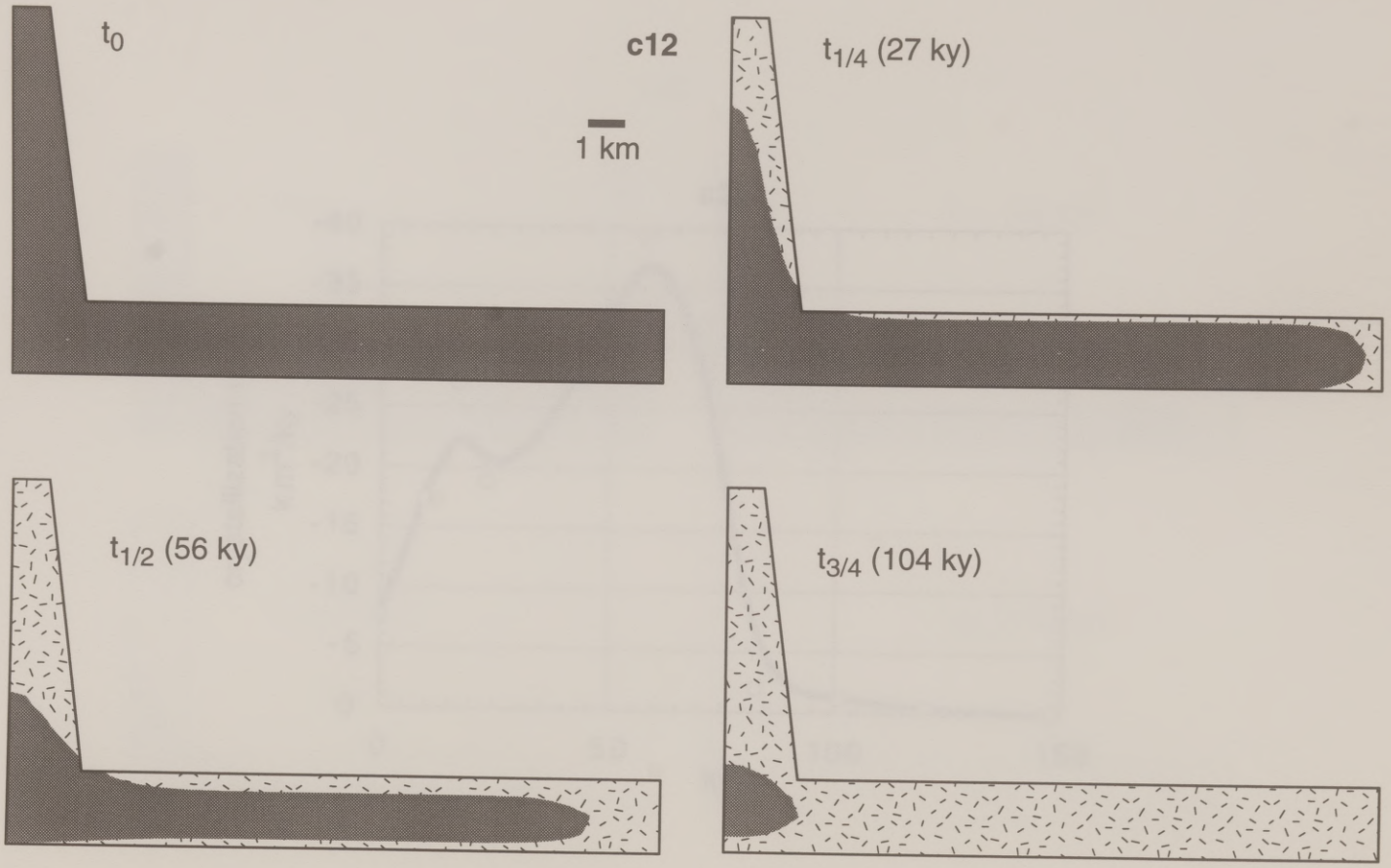
$t_0$
c12
1 km
$t_{1/4}$ (27 ky)
$t_{1/2}$ (56 ky)
$t_{3/4}$ (104 ky)

c22
crystallization rate
km3/ky
-40
-35
-30
-25
-20
-15
-10
-5
0
0
50
100
150
ky

c22

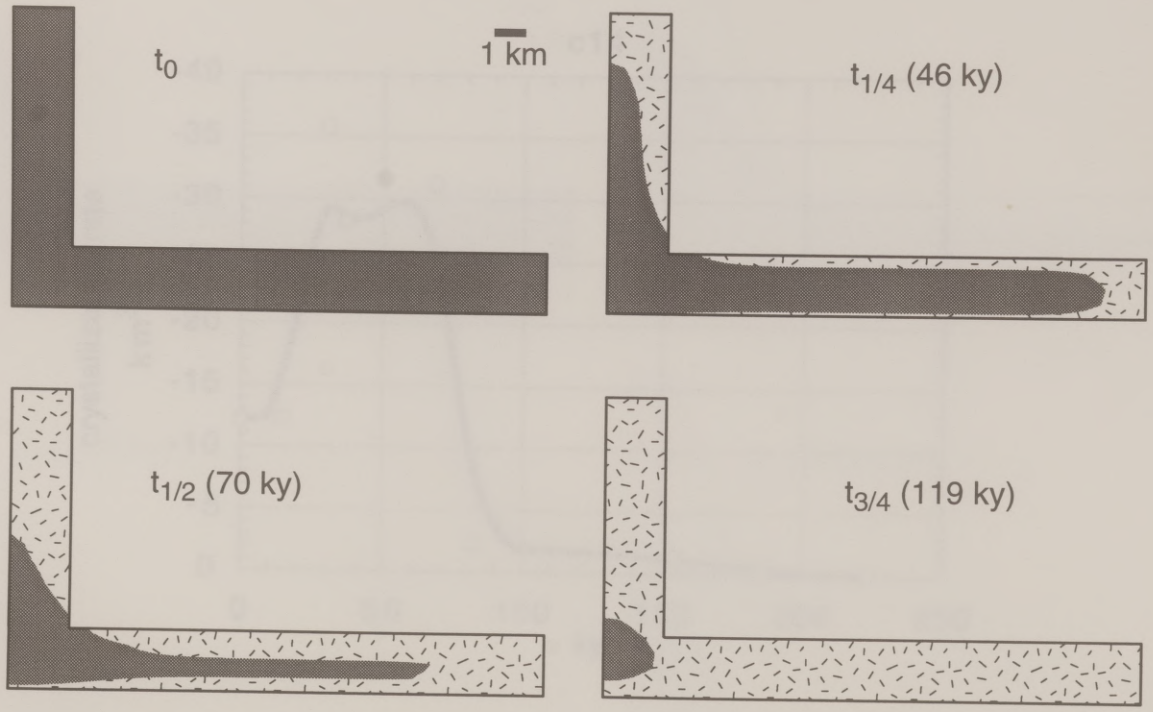

c14
crystallization rate
km3/ky
-40
-35
-30
-25
-20
-15
-10
-5
0
0
50
100
150
200
250
ky

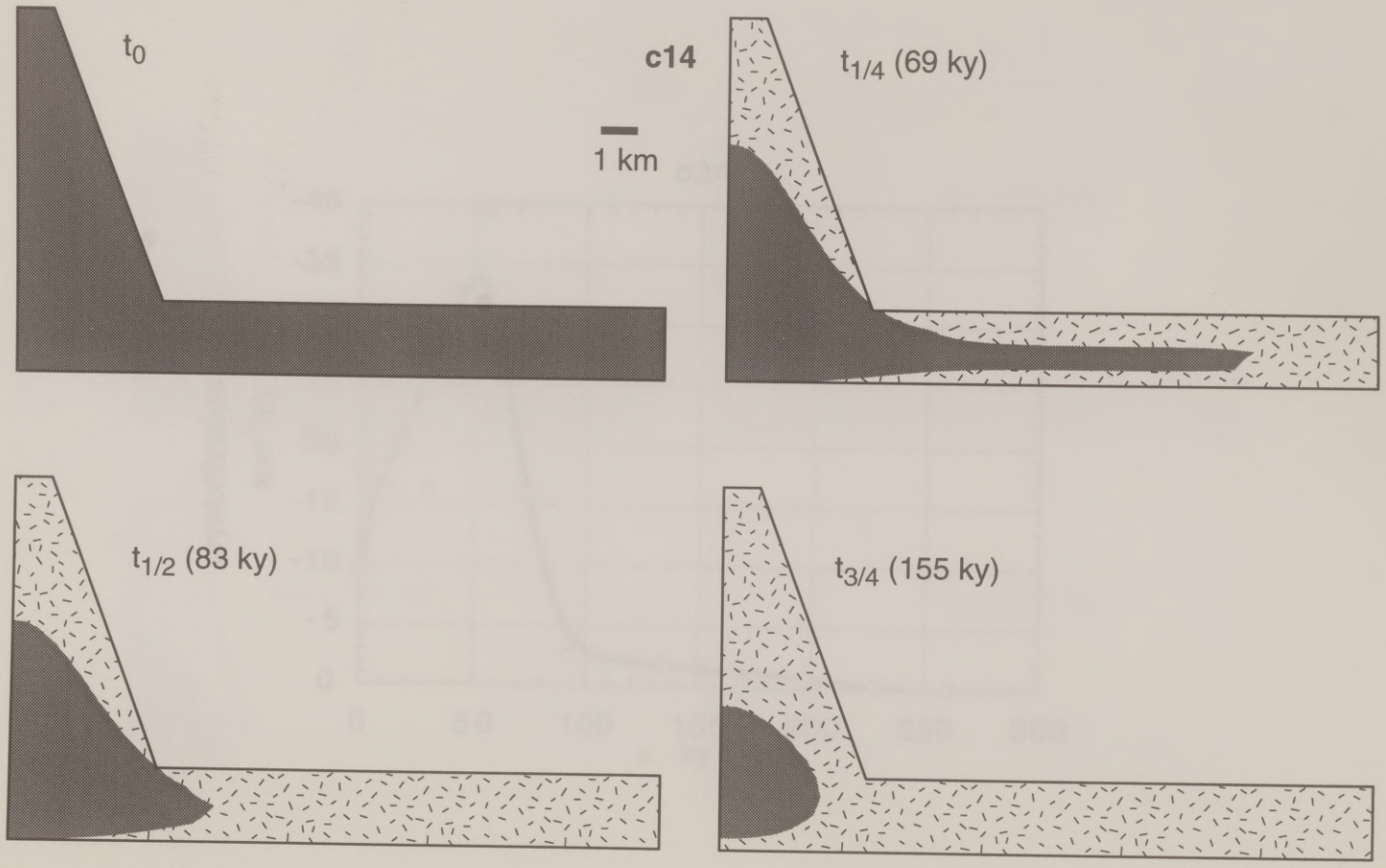
$t_0$
c14
1 km
$t_{1/4}$ (69 ky)
$t_{1/2}$ (83 ky)
$t_{3/4}$ (155 ky)

c24
crystallization rate
km3/ky
-40
-35
-30
-25
-20
-15
-10
-5
0
0
50
100
150
200
250
300
ky

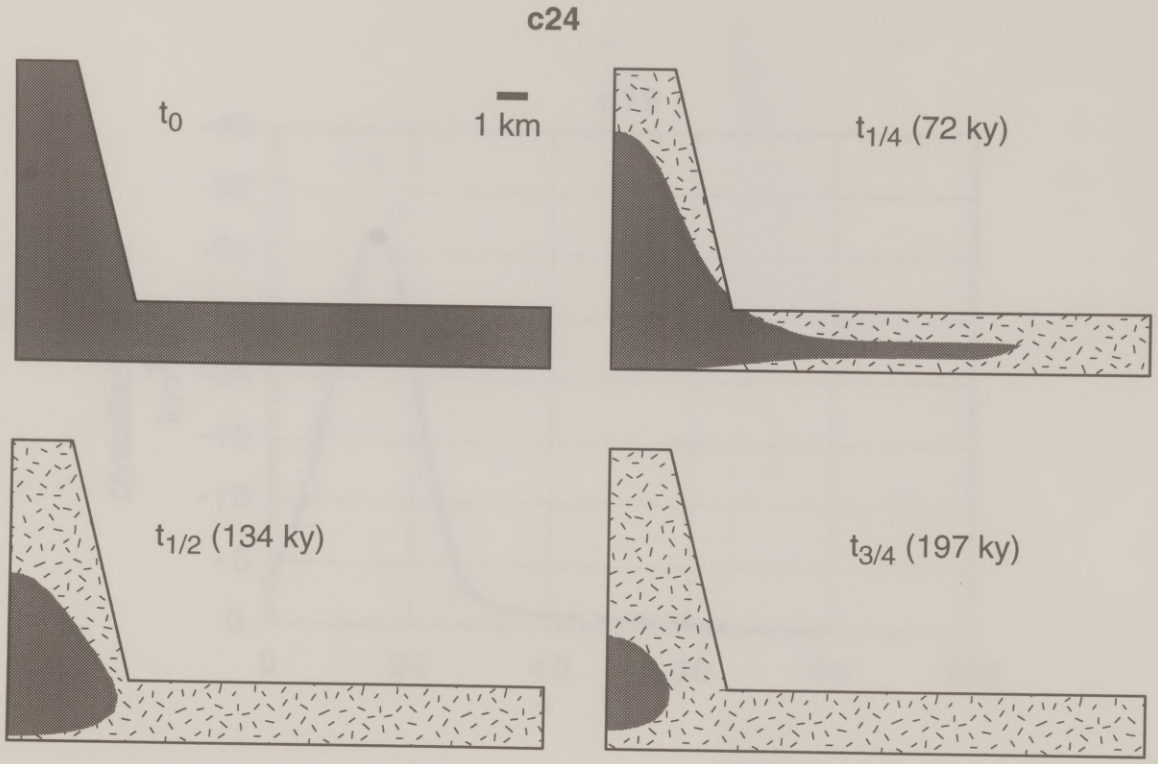
c24
$t_0$
1 km
$t_{1/4}$ (72 ky)
$t_{1/2}$ (134 ky)
$t_{3/4}$ (197 ky)

d12
crystallization rate
km3/ky
-40
-35
-30
-25
-20
-15
-10
-5
0
0
20
40
60
80
100
ky

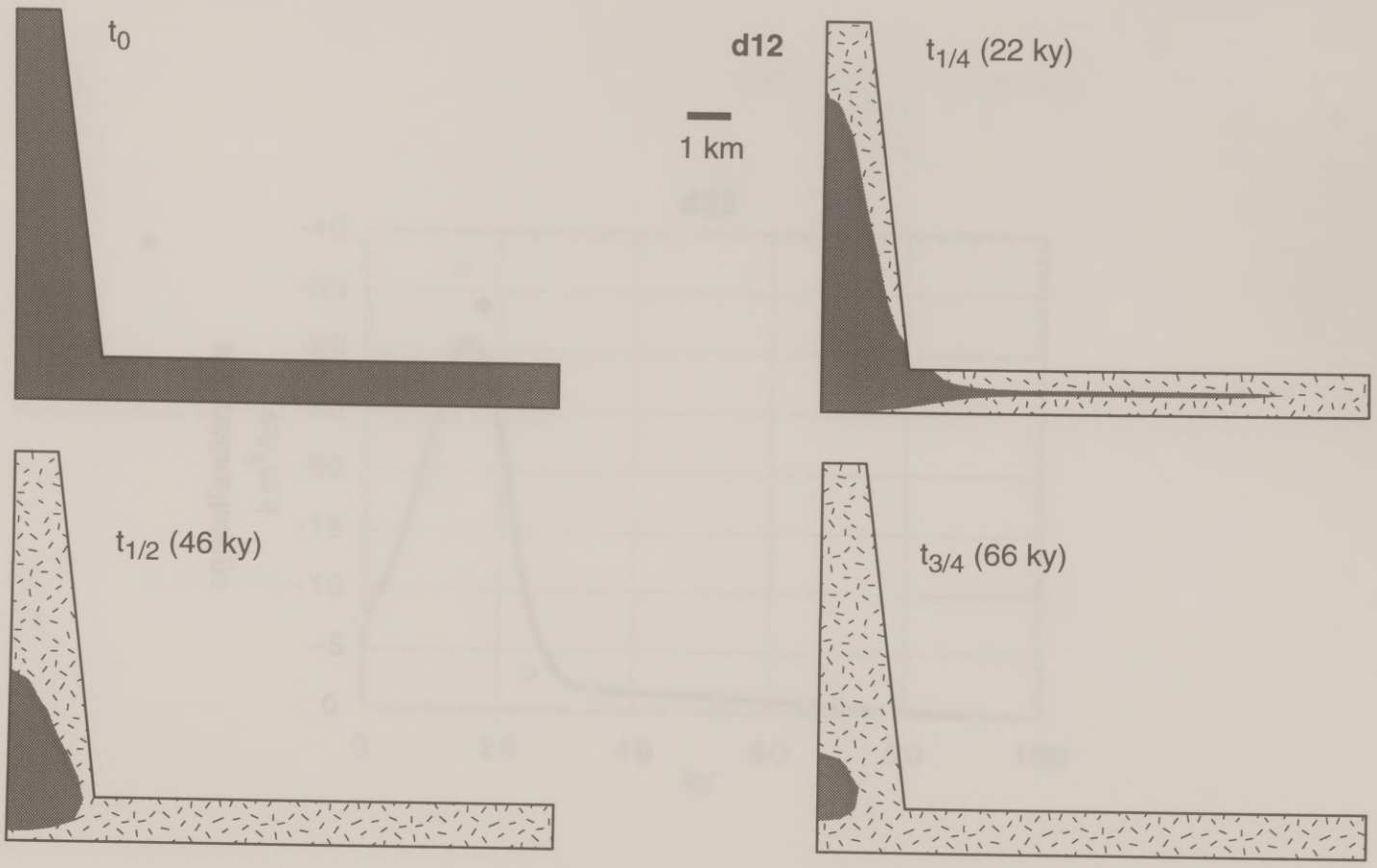
d12
1 km
$t_0$
$t_{1/4}$ (22 ky)
$t_{1/2}$ (46 ky)
$t_{3/4}$ (66 ky)

d22
crystallization rate
km3/ky
ky
-40
-35
-30
-25
-20
-15
-10
-5
0
0
20
40
60
80
100

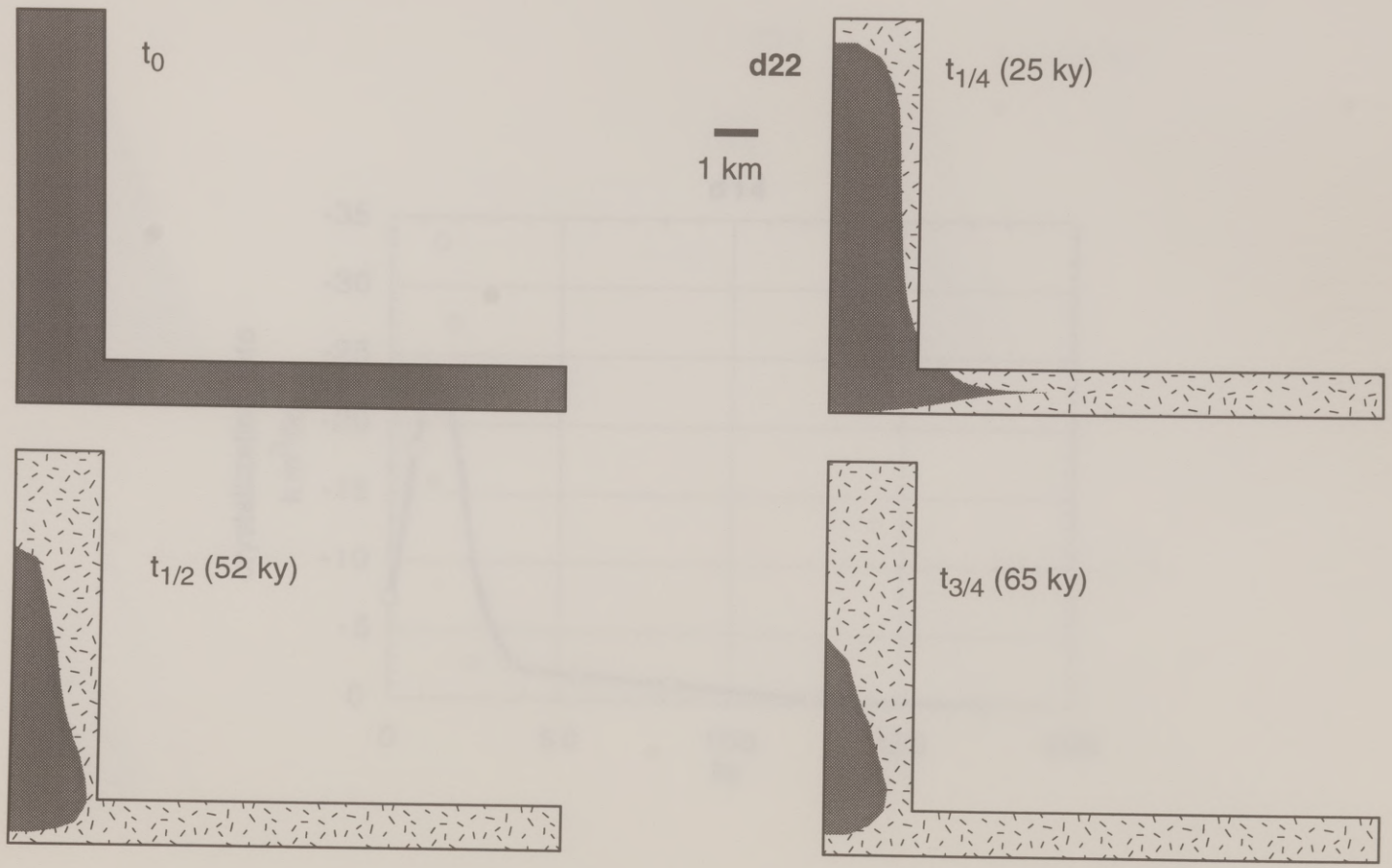
d22
1 km
$t_0$
$t_{1/4}$ (25 ky)
$t_{1/2}$ (52 ky)
$t_{3/4}$ (65 ky)

d14
crystallization rate
km3/ky
-35
-30
-25
-20
-15
-10
-5
0
0
50
100
150
200
ky

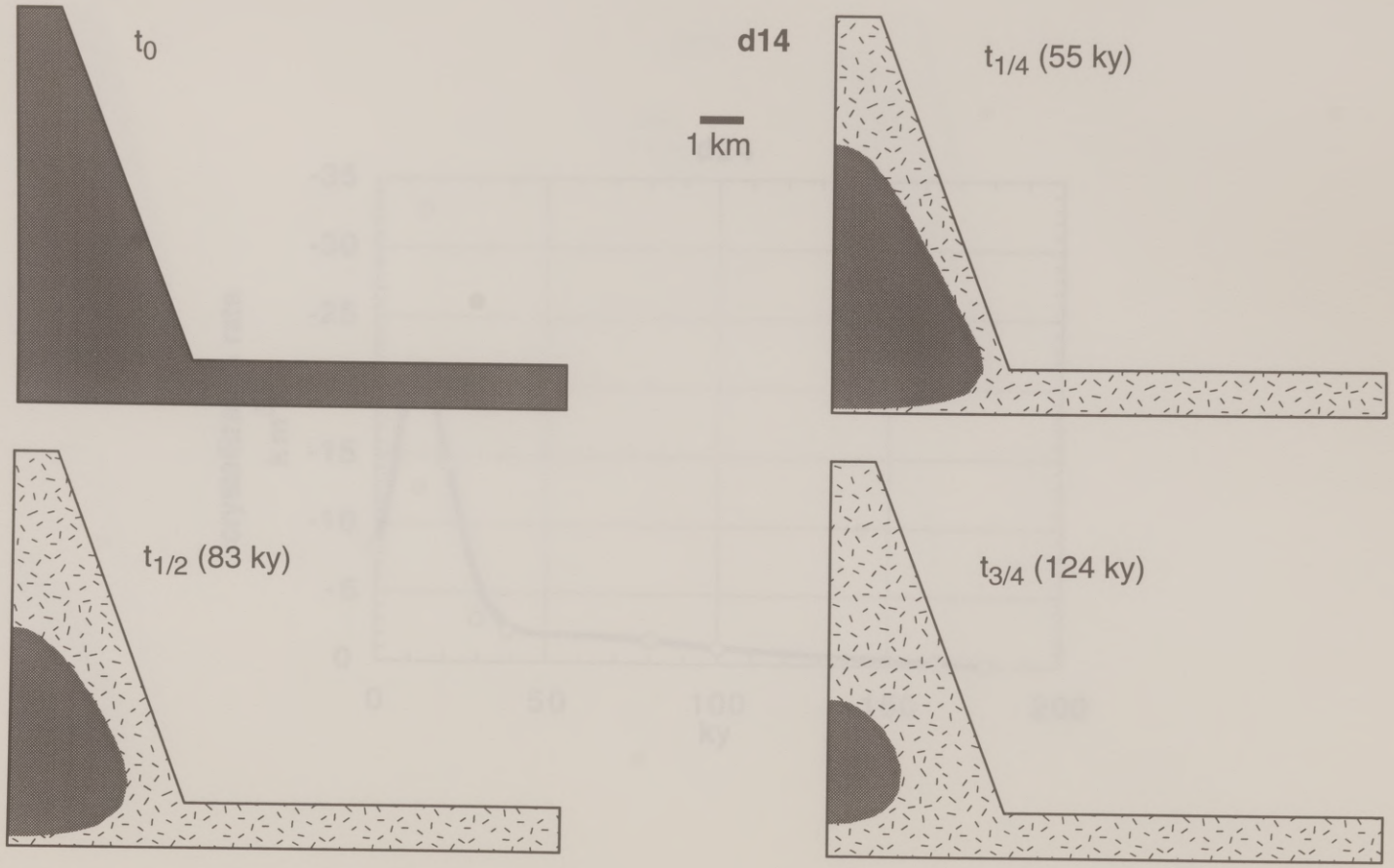
d14
1 km
$t_0$
$t_{1/4}$ (55 ky)
$t_{1/2}$ (83 ky)
$t_{3/4}$ (124 ky)

d24
crystallization rate
km³/ky
-35
-30
-25
-20
-15
-10
-5
0
0
50
100
150
200
ky

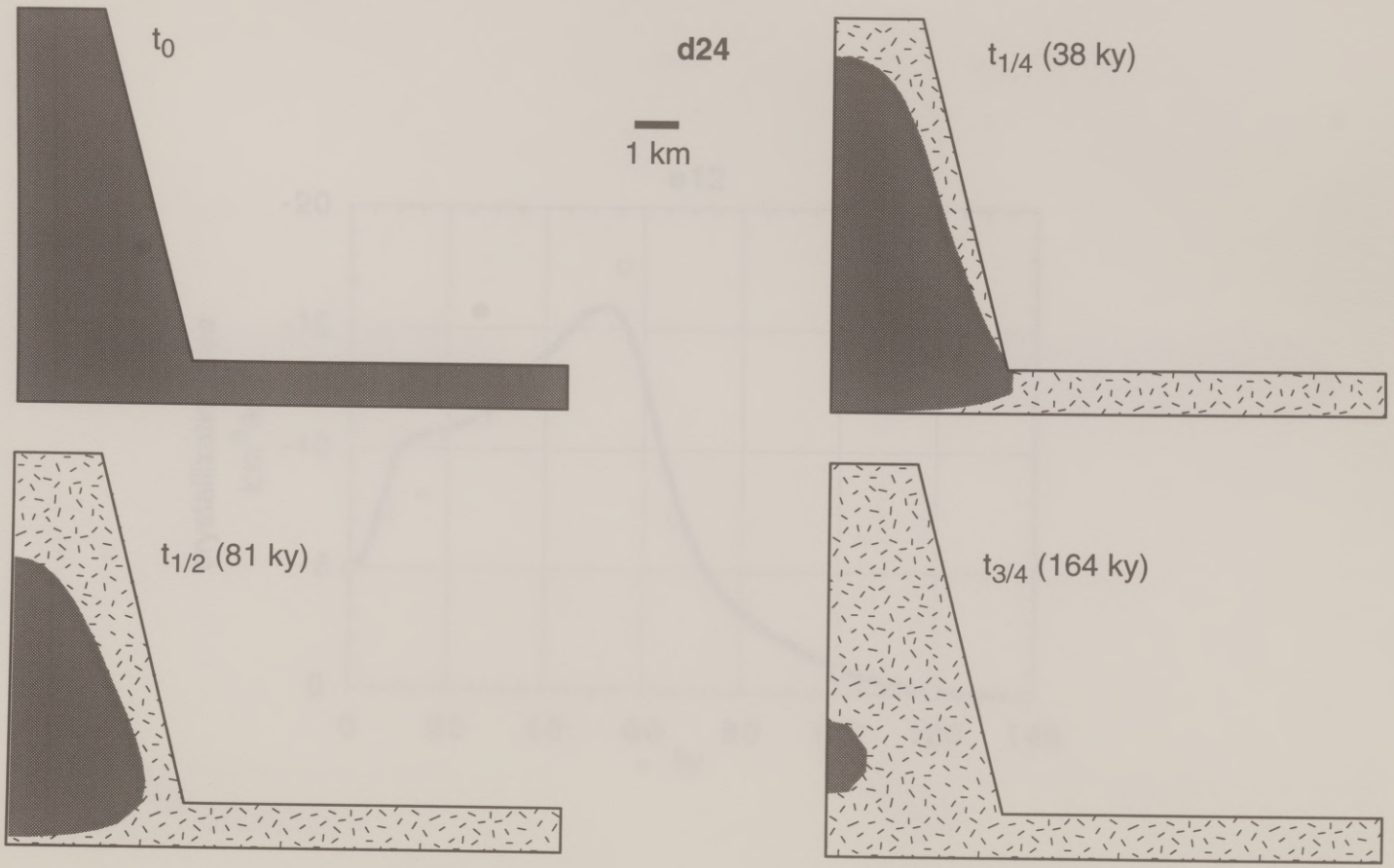
$t_0$
d24
1 km
$t_{1/4}$ (38 ky)
$t_{1/2}$ (81 ky)
$t_{3/4}$ (164 ky)

e12
crystallization rate
km3/ky
-20
-15
-10
-5
0
0
20
40
60
80
100
120
140
ky

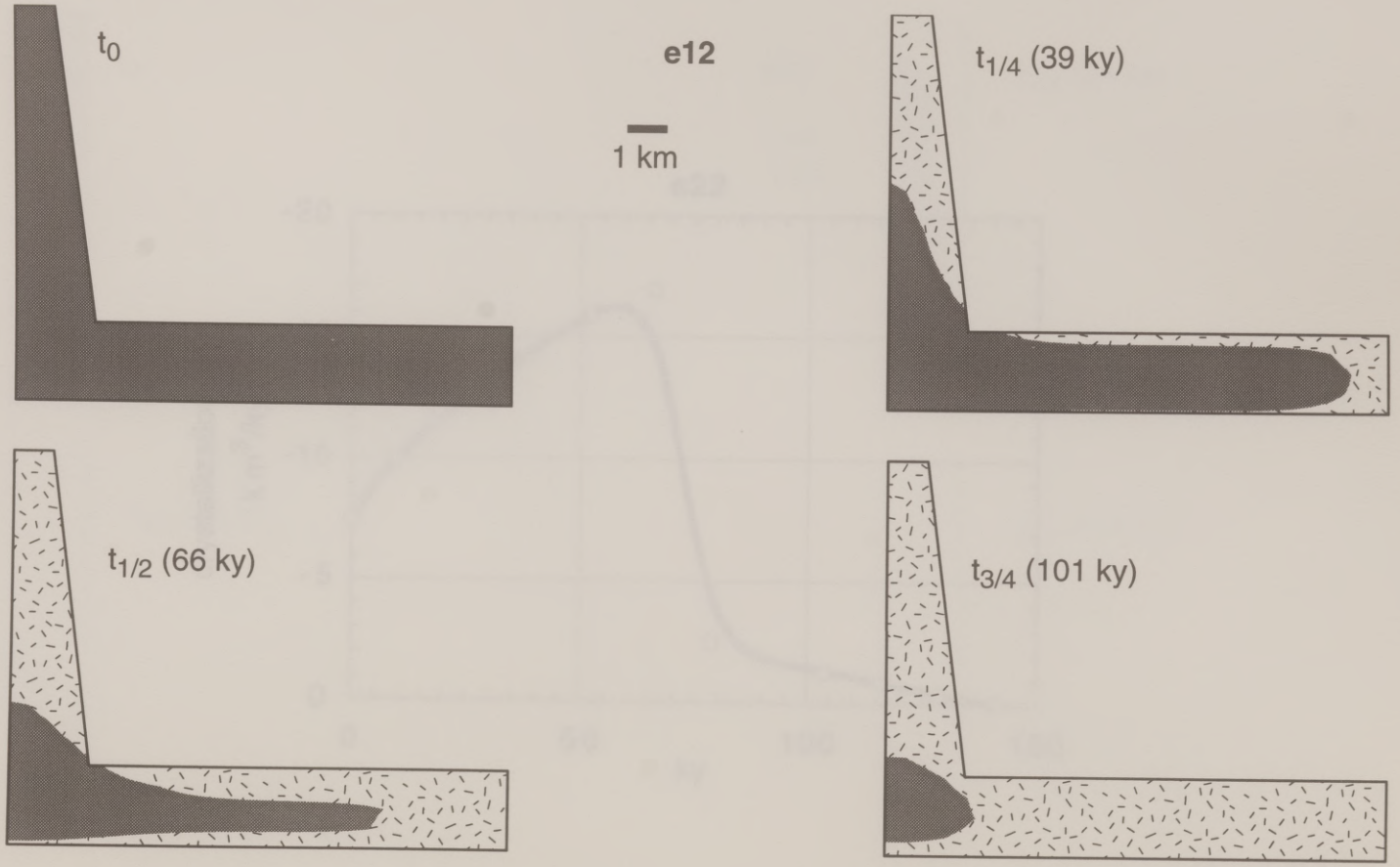
e12
1 km
$t_0$
$t_{1/4}$ (39 ky)
$t_{1/2}$ (66 ky)
$t_{3/4}$ (101 ky)

e22
crystallization rate
km3/ky
-20
-15
-10
-5
0
0
50
100
150
ky

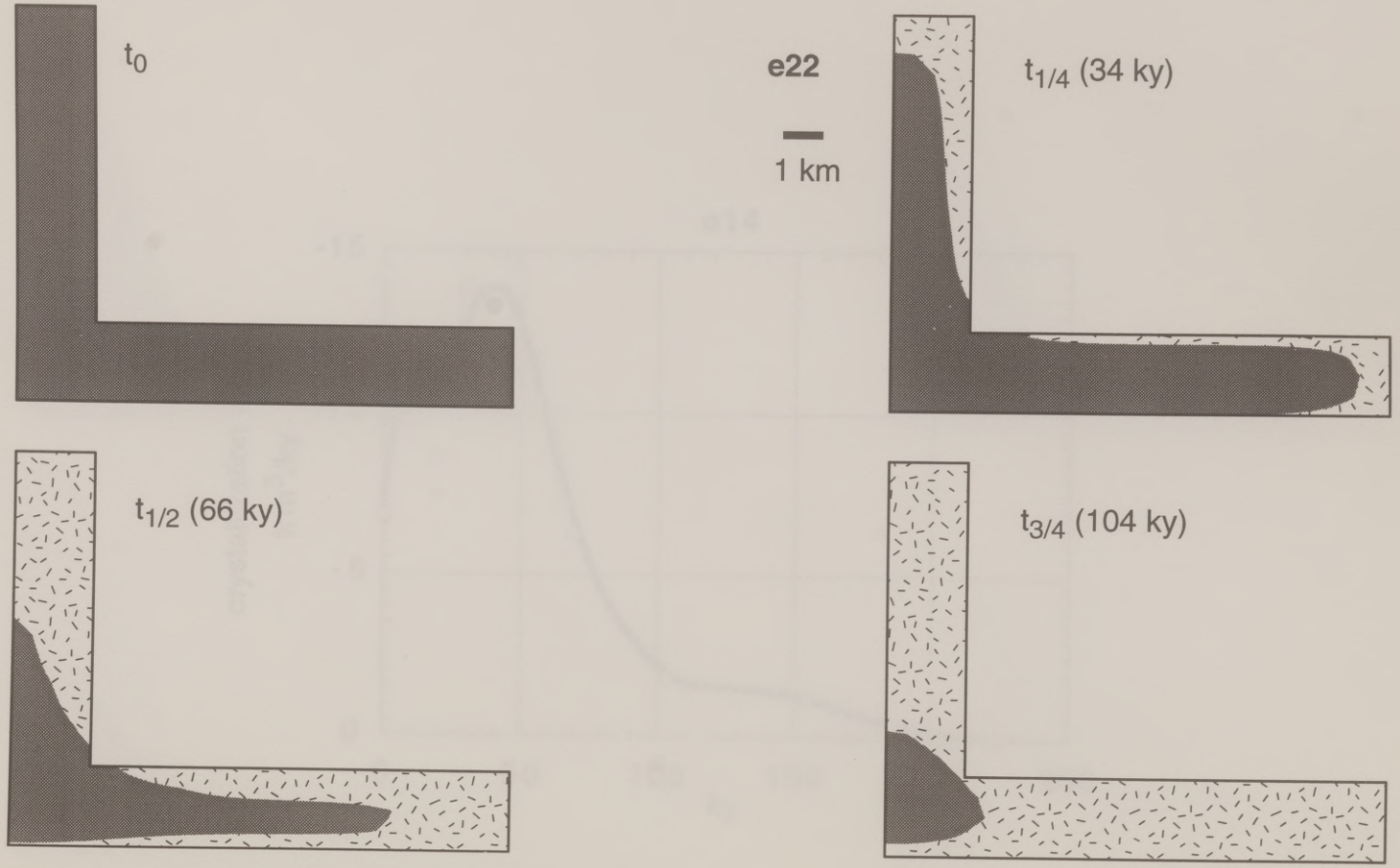
e22
1 km
$t_0$
$t_{1/4}$ (34 ky)
$t_{1/2}$ (66 ky)
$t_{3/4}$ (104 ky)

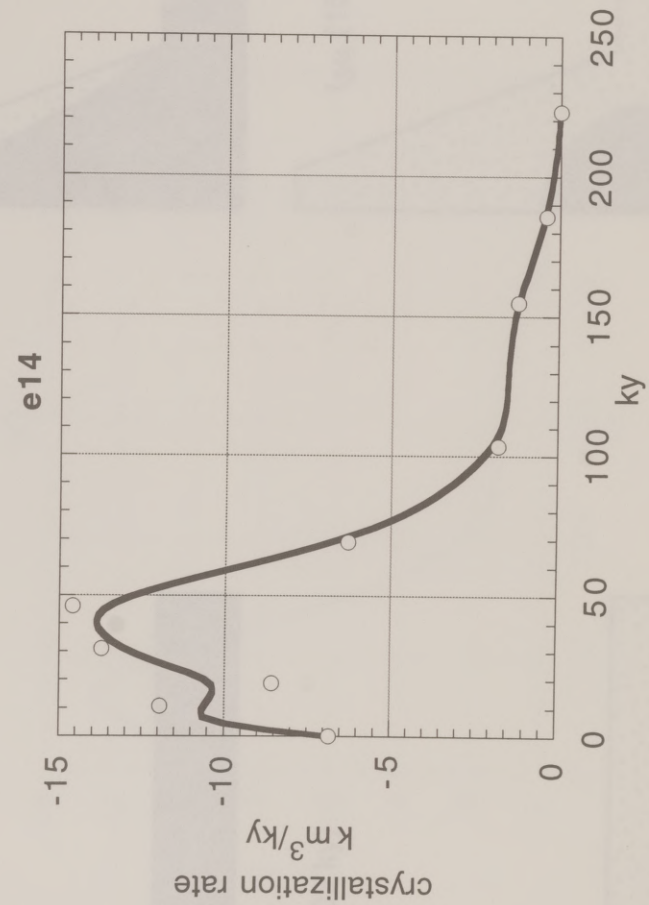
e14
crystallization rate
km3/ky
-15
-10
-5
0
0
50
100
150
200
250
ky

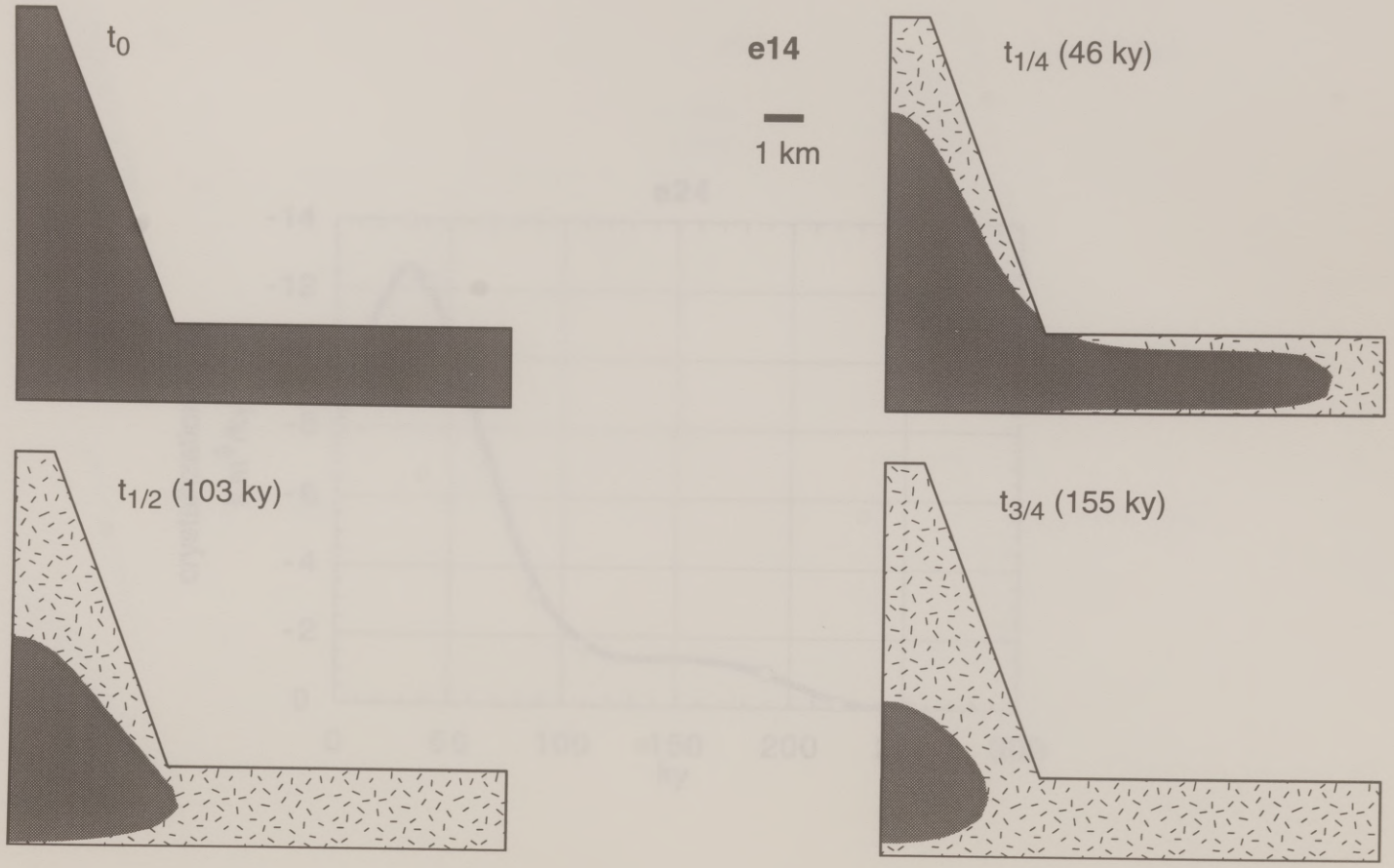
$t_0$
e14
1 km
$t_{1/4}$ (46 ky)
$t_{1/2}$ (103 ky)
$t_{3/4}$ (155 ky)

e24
crystallization rate
km³/ky
-14
-12
-10
-8
-6
-4
-2
0
0
50
100
150
200
250
300
ky

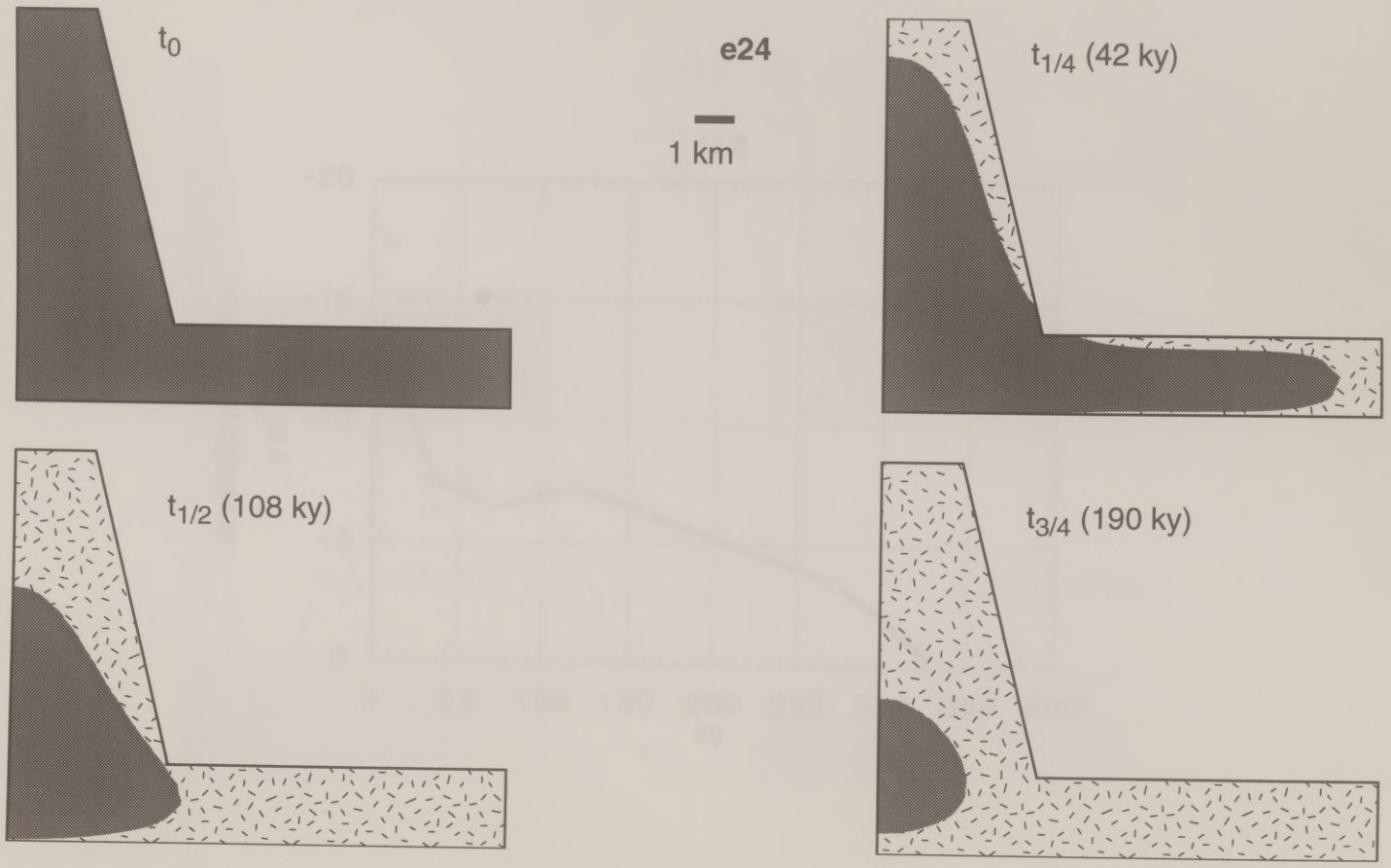
$t_0$
e24
1 km
$t_{1/4}$ (42 ky)
$t_{1/2}$ (108 ky)
$t_{3/4}$ (190 ky)

f12
crystallization rate
km3/ky
-20
-15
-10
-5
0
0
50
100
150
200
250
300
350
400
ky

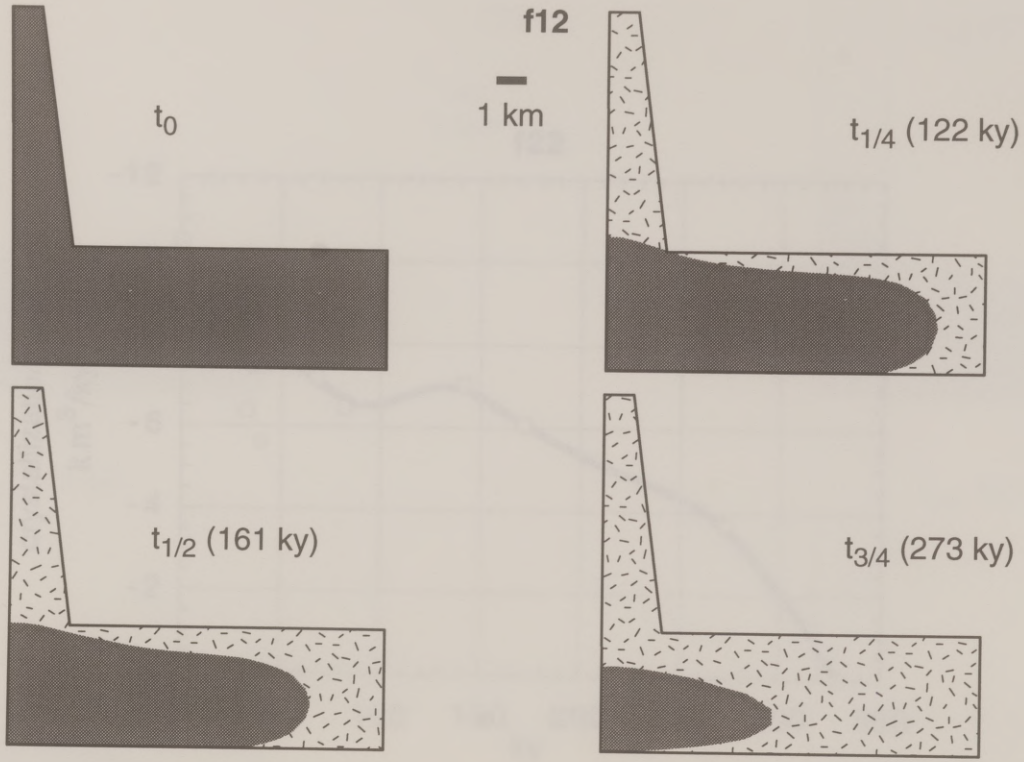
f12
1 km
$t_0$
$t_{1/4}$ (122 ky)
$t_{1/2}$ (161 ky)
$t_{3/4}$ (273 ky)

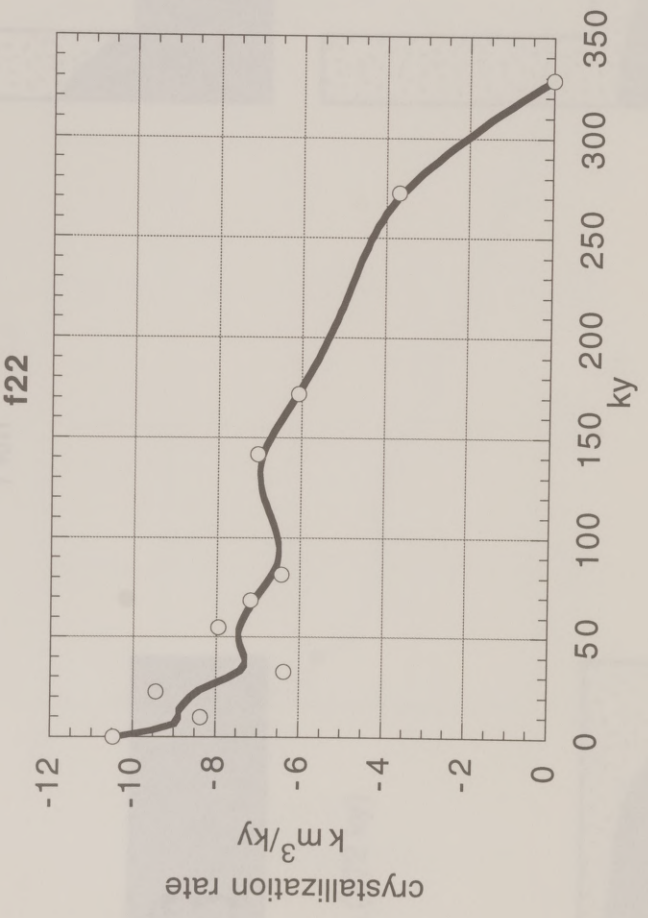
f22
crystallization rate
km3/ky
-12
-10
-8
-6
-4
-2
0
0
50
100
150
200
250
300
350
ky

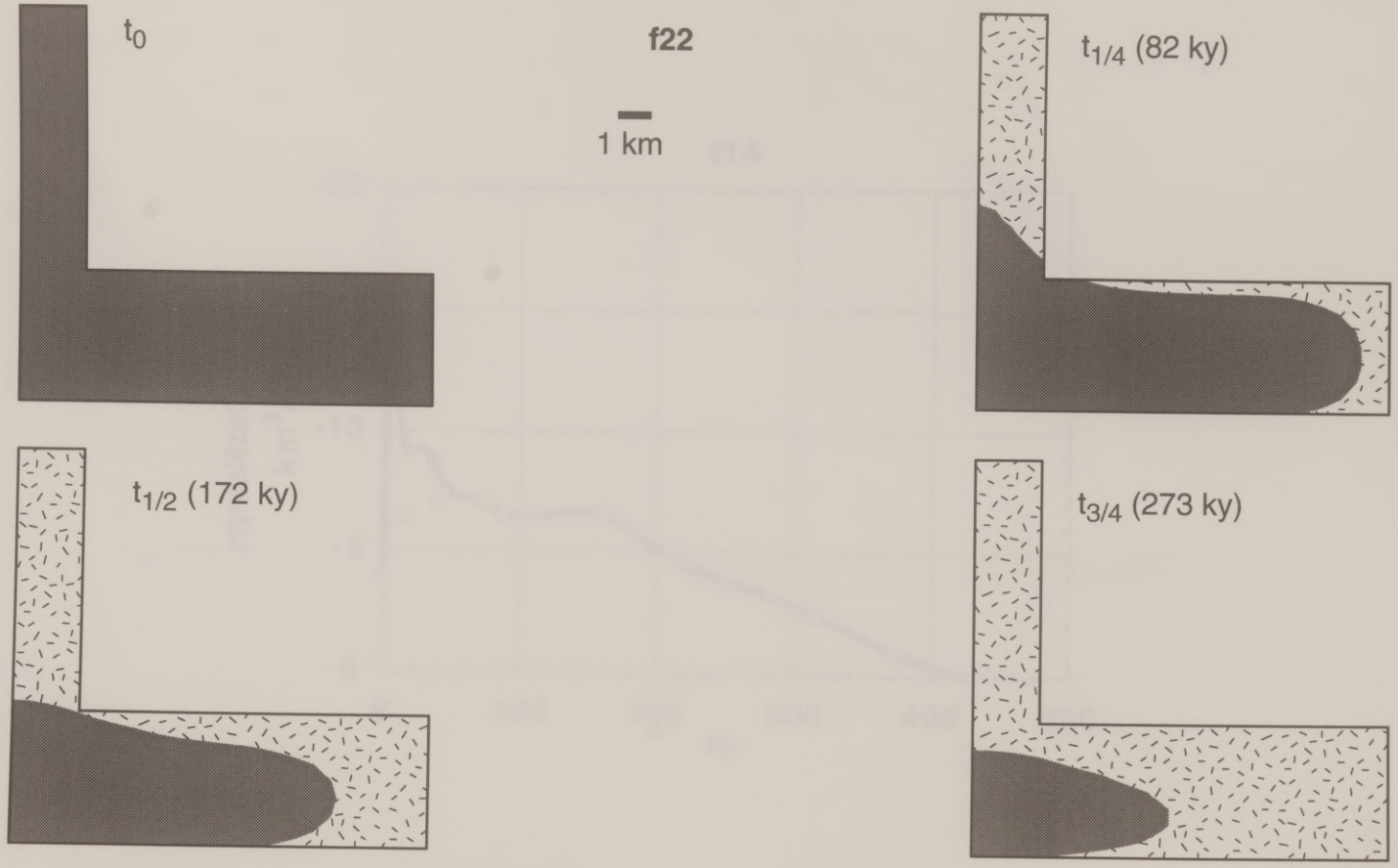


f22

1 km

f14
crystallization rate
km3/ky
-20
-15
-10
-5
0
0
100
200
300
400
500
ky

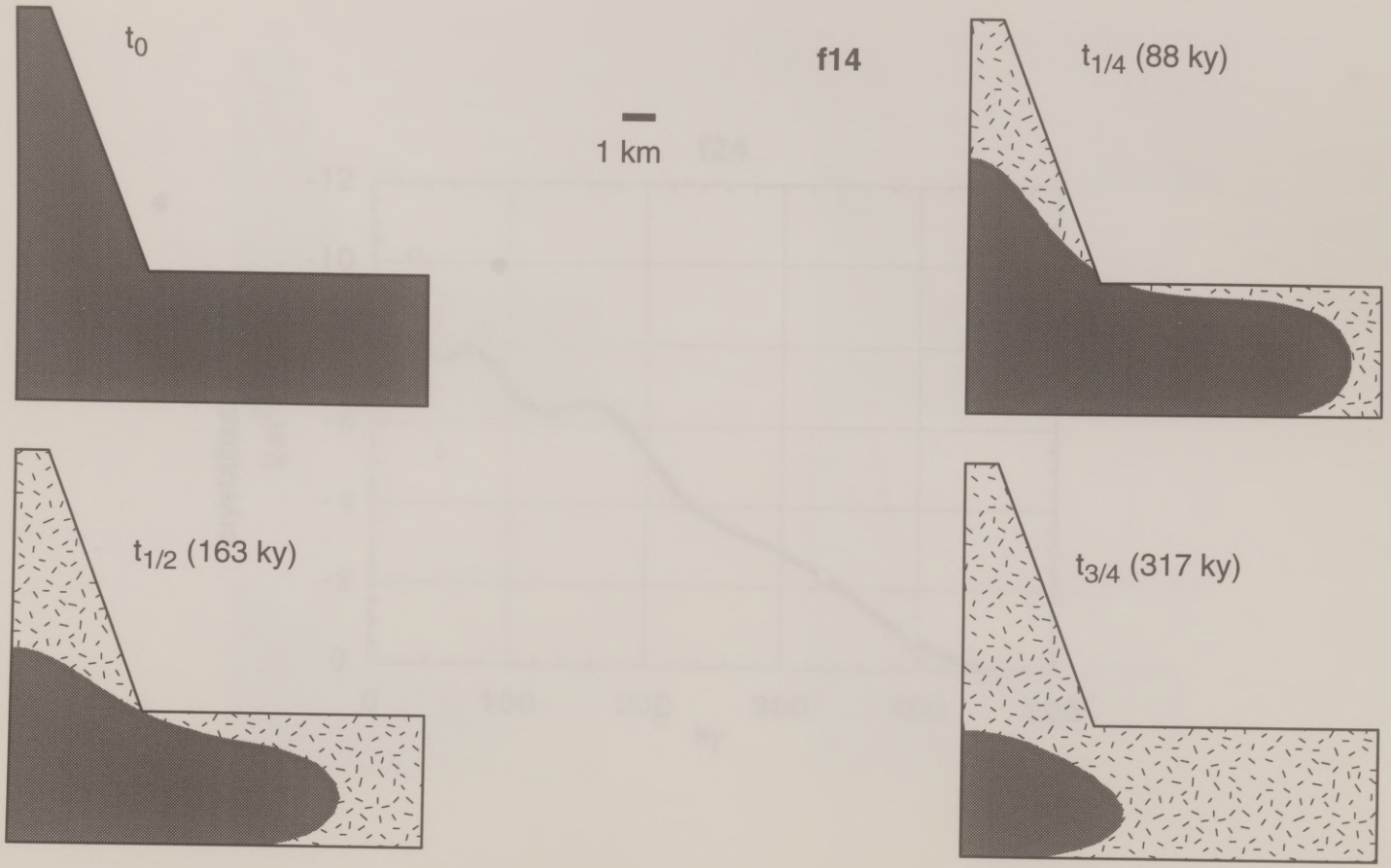


**f14**

f24
crystallization rate
km3/ky
-12
-10
-8
-6
-4
-2
0
0
100
200
300
400
500
ky

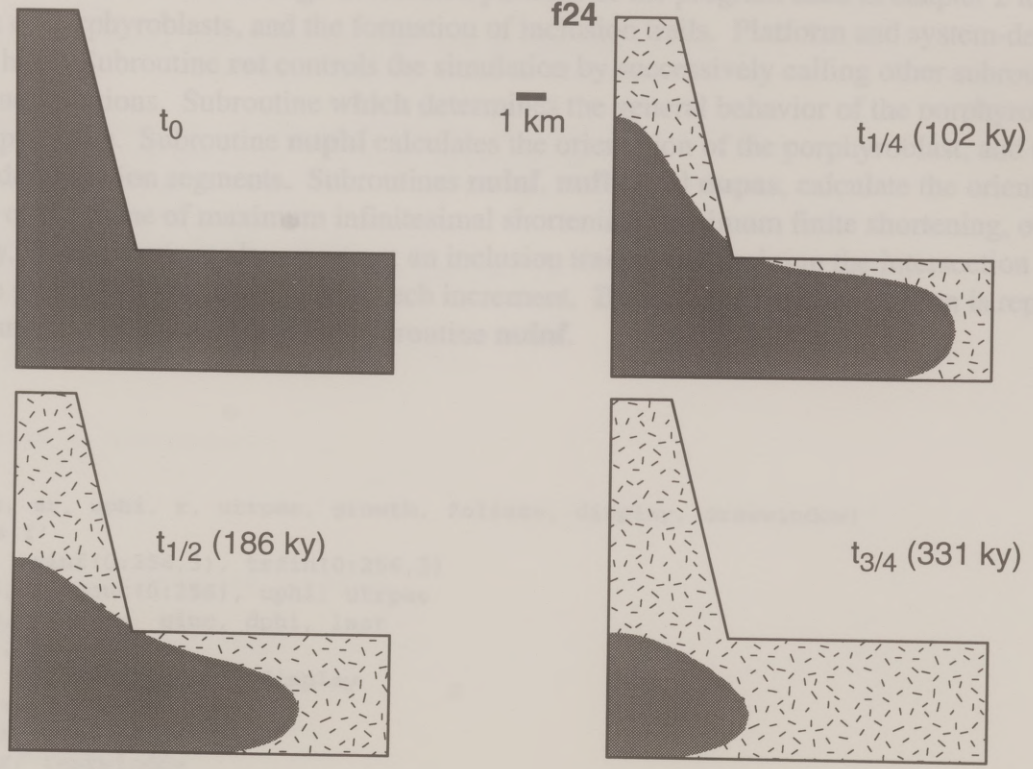
f24
1 km
$t_0$
$t_{1/4}$ (102 ky)
$t_{1/2}$ (186 ky)
$t_{3/4}$ (331 ky)

# Appendix B

This appendix contains FORTRAN listings of selected portions of the program used in chapter 2 to simulate the growth and rotation of porphyroblasts, and the formation of inclusion trails. Platform and system-dependent code is kept to a minimum here. Subroutine **rot** controls the simulation by successively calling other subroutines to rotate the porphyroblast and foliations. Subroutine **which** determines the general behavior of the porphyroblast, and the equations that are applicable. Subroutine **nuphi** calculates the orientation of the porphyroblast, and updates the orientation of included foliation segments. Subroutines **nuinf**, **nufin**, and **nupas**, calculate the orientation of a foliation consisting of the plane of maximum infinitesimal shortening, maximum finite shortening, or a passive marker, respectively. These routines also construct an inclusion trail by determining the intersection of the foliation with the shell of the porphyroblast grown during each increment. Because most of this portion is repeated from subroutine to subroutine, it is listed only in the subroutine **nuinf**.



```
      subroutine rot(g, sr, uphi, r, utrpas, growth, foliate, display, drawwindow)
      include 'Globals.f'
      real phi(0:256), trinf(0:256,3), trfin(0:256,3)
      real trpas(0:256,3), pout(0:256), uphi, utrpas
      real sr, g, a, b, c, p, r, ginc, dphi, last
      integer field, i, ni
      character*1 inp, foliate, growth, display
c The Window pointer
      record /WindowPtr/ drawwindow
      record /WindowPtr/ textwindow
c Storage for the Window Record
      record /WindowRecord/ myWrec
```

```
c Set up QDG to point to the QuickDraw A5 Globals
  QDG = JQDGLOBALS()


C Most of this is based on ghosh and ramberg (1976), and tends
C to follow their notation.
C phi(i) is the orientation of the long axis of the porphyroblast
C in the coordinate system of ghosh and ramberg (1976), for the
C i increment of strain
C For an equant porphyroblast it is the orientation of that line within
C the porphyroblast which was given as "initial orientation"
C sr is the ratio of rate of pure shear strain in the x
C direction to simple shear strain rate
C g is the total finite simple shear strain
C a, b, c are based on r, sr, and phi(i-1), as defined in
C ghosh and ramberg (1976) eqn. #4a
C r is axial ratio
C p is defined in ghosh and ramberg (1976) eqn. #11


c set number of steps in simulation
  ni = 64



C determine number of increments and interval
  ginc=g/real(ni)
c write(6,*) ni, "increments of", ginc


c determine what rotation equation to use
  call which(r, sr, field)


c set initial values to 0
  trinf(0,1) = 0.
```

```
  trinf(0,2) = 0.
  trinf(0,3) = 0.
  trfin(0,1) = 0.
  trfin(0,2) = 0.
  trpas(0,2) = 0.

c determine what is the foliation-forming element (plane of maximum infinitesimal shortening
c plane of maximum finite shortening, or passive marker), then calculate orientation of
c porphyroblast and foliation at successive increments, including segments of foliation
c in porphyroblast as it grows


  Select Case (foliate)
    Case ('i')

      Do i = 1,ni
        call nuphi(phi,i,field,r,sr,ginc,trinf,trfin,trpas)
        call nuinf(trinf,i,field,r,sr,ginc,ni,phi,growth)

      End Do
      call shoporph(drawwindow,myWrec,phi(ni),r)
      call shotr(drawwindow,myWrec,trinf,ni,display)


    Case ('f')

      Do i = 1,ni
        call nuphi(phi,i,field,r,sr,ginc,trinf,trfin,trpas)
        call nufin(trfin,i,field,r,sr,ginc,ni,phi,growth)

      End Do
      call shoporph(drawwindow,myWrec,phi(ni),r)
      call shotr(drawwindow,myWrec,trfin,ni,display)


    Case ('p')
```

```
      Do i = 1,ni
        call nuphi(phi,i,field,r,sr,ginc,trinf,trfin,trpas)
        call nupas(trpas,i,field,r,sr,ginc,ni,phi,growth,last)

      End Do
      call shoporph(drawwindow,myWrec,phi(ni),r)
      call shotr(drawwindow,myWrec,trpas,ni,display)


    Case Default

  End Select


c end do

  return
  stop
  end

c this subroutine determines, based on the axial ratio of the porphyroblast and the ratio of
c pure to simple shear, whether the porphyroblast will rotate continuously forward, or may
c back-rotate or reach a stable orientation

  subroutine which(r, sr, field)
  real r, sr, diff
  integer field

  if (r = 1.0) then
    field = 2
  else
    diff = sr-r/(r*r-1)
    if (diff.gt.(.0001)) then
      field = 1
```

```
      elseif (diff.lt.(-.0001)) then
        field = 2
      else
        field = 3
      endif

    end if

    return
    end


c this subroutine calculates the orientation of the porphyroblast at successive increments of strain.
c included foliation segments are rotated along with the porphyroblast

    subroutine nuphi(phi,i,field,r,sr,ginc,trinf,trfin,trpas)
    real phi(0:256), ginc, r, sr, a, b, c, d, p, trinf(0:256,3), trfin(0:256,3), trpas(0:256,3)
    integer i, field, j


    a = (r*r)/(r*r+1)
    b = sr*(r*r-1)/(r*r+1)
    c = 1/(r*r+1)

    if (field = 2) then

c equation 12, Ghosh and Ramberg (1976), p. 16 applies
c simplified in theorist
      d = sqrt(a*c - b*b)
      phi(i) = atan(d*tan(atan(b/d+c*tan(phi(i-1))/d)+d*ginc)/c-b/c)


    else if (field = 1) then

c equation 11, Ghosh and Ramberg (1976), p. 16 applies
      p = (c*tan(phi(i-1))+b-sqrt(b**2-a*c))/(c*tan(phi(i-1))+b+sqrt(b**2-a*c))*exp(2*ginc*sqrt(b**2-a*c))
```

```
      phi(i) = atan((sqrt(b**2-a*c)-b+(sqrt(b**2-a*c)+b)*p)/((-p+1)*c))

     else
c this seems unlikey, so we'll skip it for now
c     write(6,*) 'yikes'
     end if

C correct for tan change of sign, all phi(i) will be in
C quadrants I and II
     if (phi(i).lt.0.0) phi(i) = phi(i) + pi

     dphi = phi(i)-phi(i-1)
     if (dphi.lt.-.8029) dphi=dphi+pi

C update inclusion trails (that is, rotate the material that
C is within the porphyroblast by the same amount
C as the porphyroblast)


     do 10 j=1,i
       trinf(j,1) = trinf(j,1) + dphi
       trfin(j,1) = trfin(j,1) + dphi
       trpas(j,1) = trpas(j,1) + dphi


10   continue
     return
     end


c this subroutine calculates the orientation of the plane of maximum infinitesimal shortening
c at each increment, then constructs a segment of on included foliation by intersecting this plane with
c the shell of porphyroblast grown during that increment

     subroutine nuinf(trinf,i,field,r,sr,ginc,ni,phi,growth)
     real trinf(0:256,3), phi(0:256), r, sr, ginc, a, b, gamma, vi, vf, ai, af, ecc
```

```
  integer i, field, ni
  character*1 growth

C construct an inclusion trail

c determine orientation of infinitesimal strain cleavage
c include handling for sr=0, to avoid div by zero
c Ghosh 1993 eq. 8.89 or Ghosh 1982 eq. 10
  if (sr.eq.0.) then
    trinf(i,1) = pi/4.
  else
    trinf(i,1) = pi/2. - (atan(1./sr/2.)/2.)
  end if



  Select Case (growth)
    Case ('r')
      a = 1./real(ni)*real(i)
      b = a/r
      trinf(i,2) = a*b/(sqrt(abs(b*b*(cos(trinf(i,1)-phi(i)))**2.+a*a*(sin(trinf(i,1)-phi(i)))**2.)))
c try to make a ray
c avoid divide by zero
      if (i = 1) then
        trinf(i,3) = 0.0
      else
        a = 1./real(ni)*real(i-1)
        b = a/r
        trinf(i,3) = a*b/(sqrt(abs(b*b*(cos(trinf(i,1)-phi(i)))**2.+a*a*(sin(trinf(i,1)-phi(i)))**2.)))
      endif
    Case ('a')

      if (r = 1.0) then
        af = 4*pi*r**2
        ai = af/real(ni)*real(i)
        a  = sqrt(ai/4/pi)
```

```
        b  = a/r
        trinf(i,2) = a*b/(sqrt(abs(b*b*(cos(trinf(i,1)-phi(i)))**2.+a*a*(sin(trinf(i,1)-phi(i)))**2.)))
c try to make a ray
c avoid divide by zero
        if (i = 1) then
          trinf(i,3) = 0.0
        else
          ai = af/real(ni)*real(i-1)
          a  = sqrt(ai/4/pi)
          b  = a/r
          trinf(i,3) = a*b/(sqrt(abs(b*b*(cos(trinf(i,1)-phi(i)))**2.+a*a*(sin(trinf(i,1)-
phi(i)))**2.)))
        endif


      else
        ecc = sqrt(1-1/r**2)
        af = 2* pi* (1/r)**2 + 2* (pi*asin(ecc))/(ecc*r)
        ai = af/real(ni)*real(i)
        a = sqrt(ai/(2*pi/r**2+2*(pi*asin(ecc))/(ecc*r)))
        b = a/r
        trinf(i,2) = a*b/(sqrt(abs(b*b*(cos(trinf(i,1)-phi(i)))**2.+a*a*(sin(trinf(i,1)-phi(i)))**2.)))
c try to make a ray
c avoid divide by zero
        if (i = 1) then
          trinf(i,3) = 0.0
        else
          ai = af/real(ni)*real(i-1)
          a = sqrt(ai/(2*pi/r**2+2*(pi*asin(ecc))/(ecc*r)))
          b = a/r
          trinf(i,3) = a*b/(sqrt(abs(b*b*(cos(trinf(i,1)-phi(i)))**2.+a*a*(sin(trinf(i,1)-
phi(i)))**2.)))
        endif
```

```
      end if

    Case ('v')
      vf = 4./3.*pi*(1./r)**2.
      vi = vf/real(ni)*real(i)
      a = (3./4.*vi*r**2/pi)**.3333
      b = a/r
      trinf(i,2) = a*b/(sqrt(abs(b*b*(cos(trinf(i,1)-phi(i)))**2.+a*a*(sin(trinf(i,1)-phi(i)))**2.)))

c try to make a ray
c avoid divide by zero
        if (i = 1) then
          trinf(i,3) = 0.0
        else
          vi = vf/real(ni)*real(i-1)
          a = (3./4.*vi*r**2/pi)**.3333
          b = a/r
          trinf(i,3) = a*b/(sqrt(abs(b*b*(cos(trinf(i,1)-phi(i)))**2.+a*a*(sin(trinf(i,1)-
phi(i)))**2.)))
        endif

    Case Default

  End Select

  return
  end

c this subroutine calculates the orientation of the plane of maximum finite shortening
c at each increment, then constructs a segment of on included foliation by intersecting this plane with
c the shell of porphyroblast grown during that increment

c the portion where the inclusion trail is constructed is not included here, see subroutine nuinf
  subroutine nufin(trfin,i,field,r,sr,ginc,ni,phi,growth)
  real trfin(0:256,3), phi(0:256), r, sr, ginc, a, b, gamma, theta, vf, vi
  integer i, field, ni
  character*1 growth
```

```
C construct an inclusion trail
c determine orientation of cleavage to be included

  gamma = real(i)*ginc

c determine orientation of finite strain cleavage
c with special case for sr=0
c for sr=0 Ghosh 1993 eq. 8.69
c for sr .ne. 0 Ghosh 1982 eq. 8 or Ghosh 1993 eq. 9.3
  if (sr.eq.0.) then
    trfin(i,1) = pi/4+(atan(gamma/2.)/2.)
  else
    theta = 1./2.*atan((-exp(-2.*sr*gamma)+1.)/(((sinh(sr*gamma)/sr)**2.-exp(-
2.*sr*gamma)+exp(2.*sr*gamma))*sr))
    trfin(i,1) = pi/2-theta
  end if


C CONSTRUCT TRAIL HERE


  return
  end


c this subroutine calculates the orientation of the passive marker plane
c at each increment, then constructs a segment of on included foliation by intersecting this plane with
c the shell of porphyroblast grown during that increment
c the portion where the inclusion trail is constructed is not included here, see subroutine nuinf

  subroutine nupas(trpas,i,field,r,sr,ginc,ni,phi,growth,last)
  real trpas(0:256,3), phi(0:256), r, sr, ginc, a, b, gamma, theta, tmp, last
  integer i, field, ni
  character*1 growth

C construct an inclusion trail
c determine orientation of cleavage to be included
```

```
c got to avoid operating on included cleavage

  if (i.eq.1) last=trpas(0,1)


c determine orientation of passive marker cleavage
c with special case for sr=0
c if sr = 0 Ghosh 1993 eq. 8.73
c in sr .ne. 0 then Ghosh and Ramberg 1976 eq. 16
  if (sr.eq.0.) then

c   convert into an appropriate local coordinate system
c   without changing previous results
    tmp = pi/2-last

    trpas(i,1) = atan(1./((cos(tmp)/sin(tmp))+ginc))
c   convert back to g+r
    trpas(i,1) = pi/2 - trpas(i,1)
  else

    trpas(i,1) = atan(exp(2.*ginc*sr)*tan(last) + 1./(2.*sr)*(exp(2.*ginc*sr)-1.))

c     move into correct quadrant
      if (trpas(i,1).lt.0.) trpas(i,1)=trpas(i,1)+pi

  end if


c save new orientation

  last = trpas(i,1)


c CONSTRUCT TRAIL HERE


  return
  end
```

## References


Barton, M. D., and Hansen, R. B., 1989, Magmatism and the development of low pressure metamorphic belts: Implications from the western United States and thermal modeling: Geological Society of America Bulletin, v. 101, p. 1051-1065.

Bates, R. L., and Jackson, J. A., 1987, Glossary of geology: Alexandria, American Geological Institute, 788 p.

Beam, E. C., and Fisher, D. M., 1990, Rotation of elongate porphyroblasts in a shear zone, Kahiltna terrane, south central Alaska: Geological Society of America Abstracts with Program, v. 22, p. A183.

Busa, M. D., and Gray, N. H., 1992, Rotated staurolite porphyroblasts in the Littleton Schist at Bolton, Connecticut, USA: Journal of Metamorphic Geology, v. 10, p. 627-636.

Bell, T. H., 1985, Deformation partitioning and porphyroblast rotation in metamorphic rocks: a radical reinterpretation: Journal of Metamorphic Geology, v. 3, p. 109-118.

Bell, T. H., and Rubenach, M. J., 1980, Crenulation cleavage development-evidence for progressive bulk inhomogeneous shortening from "millipede" microstructures in the Robertson River Metamorphics: Tectonophysics, v. 68, p. T9-T15.

Bell, T. H., Forde, A., and Hayward, N., 1992a, Do smoothly curving, spiral-shaped inclusion trails signify porphyroblast rotation?: Geology, v. 20, p. 59-62.

Bell, T. H., Johnson, S. E., Davis, B., Forde, A., Hayward, N., and Wilkins, C., 1992b, Porphyroblast inclusion-trail orientation data: eppur non son girate!: Journal of Metamorphic Geology, v. 10, p. 295-307.

Best, M. G., 1982, Igneous and metamorphic petrology: New York, W. H. Freeman, 630 p.

Bjørnerud, M. G., and Zhang, H., 1994, Rotation of porphyroblasts in non-coaxial deformation: insights from computer simulations: Journal of Metamorphic Geology, v. 12, p. 135-139.

Bjørnerud, M., 1989, Mathematical model for folding of layering near rigid objects in shear deformation: Journal of Structural Geology, v. 11, p. 245-254.

Bowers, J. R., Kerrick, D. M., and Furlong, K. P., 1990, Conduction model for the thermal evolution of the Cupsuptic aureole, Maine: American Journal of Science, v. 290, p. 644-665.

Brandeis, G., and Marsh, B. D., 1989, The convective liquidus in a solidifying magma chamber: a fluid dynamic investigation: Nature, v. 339, p. 613-616.

Brun, J. P., and Cobbold, P. R., 1980, Strain heating and thermal softening in continental shear zones: A review: Journal of Structural Geology, v. 2, p. 149-158.

Brun, J. P., and Pons, J., 1981, Strain patterns of pluton emplacement in a crust undergoing non-coaxial deformation, Sierra Morena, Southern Spain: Journal of Structural Geology, v. 3, p. 219-229.

Burnham, C. W., 1979, Magmas and hydrothermal fluids, *in* Barnes, H. L., ed., Geochemistry of hydrothermal ore deposits: New York, John Wiley & Sons, p. 71-136.

Busa, M. D., and Gray, N. H., 1992, Rotated staurolite porphyroblasts in the Littleton Schist at Bolton, Connecticut, USA: Journal of Metamorphic Geology, v. 10, p. 627-636.

Candela, P. A., and Holland, H. D., 1984, The partitioning of copper and molybdenum between silicate melts and aqueous fluids: Geochimica et Cosmochimica Acta, v. 48, p. 373-380.

Candela, P., 1991, Physics of aqueous phase evolution in plutonic environments: American Mineralogist, v. 76, p. 1081-1091.

Carlson, W. D., 1989, The significance of intergranular diffusion to the mechanisms and kinetics of porphyroblast crystallization: Journal of Metamorphic Geology, v. 103, p. 1-24.

Carslaw, H. S., and Jaeger, J. C., 1959, Conduction of heat in solids: Oxford, Clarendon Press, 510 p.

Clark, M. B., and Fisher, D. M., 1995, Strain partitioning and crack-seal growth of chlorite-muscovite aggregates during progressive noncoaxial strain: an example from the slate belt of Taiwan: Journal of Structural Geology, v. 17, p. 461-474.

Cline, J. S., and Bodnar, R. J., 1991, Can economic porphyry copper mineralization be generated by a typical calc-alkaline melt?: Journal of Geophysical Research, v. 96, p. 8113-8126.

Cloos, M., Sapiie, B., and Penniston-Dorland, S., 1995, Formation of the Grasberg Cu-Au orebody, Irian Jaya, Indonesia: strike-slip faulting, cupolas, and bubbling magma chambers: Geological Society of America, Abstracts with Program, v. 27, p. A65.

Davidson, C., 1991, Tectonometamorphic evolution of the Maclaren glacier metamorphic belt, south-central Alaska [PhD thesis]: Princeton, 201 pp.

Davidson, C., and Hollister, L. S., 1992, Role of melt in the formation of a deep-crustal compressive shear zone: The Maclaren Glacier Metamorphic Belt, South Central Alaska: Tectonics, v. 11, p. 348-359.

Davidson, C., Schmid, S. M., and Hollister, L. S., 1994, Role of melt during deformation in the deep crust: Terra Nova, v. 6, p. 133-142.

De Bremaecker, J.-C., and Becker, E. B., 1978, Finite element models of folding: Tectonophysics, v. 50, p. 349-367.

Einstein, A., 1956, Investigations on the theory of the Brownian movement: New York, Dover, 119 p.

Fisher, D. M., 1990, Orientation history and rheology in slates, Kodiak and Afognak Islands, Alaska: Journal of Structural Geology, v. 12, p. 483-498.

Fleitout, L., and Froidevaux, C., 1980, Thermal and mechanical evolution ofshear zones: Journal of Structural Geology, v. 2, p. 159-164.

Fletcher, J. M., and Karlstrom, K. E., 1990, Late Cretaceous ductile deformation, metamorphism and plutonism in the Piute mountains, easterm Mojave desert: Journal of Geophysical Research, v. 95, p. 487-500.

Furlong, K. P., Hanson, R. B., and Bowers, J. R., 1991, Modeling thermal regimes, *in* Kerrick, D. M., ed., Contact Metamorphism: Reviews in mineralogy: Washington, Mineralogical Society of America, p. 437-505.

Gettings, M. E., 1988, Variation of the depth to the brittle-ductile transition due to cooling of a midcrustal intrusion: Geophysical Research Letters, v. 15, p. 213-216.

Ghosh, S. K., 1982, The problem of shearing along axial plane foliations: Journal of Structural Geology, v. 4, p. 63-67.

Ghosh, S. K., 1993, Structural Geology, Fundamentals and Modern Developments: Oxford, Pergamon, 598 p.

Ghosh, S. K., and Ramberg, H., 1976, Reorientation of inclusions by combination of pure shear and simple shear: Tectonophysics, v. 34, p. 1-70.

Giggenbach, W. F., 1992, Magma degassing and mineral deposition in hydrothermal systems along convergent plate boundaries: Economic Geology, v. 87, p. 1927-1944.

Gleason, G. C., and Tullis, J., 1993, Improving flow laws and piezometers for quartz and feldspar aggregates: Geophysical Research Letters, v. 20, p. 2111-2114.

Gray, N. H., and Busa, M. D., 1994, The three-dimensional geometry of simulated porphyroblast inclusion trails: inert marker, viscous-flow models: Journal of Metamorphic Geology, v. 12, p. 575-587.

Guglielmo, G., 1993, Interference between pluton expansion and non–coaxial tectonic deformation: Three–dimensional computer model and field implications: Journal of Structural Geology, v. 15, p. 593–608.

Hansen, R. B., and Barton, M. D., 1989, Thermal development of low-pressure metamorphic belts: Results from two-dimensional numerical models: Journal of Geophysical Research, v. 94, p. 10,363-10,377.

Hedenquist, J. W., and Lowenstern, J. B., 1994, The role of magmas in the formation of hydrothermal ore deposits: Nature, v. 370, p. 519-527.

Hillhouse, J. W., 1987, Accretion of southern Alaska: Tectonophysics, v. 139, p. 107-122.

Hillhouse, J., and Grommé, S., 1984, Northward displacement and accretion of Wrangellia: New paleomagnetic evidence from Alaska: Journal of Geophysical Research, v. 89, p. 4461-4477.

Hollister, L. S., 1993, The role of melt in the uplift and exhumation of orogenic belts: Chemical Geology, v. 108, p. 31-48.

Hollister, L. S., and Crawford, M. L., 1986, Melt-enhanced deformation: a major tectonic process: Geology, v. 14, p. 558-561.

Hutton, D. H. W., 1982, A tectonic model for the emplacement of the Main Donegal Granite, NW Ireland: Journal of the Geological Society of London, v. 139, p. 615–631.

Jaeger, J. C., 1961, The cooling of irregularly shaped igneous bodies: American Journal of Science, v. 259, p. 721-734.

Jaeger, J. C., 1964, Thermal effects of intrusions: Reviews of Geophysics, v. 2, p. 443-466.

Jones, D. L., Silberling, N. J., and Hillhouse, J., 1977, Wrangellia - A displaced terrane in northwestern North America: Canadian Journal of Earth Sciences, v. 14, p. 2565-2577.

Jones, D. L., Silberling, N., and Coney, P., 1986, Collision tectonics in the Cordillera of western N. America: examples from Alaska, *in* Coward, M., and Ries, A., eds., Collision Tectonics, Special Publication, Geological Society, p. 367-387.

Karlstrom, K. E., Miller, C. F., Kingsbury, J. A., and Wooden, J. L., 1993, Pluton emplacement along an active ductile thrust zone, Piute Mountains, southeastern California: Interaction between deformational and solidification processes: Geological Society of America Bulletin, v. 105, p. 213-230.

Karlstrom, K., 1989, Towards a syntectonic paradigm for granitoids: EOS, v. 70, p. 762, 770.

Kirby, S. H., and McCormick, J. W., 1989, Inelastic Properties of rocks and minerals: Strength and rheology, *in* Carmichael, R. S., ed., Physical properties of rocks and minerals: Boca Raton, CRC, p. 177-287.

Kohlstedt, D. L., Evans, B., and Mackwell, S. J., 1995, Strength of the lithosphere: Constraints imposed by laboratory experiments: Journal of Geophysical Research, v. 100, p. 17,587-17,602.

Lan, L., and Hudleston, P. J., 1991, Finite element models of buckle folds in non-linear materials: Tectonophysics, v. 9, p. 1-12.

Le Cloarec, M. F., Allard, P., Ardouin, B., Giggenbach, W. F., and Sheppard, D., S., 1992, Radioactive isotopes and trace elements in gaseous emissions from White Island, New Zealand: Earth and Planetary Science Letters, v. 108, p. 19-28.

Lister, G. S., Boland, J. N., and Zwart, H. J., 1986, Step-wise growth of biotite porphyroblasts in pelitic schists of the western Lys-Caillaouas massif (Pyrenees): Journal of Structural Geology, v. 8, p. 543-562.

Mares, V. M., and Kronenborg, A. K., 1993, Experimental deformation of muscovite: Journal of Structural Geology, v. 15, p. 1061-1075.

Marsh, B. D., 1988, On convective style and vigor in sheet-like magma chambers: Journal of Petrology, v. 30, p. 479-530.

Masuda, T., and Ando, S., 1988, Viscous flow around a rigid spherical body: a hydrodynamical approach: Tectonophysics, v. 148, p. 337-346.

Masuda, T., and Mochizuki, S., 1989, Development of snowball structure: numerical simulation of inclusion trails during synkinematic porphyroblast growth in metamorphic rocks: Tectonophysics, v. 170, p. 141-150.

McMahon, T. P., 1994, Pliocene intrusions in the Gunung Bijih (Ertsberg) mining district, Irian Jaya, Indonesia: Major- and trace-element chemistry: International Geology Review, v. 36, p. 925-946.

Nicolas, A., Bouchez, J. L., Blaise, J., and Poirier, J. P., 1977, Geological aspects of deformation in continental shear zones: Tectonophysics, v. 42, p. 55–73.

Nokleberg, W. J., Jones, D. L., and Silberling, N. J., 1985, Origin and tectonic evolution of the Maclaren and Wrangellia terranes, eastern Alaska Range, Alaska: Geological Society of America Bulletin, v. 96, p. 1251–1270.

Orange, D. L., 1990, Criteria helpful in recognizing shear-zone and diapiric melanges: examples from the Hoh accretionary complex, Olympic Peninsula, Washington: Geological Society of America Bulletin, v. 102, p. 935-951.

Oxburgh, E. R., and Turcotte, D. L., 1970, The thermal structure of island arcs: Geological Society of America Bulletin, v. 81, p. 1665-1688.

Parmentier, E. M., and Schedl, A., 1981, Thermal aureoles of igneous intrusions: Some possible indications of hydrothermal convective cooling: Journal of Geology, v. 89, p. 1-22.

Paterson, S. R., 1989, Are syntectonic granites truly syntectonic?: EOS, v. 70.

Paterson, S. R., Brudos, T., Fowler, K., Carlson, C., Bishop, K., and Vernon, R. H., 1991a, Papoose Flat pluton: forceful expansion or post-emplacement deformation?: Geology, v. 19, p. 324-327.

Paterson, S. R., Vernon, R. H., and Fowler, T. K., 1991b, Aureole tectonics, *in* Kerrick, D. K., ed., Contact Metamorphism: Washington, Mineralogical Society of America, p. 673-714.

Poirier, J. P., Bouchez, J. L., and Jonas, J. J., 1979, A dynamic model for aseismic ductile shear zones: Earth and Planetary Science Letters, v. 43, p. 441-453.

Rosenfeld, J. L., 1970, Rotated garnets in metamorphic rocks: Boulder, Geological Society of America Special Paper 129, 105 p.

Rubey, W. R., 1951, Geologic history of sea water: Geological Society of America Bulletin, v. 62, p. 1111-1148.

Shea, W. T., and Kronenberg, A. K., 1992, Rheology and deformation mechanisms of an isotropic mica schist: Journal of Geophysical Research, v. 97, p. 15,201-15,237.

Shinohara, H., and Kazahaya, K., 1995, Degassing processes related to magma-chamber crystallization, *in* Thompson, J. F. H., ed., Magmas, Fluids, and Ore Deposits: Short Course Series: Nepean, Mineralogical Association of Canada, p. 47-70.

Shinohara, H., Kazahaya, K., and Lowenstern, J. B., 1995, Volatile transport in a convecting magma column: implications for porphyry Mo mineralization: Geology, v. 23, p. 1091-1094.

Shreve, R. L., and Cloos, M., 1986, Dynamics of sediment subduction, melange formation, and prism accretion: Journal of Geophysical Research, v. 91, p. 10,229-10,245.

Silberling, N. J., Jones, D. L., Blake, M. C., and Howe, D. G., 1987, Lithotectonic terrane map of the western conterminous United States: U. S. Geological Survey Map 1874-C.

Silberling, N. J., Richter, D. H., and Jones, D. L., 1981, Recognition of the Wrangellia terrane in Clearwater Mountains and vicinity, southcentral Alaska: U. S. Geological Survey Circular, v. 823-B, p. 51-54.

Singh, M. M., 1981, Strength of rock, *in* Toulokian, Y. S., Jud, W. R., and Roy, R. F., ed., Physical properties of rocks and minerals: New York, McGraw Hill, p. 83-121.

Smith, R. L., 1979, Ash-flow magmatism, *in* Chapin, C. E., and Elston, W. E., eds., Ash-flow Tuffs: Boulder, Geological Society of America, p. 5-27.

Smith, T. E., 1981, Geology of the Clearwater Mountains, South-central Alaska, Geologic Reports: Anchorage, Alaska Division of Geological and Geophysical Surveys, 72 p.

Spry, A., 1963, The origin and significance of snowball structure in garnet: Journal of Petrology, v. 4, p. 211-222.

Stone, D., Panuska, B., and Packer, D., 1982, Paleolatitudes versus time for southern Alaska: Journal of Geophysical Research, v. 87, p. 3697-3707.

Stüwe, K., 1995, Thermal buffering effects at the solidus. Implications for the equilibration of partially melted metamorphic rocks: Tectonophysics, v. 248, p. 39-51.

Tobisch, O. T., and Paterson, S. R., 1990, The Yarra Granite: an intradeformational pluton associated with ductile thrusting, Lachlan Fold Belt, southeastern Australia: Geological Society of America Bulletin, v. 102, p. 693-703.

Tullis, J. A., 1979, High temperature deformation of rocks and minerals: Reviews of Geophysics and Space Physics, v. 17, p. 1137-1154.

Turcotte, D. L., and Schubert, G., 1973, Frictional heating of the descending lithosphere: Journal of Geophysical Research, v. 78, p. 5876-5886.

Turcotte, D. L., and Schubert, G., 1982, Geodynamics: New York, John Wiley and Sons, 450 p.

Vernon, R. H., and Flood, R. H., 1988, Contrasting deformation styles of S– and I–type granitoids in the Lachlan Fold Belt, eastern Australia: Tectonophysics, v. 147, p. 127–143.

Wallace, W. K., Hanks, C. L., Rogers, J. F., 1989, The southern Kahiltna terrane: Implications for the tectonic evolution of southwestern Alaska: Geological Society of America Bulletin, v. 101, p. 1389–1407.

Wilks, K. R., and Carter, N. L., 1990, Rheology of some continental lower crustal rocks: Tectonophysics, v. 182, p. 57-77.

Williams, P. F., and Schoneveld, C., 1981, Garnet rotation and the development of axial plane crenulation cleavage: Tectonophysics, v. 78, p. 307-334.

Zienkiewicz, O. C., and Taylor, R. L., 1989, The finite element method, v. 1: Basic formulations and linear problems: New York, McGraw Hill, 648 p.

Zienkiewicz, O. C., and Taylor, R. L., 1991, The finite element method, v. 2: Solid and fluid mechanics, dynamics, and non–linearity: New York, McGraw Hill.

The vita has been removed from the digitized version of this document.